Drexel University

Annual Progress Report: 2008 Formula Grant

Reporting Period

July 1, 2009 – June 30, 2010

Formula Grant Overview

The Drexel University received $ 1,215,241 in formula funds for the grant award period January 1, 2009 through December 31, 2010. Accomplishments for the reporting period are described below.

Research Project 1: Project Title and Purpose

Triggers of Inflammation in Scleroderma - Scleroderma is a disease caused by uncontrolled accumulation of collagen in the soft tissues. Its cause is unknown and the progression of the disease is not well understood. Recent research has identified a new inflammatory pathway that does not reflect traditional T cell activation. This pathway senses danger signals from the tissues that are external to the cells. The goal of this project is to understand the role of this new inflammatory pathway and other inflammatory signaling pathways in early scleroderma skin lesions and to investigate the signaling in several mouse models that have had pertinent proteins in this new pathway deleted.

Duration of Project

1/1/2009 - 12/31/2009

Project Overview

The inflammasome is a newly identified inflammatory signaling pathway that detects danger signals external from the cell. This signaling is independent of toll-like receptor signaling. We will be focusing on a well-defined model for the autoimmune fibrotic disease, systemic sclerosis. The goal of this project is to tease apart the involvement of the inflammasome by studying several knockout mouse models and utilizing bleomycin (BLM) to induce fibrosis in the dermis.

Specific Aim. To understand the contribution of *inflammatory signaling molecules* in early dermal fibrotic lesions and autoantibody production utilizing various knockout mouse models**.**

This project will determine the precise role of the inflammatory signaling molecules in BLM-induced fibrosis. All knockout mice are on a C57BL/6J background and will include p110δ-/-, TLR7-/-, INFαβR-/-, MyD88$^{-/-}$, TRIF$^{-/-}$, ASC$^{-/-}$, or NALP3$^{-/-}$ deficient mice. These mice will be compared to C57BL/6J wild-type mice.

These models will allow us to understand the contributions of a broad range of inflammatory triggers and their role in fibrosis. We will inject wild-type C57BL/6J mice and p110δ-/-, TLR7-/-, INFαβR-/-, MyD88-/-, TRIF-/-, ASC-/-, or NALP3-/- mice with bleomycin for 28 days. Mice will be sacrificed on day 29 and the injection site analyzed for fibrosis by histological stains, H&E and trichrome where we will compare the size and thickness of the fibrotic lesion in these mice to determine the contribution of the inflammatory signaling molecule to fibrosis. We will assay the injection site by Western blotting for proteins, such as COL1A1, COL3A1, and TGF-beta. As autoantibodies are the hallmark of autoimmune diseases, we will investigate the presence of autoantibodies in response to bleomycin in the knockout models. It is known that bleomycin induces autoantibody production and therefore we will perform assays to detect and characterize using Hep2 cells. Data from this study will allow us to focus our efforts on pertinent signaling molecules that contribute to fibrosis. As the cause of fibrosis in SSc is unknown, we may identify new and effective therapies for the treatment of fibrosis and autoimmune diseases.

Principal Investigator

Carol M. Artlett, PhD
Associate Professor
Drexel University College of Medicine
Microbiology & Immunology
2900 Queen Lane, Room G75
Philadelphia PA 19129

Other Participating Researchers

Peter D. Katsikis, MD, PhD – employed by Drexel University College of Medicine

Expected Research Outcomes and Benefits

Scleroderma is an aggressive disease and even with treatment the death rate after 10 years is approximately 50%. Like all autoimmune diseases, the cause of scleroderma is unknown and the progression of the disease is not well understood. It exhibits all the classic hallmarks of an autoimmune disease, whereby disease specific autoantibodies are identified in 98% of scleroderma affected individuals.

Recent research has identified new inflammatory pathways that do not reflect traditional immune activation. One of these pathways, the inflammasome, senses danger signals in the tissues that are external to the cells and signals through a pathway called the inflammasome. The inflammasome activates important and specific cytokines and in scleroderma these specific cytokines are activated implicating the involvement of the inflammasome. The other pathway investigates Toll-like receptor (TLR) signaling and pertinent down stream molecules. The goal of this project is to understand the role of these new inflammatory pathways in early scleroderma skin lesions by allowing us to investigate the signaling mediated by triggers of inflammation in mouse models that have had pertinent proteins in this new pathway deleted.

Investigating the contribution of TLR and the inflammasome to the early skin fibrosis in scleroderma will allow us to 1) potentially identify the initiating mechanisms of fibrosis in scleroderma; 2) understand how signaling further down stream from the inflammasome and TLR is affected; 3) determine if autoantibody expression is orchestrated by the inflammasome or TLR signaling; and 4) may provide hope for a new therapeutic strategy to treat scleroderma where there are currently no effective therapies for controlling disease progression. Indeed, this research may shed light on the initiating mechanisms of autoimmunity as a whole.

Summary of Research Completed

Fibroblasts stimulated with bleomycin express more collagen COL1A1 and COL3A1.
First, we wanted to confirm by *in vitro* studies in our laboratory that bleomycin induced the expression of collagen molecules so that we could further study the expression of the inflammasome in mouse dermal cells. Fibroblasts were isolated from C57BL/6 skin, cultured until confluent and incubated with 10 nM bleomycin for 24 h. The RNA was isolated and assayed it by real-time PCR for COL1A1 and COL3A1 transcripts and the expression of these transcripts was normalized to β-actin. We found that collagen COL1A1 mRNA levels increased by 13% and COL3A1 increased by 66% (Figure 1) with the bleomycin treatment. These differences were found to be statistically significant ($P = 0.0018$ for COL1A1 and $P = 0.0004$ for COL3A1).

Bleomycin induced TGF-β1 mRNA in mouse fibroblasts. We then further investigated the expression of fibrotic mediators in the bleomycin treated fibroblasts and found that TGF-β1 mRNA levels were also increased in a dose dependent manner (Figure 2). In these experiments we were trying to determine the best amount of bleomycin to use in these studies.

Bleomycin induces inflammatory cytokines in vitro in human fibroblasts. It is now known that fibroblasts contribute to the innate immune signaling and these cells are no longer thought to be just involved in extracellular matrix expression and it has been suggested that bleomycin induced fibrosis must be mediated by the innate immune system. Recently it has been shown that the inflammasome is part of the innate immune signaling system as its activation takes place early in response to infection. Therefore, we cultured normal human fibroblasts to determine pertinent cytokine expression in response to bleomycin (Figure 3). We found that bleomycin induced mRNA increases for IL-1β, IL-18, IL-33, and IL-6. The increase in mRNA for IL-1β, IL-18, and IL-33 do not directly show inflammasome activation but may suggest increases in substrates of the inflammasome activation and also positive feedback loops originating from the inflammasome. For example, mature IL-1β is a known potent inducer of IL-1β mRNA in fibroblasts. Thus in our experiments of Figure 3, mRNA increases may suggest inflammasome activation and the induction of mature cytokines that induce mRNA upregulation in fibroblasts.

NALP3 is involved in bleomycin induced skin fibrosis in mice. Treated mice had both flanks shaved to allow for the relocation of the injection sites. Bleomycin was injected into the dermis of one flank and PBS (carrier) was injected into the other flank in C57BL/6 (n=6), NALP3-/- (n=6), ASC-/- (n=4), and MyD88-/- (n=2) mice for 28 days. The mice were sacrificed by CO_2 asphyxiation and cervical dislocation. Skin from the injection sites and lung was harvested and embedded in paraffin for sectioning. Sections were stained with Masson's trichrome to detect collagen (blue stain). The sections of skin and lung were photographed at 10X magnification

(Figure 4). Measurements of skin thickness were taken at five random points across the image from the epidermis down to the pannus carnosus layer and the measurements in each mouse was averaged. In the C57BL/6 mice, we found that bleomycin induced a 1.75 +/- 0.29 fold increase (~75% increase) in the thickness of the dermal layer compared to NALP3-/- mice that showed no increase (1.04 +/- 0.24 fold increase in skin thickness) and MyD88-/- mice (1.03 +/- 0.25) (Figure 4).

However, we found that ASC was not absolutely necessary for dermal fibrosis, suggesting that there may be an alternative adaptor molecule in the skin. This is the first observation of this. Further, this alternative adaptor molecule may not be as efficient at activating CASP1, as induction of fibrosis was approximately half of that which was observed in the wild-type mice (Figure 4). We also harvested the lung from the C57BL/6, NALP3-/-, ASC-/-, and MyD88-/- mice and stained the sections with Masson's trichrome. It is known that bleomycin injected in the skin will also induce fibrosis in the lung and indeed we observed that the lung in the C57BL/6 mouse had altered architecture and increased collagen deposition whereas, the NALP3, ASC, and MyD88 deficient mice did not. Of note, the lung was completely devoid of fibrosis in the ASC-/- confirming the previously published data. In summary, these results show that NALP3 and MyD88 play a critical role in bleomycin induced skin fibrosis and provides strong support for our hypothesis that the inflammasome may be involved in skin fibrosis.

Infiltrating cells in skin biopsies at the BLM or PBS injection sites. We investigated infiltrating cells in the C57BL6/J wild type mice and the NALP3-/-, ASC-/- mice to determine if any changes in inflammatory cell numbers were present. We found that in the wild type mice BLM induced a CD3 inflammatory infiltrate at 28 days with BLM. This was also confirmed with the NALP3-/- and ASC-/- mice. We observed no difference in the number of infiltrating cells in the 3 groups for CD3. We also investigated the presence of macrophages and observed that there were no differences in the pattern of infiltrate between the PBS injection site and the BLM injection site.

Bleomycin activation of the inflammasome is inhibited with KCl. It has previously been demonstrated that the activation of the NALP3 inflammasome can be specifically inhibited by potassium chloride (KCl). KCL does not inhibit other inflammasomes. Therefore, we wanted to determine if inflammasome activation by bleomycin could be prevented when KCl was added to fibroblasts at the same time as 10 nM bleomycin. This experiment confirms that bleomycin does indeed activate the NALP3 inflammasome. Normal fibroblasts were incubated with 10 nM bleomycin and 100 nM KCl for 24 h. RNA was extracted and transcripts for IL-18, IL-33, and NALP3 were measured by real-time PCR. We found that with KCl, mRNA transcripts were reduced to below control levels (Figure 5). We also found that KCL decreased NALP3 transcripts but these were still elevated. These data confirm that bleomycin activates the NALP3 inflammasome.

IL-33, IL-18, and NALP3 mRNA is elevated in SSc fibroblast cell lines. We investigated mRNA expression of IL-18, IL-33, and NALP3 to determine if the expression of these proteins are elevated in SSc. Low passage (passage 4) SSc primary cell lines (n=7) were cultured in DMEM supplemented with 10% FBS and antibiotics. RNA was purified and converted to cDNA and IL-18, IL-33 and NALP3 mRNA transcripts were measured by Real Time PCR and normalized to

β-actin expression (Figure 6). Expression of the transcripts was compared to expression in normal fibroblasts (n=4).

NALP3, Active CASP1, and IL-1β Proteins are elevated in scleroderma (SSc) dermal fibroblasts. The bleomycin mouse model which we utilized to understand the role of the inflammasome in fibrosis is a good model for scleroderma. Therefore we investigated the activation of the inflammasome in primary fibroblast cell lines. A critical step in the activation of CASP1 is the assembly of the inflammasome. CASP-1 is present in the cytosol as an inactive zymogen but becomes activated through the inflammasome, via self cleavage to produce a p20 subunit. CASP1 cleavage is dependent on the NALP3 inflammasome. The resulting activation of CASP1 then induces cleavage of IL-1β. We investigated the expression of the inflammasome protein NALP3 and active CASP1, the CASP1 p20 fragment in SSc fibroblast cell lines (n=4) established from the active lesions and compared these to normal cell lines (n=4). NALP3 was expressed 1.86 fold more (increase of 86%), active CASP1 cleaved protein fraction was found to be 5.4-fold more (increase of 540%) and cleaved IL-1β was expressed 1.52 (increase of 52%) than that expressed in normal fibroblasts (Figure 7). These data suggest that the inflammasome is activated and participating in disease in SSc and further validates our rationale for further studying this mechanism in SSc.

Immunofluorescence of active CASP1 and NALP3 protein identify altered localization in SSc fibroblasts. We stained fibroblasts of low passage for active CASP1 (p20) protein and NALP3. Compared to control fibroblasts, active CASP1 was detected more in the SSc fibroblasts and appeared to aggregate in the cytoplasm (Figure 8). NALP3 protein in the controls was found close to the nucleus, whereas in SSc the protein appeared to localize to the cytoplasm and stress fibers. This data further supports the activation of the inflammasome in SSc.

Active CASP1 p20 subunit is elevated in SSc lung tissue. We investigated the expression of the active CASP1 p20 subunit in paraffin embedded lung tissue from SSc (n=1) and normal (n=1). Briefly the sections were deparaffinized, boiled in 10 mM Citrate buffer, pH 6.0 for 30 min and blocked with 5% goat serum. Primary antibody rabbit-anti-CASP1 p20 was diluted 1:50 and applied to the section for 40 min at room temperature in a humid chamber. The unbound antibody was washed off and the secondary antibody goat-anti-rabbit-Cy2 was diluted and applied to the section for 40 min. Slides were washed and mounted with DaPI and a coverslip and viewed with a Nikon Eclipse epi-fluorescent microscope (Figure 9).

Bleomycin induces the secretion of IL-6 from normal human fibroblasts and IL-6 is elevated in SSc fibroblasts. We measured IL-6 protein in the culture media from human fibroblasts treated with bleomycin by ELISA. We found that 10nM bleomycin stimulated the fibroblasts to secrete 1.8 fold more IL-6 into the media (Figure 10). This was statistically significant $P = 0.05$. We further found that IL-6 protein is elevated in SSc fibroblasts.

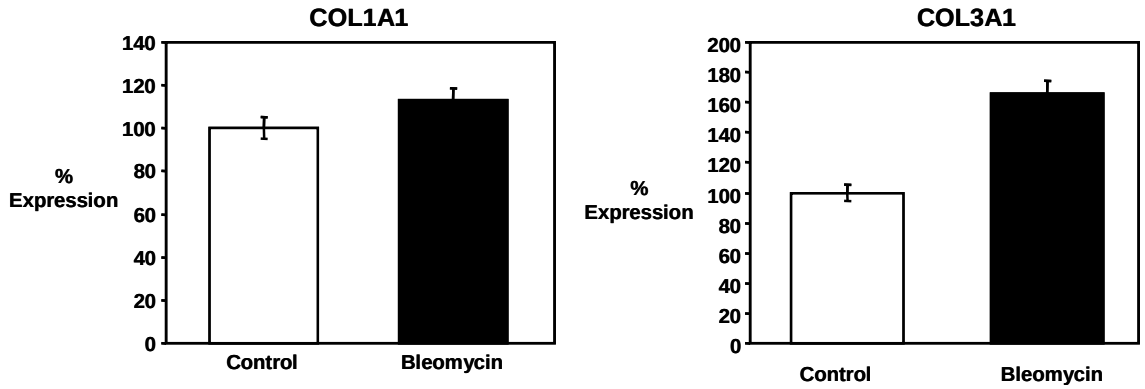

Figure 1. Bleomycin induced collagen expression in human fibroblasts. Fibroblasts were stimulated overnight with 10nM bleomycin. RNA was extracted and made into cDNA and COL1A1 and COL3A1 transcripts were measure by real-time PCR. All transcripts were normalized to β-actin expression. Pooled data from n=5 mouse fibroblast lines. COL1A1, P = 0.0018; COL3A1 P = 0.0004

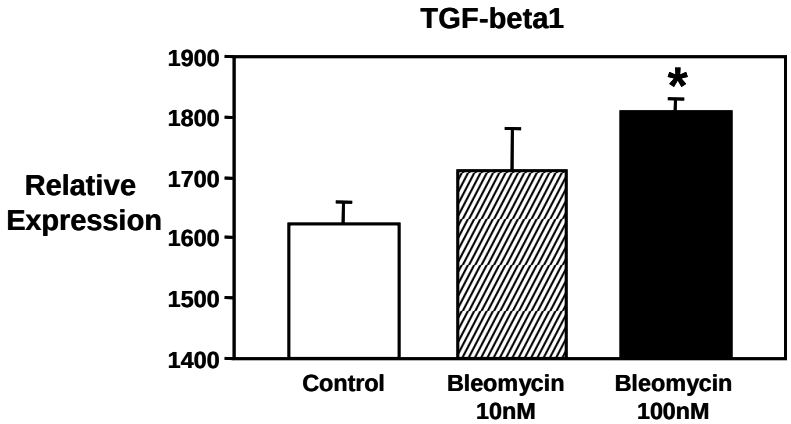

Figure 2. TGF-β1 expression is induced with bleomycin. Fibroblasts were stimulated overnight with 10 nM or 100nM bleomycin. RNA was extracted and made into cDNA and TGF-β1 transcripts were measure by real-time PCR and corrected for β-actin expression. Pooled data from n=5 human fibroblast from healthy donors shown. *P = 0.024.

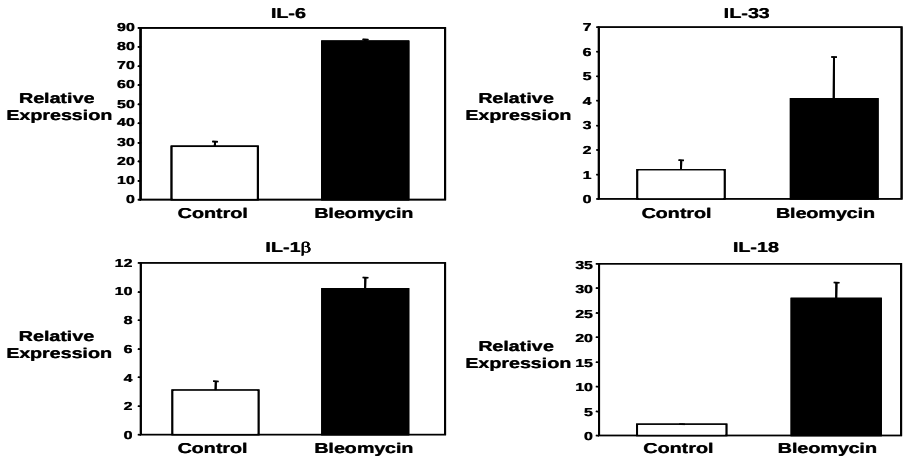

Figure 3. Bleomycin induces IL-1β, IL-6, IL-18 and IL-33 mRNA. Fibroblasts isolated from normal skin were treated overnight with 100nM bleomycin. RNA was extracted and converted to cDNA and IL-1β, IL-6, and IL-33 transcripts were measured by Real Time PCR. mRNA transcripts were normalized to β-actin. We found that with bleomycin, there was almost a 3.2-fold increase in IL-1β, (P = 0.0085); a 3-fold increase in IL-6 (P = 0.0012); a 3.5-fold increase in IL-33 (P = 0.009); and a 12.6 fold increase in IL-18 (P= 0.0082). Pooled data from human fibroblast from n=5 healthy donors shown.

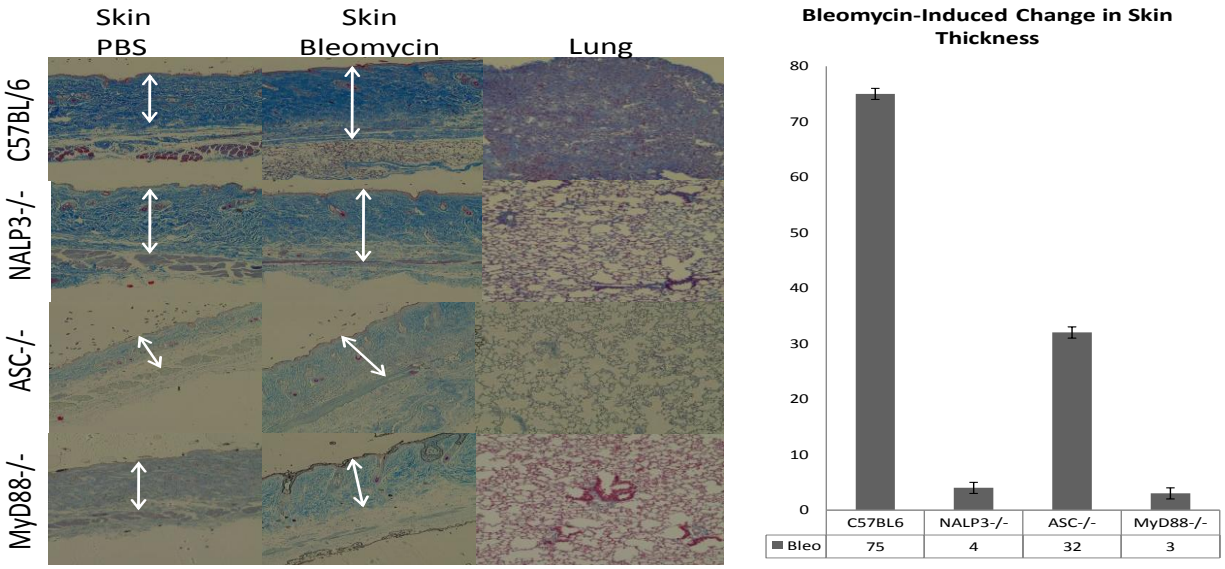

Figure 4. Bleomycin induced skin thickening is abrogated in NALP3-/- and MyD88-/-mice. C57BL6 (n=12), NALP3-/- (n=12, ASC-/- (n=12), and MyD88-/- (n=12) mice were injected intradermally for 28 days. Skin and lung were collected, embedded in paraffin and sectioned for staining. Note the increased skin thickness in the bleomycin treated C57BL/6 mice compared to the NALP3-/-, ASC-/-, and MyD88-/- mice. Also note the lung occlusion and collagen (blue) deposition in the C57BL/6 mice. The NALP3-/-, ASC-/-, and MyD88-/- had normal lung architecture and there was no increase in collagen, denoted by blue staining. The skin thickness was measure at 5 random places across the image and then averaged (e.g. white arrow). We found that the increase in skin thickness in the C57BL6 mice was 1.75 (+/- 0.29) fold more, whereas no increase was found in the NALP3-/- (1.04 +/- 0.24 fold increase) or MyD88-/- (1.03 +/- 0.25). These differences were statistically significant with P = 0.019 for NALP3-/- and P=0.05 for MyD88-/-. Fold increases were determined by comparing the bleomycin treated flank with PBS treated flank in each mouse. Left: Representative animals are shown. All images are at 10X magnification; Right: Pooled data from C57BL6 (n=12), NALP3-/- (n=12), ASC-/- (n=12), MyD88 (n=12) shown.

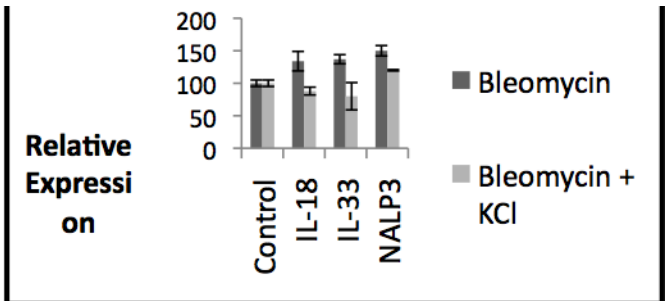

Figure 5. Bleomycin activation of the inflammasome is abolished with KCl. Fibroblasts isolated from normal skin were treated overnight with 10nM bleomycin or 10nM bleomycin + KCl. RNA was extracted and converted to cDNA and IL-18, IL-33, and NALP3 transcripts were measured by Real Time PCR. mRNA transcripts were normalized to β-actin. We found that with the addition of KCl, bleomycin stimulation of inflammasome proteins was abolished further confirming that bleomycin activates the inflammasome.

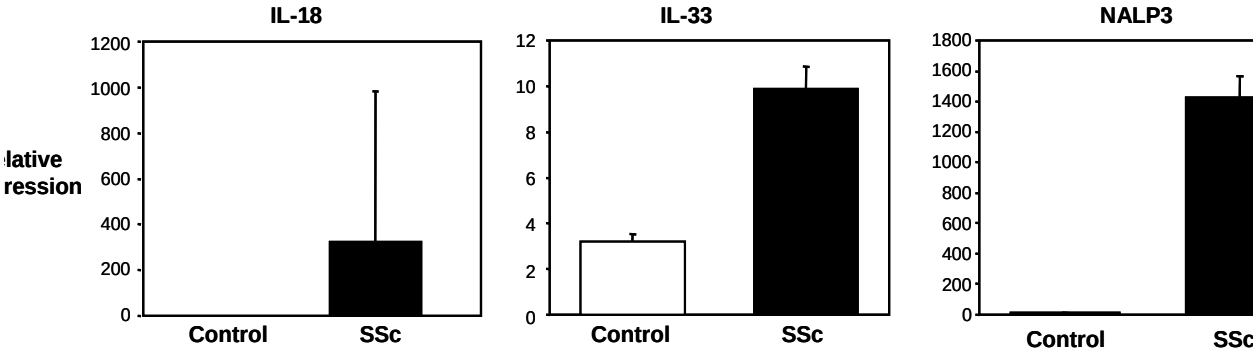

Figure 6. mRNA levels of IL-18, IL-33, and NALP3 are increased in SSc fibroblasts. Primary cell lines from SSc patients (n=7) of low passage (4) were cultured and RNA was extracted, converted to cDNA. IL-18, IL-33, and NALP3 transcripts were measured by real-time PCR. All transcripts were normalized to β-actin and compared to control fibroblasts (n=4). We found that the average expression was IL-18: 323 in SSc vs. 0.41 in control (P<0.0001); IL-33: 9.85 in SSc vs. 3.21 in control (P<0.001); and NALP3: 1423 in SSc vs. 9.5 in control (P<0.0001). Bar graphs show pooled data.

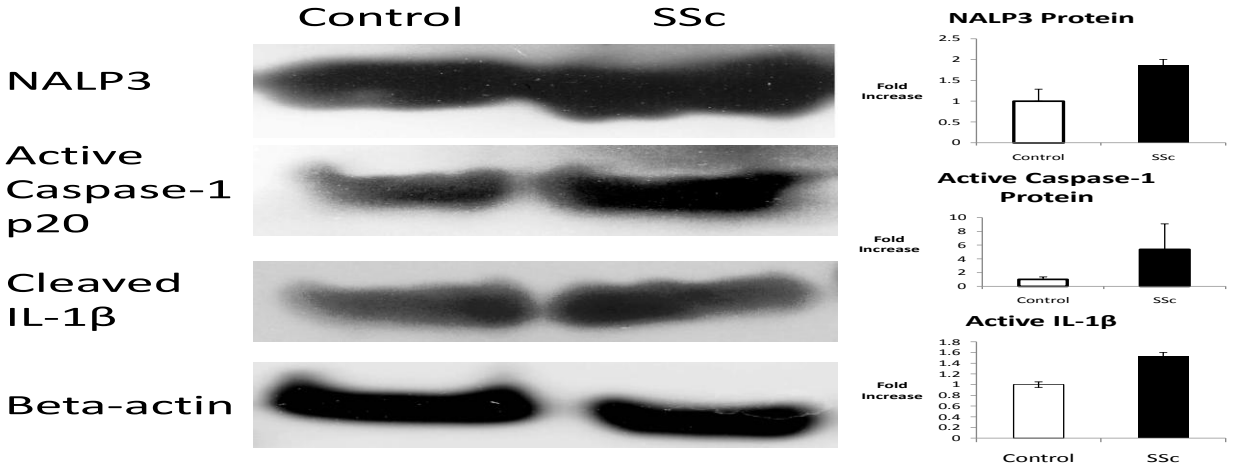

Figure 7. NALP3 and active CASP-1 proteins are elevated in SSc dermal fibrosis. Early passage dermal fibroblasts were lysed and the proteins size fractionated on a polyacrylamide, transferred to PVDF, and probed with antibodies against NALP3, the active caspase-1 p20 fragment, and β-actin. Band intensities were measure by ImageJ and normalized to β-actin expression. In SSc dermal fibroblasts (n=2), more NALP3 and active CASP-1 protein is expressed suggesting that the inflammasome is activated and participating in fibrosis. Bar graphs show pooled data from 4 SSc fibroblast lines and 4 normal lines.

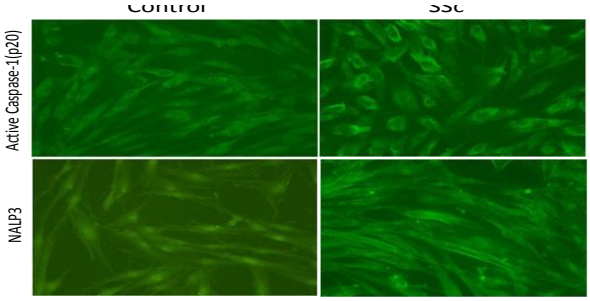

Figure 8. SSc Fibroblasts have increased expression and altered localization of active CASP1 and NALP3. SSc and control fibroblasts were cultured on chamber slides until 90% confluent. Cells were fixed and stained with active CASP1 or NALP3. Cells were viewed with an epi-fluorescent microscope and images were taken at 200X magnification. Note the increased staining of both CASP1 and NALP3. Also note the altered localization of NALP3 protein from the nuclear region in the controls to what appears to be stress fibers in SSc.

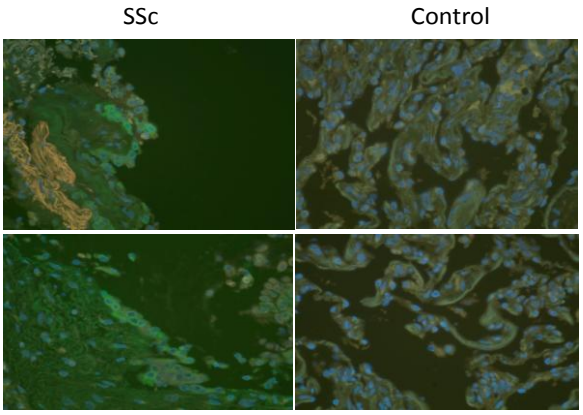

Figure 9. SSc lung tissue has increased expression of active CASP1 p20 subunit. SSc and control lung tissue was stained for active CASP1 protein as described above. Tissues were viewed with an epi-fluorescent microscope and images were taken at 200X magnification. Note the increased green staining of active CASP1 in the tissue of the SSc lung.

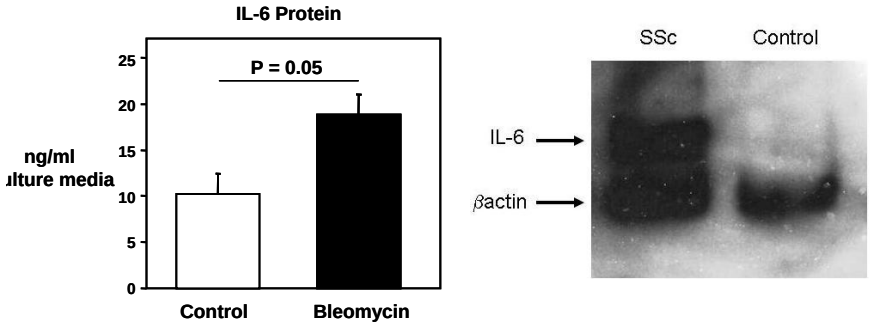

Figure 10. IL-6 production by human fibroblasts is enhanced by bleomycin. Left: Fibroblasts from normal skin were treated overnight with 100nM bleomycin. IL-6 was assayed in the culture media by commercially available specific ELISA. Pooled data from human fibroblast from n=5 healthy donors shown. Right: Western blot for IL-6 in SSc and control fibroblasts

Research Project 2: Project Title and Purpose

Developing Therapies for Treating Hereditary Spastic Paraplegia - The project goals are to:
1. Identify the deficits in nerve cell shape as well as the transport of substances within nerves when DNA is expressed in the nerve that comprises mutant forms of a protein called spastin that goes awry in a disease called hereditary spastic paraplegia.
2. Test various potential therapies for alleviating these deficits, once identified, in order to provide a basis for the development of new therapies for treating patients with the disease.

Duration of Project

1/1/2009 - 12/31/2009

Project Overview

Spastin (the gene whose mutations are the most common cause of hereditary spastic paraplegia) has two start codons, and hence produces a full-length isoform called M1 and a slightly shorter isoform called M85. Interestingly, M85 is the exclusive isoform found throughout the nervous system during development, and throughout almost all of the nervous system in the adult. M1 is only present in the adult spinal cord, which is where the corticospinal tracts are located. Thus, our hypothesis is that mutations to M85 are harmless but when M1 bears the same mutation, it becomes abnormally folded and produces cytotoxic effects. Newer data from our lab suggests that the mutant forms of M1 are also not degraded properly, so they build up in the adult corticospinal tracts. Despite these compelling findings, the medical community is still mainly focused on the idea that the disease is caused by "not enough microtubule-severing." We think this is entirely wrong, and that therapies based on augmenting microtubule-severing are doomed to failure. Rather, we believe the correct strategy is either to remove spastin altogether from these neurons (using RNAi) or to identify precisely which part of the molecule is toxic, and to somehow offset the toxicity. If we are correct about this, we believe that pursuing this line of investigation could very well make Drexel University a world-class center for the development of therapies for treating this debilitating neurodegenerative disease.

Specific Aim 1. Develop a cell culture system based on rat cortical neurons that display robust morphological symptoms of degeneration similar to those observed in the corticospinal tracts of human patients with hereditary spastic paraplegia. This will be done by expressing pathogenic spastin mutants in these neurons, and then using standard morphometric and live-cell imaging assays to measure deficits in parameters such as axonal growth and transport of organelles.

Specific Aim 2. Determine whether pathogenic neurons display "recovery of function" when they are treated with potential therapies**.** Potential therapies will include RNAi as well as small molecular inhibitors to block the toxic regions of the mutant spastin molecules.

Principal Investigator

Peter W. Baas, PhD
Professor of Neurobiology and Anatomy

Drexel University College of Medicine
2900 Queen Lane
Philadelphia PA 19129

Other Participating Researchers

Joanna Solowska, PhD, Terry Heiman-Patterson, MD - employed by Drexel University College of Medicine

Expected Research Outcomes and Benefits

We believe this project will show convincingly that hereditary spastic paraplegia is not caused by haploinsufficiency but rather by cytotoxic properties of the mutant spastin protein. This puts us in an ideal place to argue for therapeutic strategies that no other lab has considered. This endeavor will improve the health status of people suffering from hereditary spastic paraplegia, and may also have impact on other diseases in which toxic mutant proteins give rise to neurodegeneration.

Summary of Research Completed

Spastin, the product of the gene whose mutations are the most common cause of hereditary spastic paraplegia (HSP), is a microtubule-severing protein. One major hypothesis for spastic paraplegia is that the "loss of function" of spastin leads to axonal degeneration. This would presumably relate to the inability of spastin to sever microtubules where and when needed in the adult nervous system. Another possibility is that the dysfunctional mutant forms of spastin have a cytotoxic "gain of function" effect on the relevant neurons. We have documented a major difference in the isoform composition of spastin in the adult spinal cord that may explain why the adult corticospinal tracts fall victim to potential "gain of function" effects not observed elsewhere in the developing or adult nervous system. During this period of CURE funding, we conducted research that ultimately led to external funding to move forward on the project and publishing additional papers in 2010 on spastin function and HSP.

<u>Human spastin constructs</u>
To perform our studies, we developed a panel of new human spastin constructs encoding wild type (WT) spastin or spastins with mutations located outside of the AAA-domain, identical to the mutations found in HSP-SPG4 patients (Fig. 1A). The human SPG4 gene has two start codons that produce a long isoform termed M1 and a shorter protein lacking the first 86 amino acids, termed M87. To express M1 and M87 spastin isoforms simultaneously, we prepared Group-I WT or mutated spastin constructs that include 221 base pairs of 5'UTR with an upstream open reading frame (uORF) containing ATG start codon in a good Kozak's consensus sequence gttATGg and endogenous Kozak's sequences at M1 and M87 translation initiation sites. The ATG start codon in uORF was mutated to ATC in Group-II spastin construct or deleted from Group-III spastin constructs (Fig. 1A). In order to be able to express WT or mutated M1 and M87 isoforms separately, we cloned cDNA encoding M1 or M87 into pCMV-Tag vector, generating Group-IV and Group-V constructs. In these constructs, endogenous M1 or M87

Kozak's sequences were replaced by perfect Kozak's sequences provided by c-myc tag (Fig. 1A). Transcription of spastin mRNA in all constructs is driven by a strong CMV promoter.
To study the effects of mutations on microtubule-severing activity of human spastin isoforms, we chose to use RFL-6 rat fibroblasts. While these cells do not perfectly reflect the conditions within neurons, they have several advantages for the present studies. Unlike cultured neurons, this cell line expresses very little endogenous spastin, undetectable when compared to over-expressed human spastins (Fig. 1B lane C). Thus, results from our functional experiments in these cells could be interpreted in terms of the ectopically expressed spastin isoforms and mutants, without the complication of endogenous spastin. In addition, these cells allowed us to use the Sp/AAA antibody directed against amino acids 337-465 in AAA domain, which are identical in rat and human spastins, to study the expression levels and stability of human spastin isoforms. The flat morphology of RFL-6 cells also affords greater resolution for observations and measurement of microtubule levels.

Transfection of RFL-6 cells with the WT Group-I construct resulted in simultaneous expression of low levels of M1 and M87 spastin isoforms (Fig. 1B lane I). In the Group-I constructs, the M1 ORF starts with an AUG with Kozak's sequence deviating significantly from the consensus motif, with neither the purine in position –3 nor the guanine in position +4. This leads to a leaky scanning of the first AUG and preferred initiation of translation at the second AUG with a guanine in position +4. Moreover, uORF can further reduce translation from the M1 AUG resulting in a low level of M1 expression. Consistent with this idea, mutation of AUG in the uORF to AUC (Group II) as well as deletion of uORF (Group III) resulted in considerably higher expression of both WT M1 and M87 spastin isoforms (Fig. 1B lane II and III). Replacement of the endogenous imperfect Kozak's sequences by a good Kozak's sequence, as in Group IV constructs, further increased levels of WT M1 spastin expression. In contrast, such replacement did not increase expression levels of WT M87 spastin (Group V) (Fig. 1B lane IV and V). Particularly high levels of WT M1 protein detected in cells transfected with Group-IV construct might be attributed to increased translation of M1 from AUG codon in the context of a good Kozak's sequence, accumulation of insoluble M1 aggregates resisting degradation, or both. The expression levels of WT spastin isoforms encoded by Group I-V constructs, normalized against GAPDH expression to adjust for number of cells used for Western blotting, are presented in Figure 1C. Transfection efficiency as assessed by number of spastin positive cells per 200 cells was about 15-17% for all constructs. Group IV and V constructs allow to study severing activity of spastin isoforms expressed individually while group I-III constructs provide the unique opportunity to study interactions between untagged spastin isoforms expressed simultaneously at lower levels.

<u>Human spastin mutations associated with HSP-*SPG4*</u>
To assess microtubule-severing activity of spastins with mutations that lie outside of the AAA-domain, we performed site-directed mutagenesis to create E112K, L195V, S44L and 46Stop mutations, identical to the mutations in HSP-*SPG4* patients (Fig. 1D). Mutation Glu112Lys (E112K) in exon 1 affects a moderately conserved residue just upstream from the MIT domain (Fig. 1A). This mutation is associated with a case of pure HSP that started at the age of 41 and had a severity score 3 on a 4-point scale.

Mutation Leu195Val (L195V) in exon 3 affects a conserved residue in the MIT domain (Fig.

1A). This mutation was found in two cases of pure HSP with the onset of symptoms at the ages of 37 and 55 years. The severity score was 2 and 3 on a 5-point scale where 1 indicates normal or very slight stiffness in the leg and 5, wheel chair bound.

Mutation Ser44Leu (S44L) is located in the N-terminal region of M1 isoform in exon 1 (Fig. 1A). This mutation is asymptomatic when heterozygous and is associated with a case of pure HSP with mild symptoms first noticed at the age of 60 years when homozygous. When present in addition to another mutation in the second spastin allele, the S44L mutation is associated with early childhood onset of HSP.

A frame-shift 46Stop mutation in exon 1 (Fig. 1A) is associated with a case of pure HSP. The premature stop codon created as a result of the mutation is located outside of M87 coding region and should only truncate M1.

Microtubule-severing activity of WT and mutated spastins: In one major part of our study, we tested the microtubule-severing activity of the wild-type and spastin mutants, both M87 and M1 forms, by expressing them in RFL-6 rat fibroblasts. The results were reported in the previous summary of progress.

These results demonstrated that the human M87 isoform has higher microtubule-severing activity, compared to the M1 isoform, and that the mutations studied here have minimal impact, if any, on the microtubule-severing properties of either protein.

<u>Expression levels of WT and mutated spastin isoforms.</u>
Despite the conclusion above, it was possible that while the enzymatic activity was not changed, the mutated spastins were more prone to misfolding and/or aggregation, and therefore more likely to be degraded by the ubiquitin-proteasome system (UPS) or by autophagy. In such a scenario, it is not the loss of enzymatic activity but the lower levels of active spastins that might affect the level of microtubule severing. To investigate this possibility, we first performed Western blot analyses using extracts from RFL-6 cells transfected with Group-IV or Group-V constructs. The results indicated that there was no decrease in levels of M1 or M87 mutated proteins compared to WT M1 or M87. Group-IV and V constructs however, expressed very high levels of spastins, particularly of the M1 isoform, and these high levels of exogenous proteins might overwhelm the transfected cells ability to degrade them. Some of this work was underway but not yet completed in the previous summary of progress. In brief, the results of the now completed studies show that there are *SPG4* mutations associated with HSP that do not affect spastin microtubule-severing activity or expression levels, and therefore clinical symptoms observed in patients carrying these mutations cannot be explained by haploinsufficiency. Interestingly, there was a significant difference in accumulation of M1 and M87 isoforms. Inhibition of ubiquitin-proteasome system (UPS) by MG132 resulted in roughly a 50% increase of the levels of WT or mutated M87 and about three-fold increase of the levels of WT or mutated M1. This result indicates that M87 is the more metabolically stable isoform, while M1 is more readily degraded when expressed at low levels in cells with an active UPS. However, when the UPS system is compromised, the accumulation of M1 is significantly greater than is accumulation of M87 isoforms.

In terms of even greater relevance to human patients, we have now compared spastin expression in control human cerebral cortex and spinal cord with that in the spinal cord of an HSP-*SPG4* patient (Fig. 2). Human M87 spastin was expressed both in control cerebral cortex and spinal cord. A significant level of M1 expression however, was detected only in control spinal cord and not brain. This expression pattern of human spastin isoforms resembles the distribution of M1 and M85 spastin isoforms in mouse tissues. Besides 60 kDa M87 and 68 kDa M1 spastin, a 64 kDa band (M1D4), likely corresponding to spastin translated from a common splice variant lacking exon 4, was also found in the control spinal cord. The HSP spinal cord samples were obtained postmortem from a patient carrying a splice mutation that causes in-frame skipping of exon 11. Exon 11 encodes 31 amino acids and the M1 isoform missing 31 amino acids should migrate as a band of approximately the same molecular weight of 64 kDa as M1D4, which is missing 32 amino acids. Interestingly, a prominent band of this size was present in the thoracic but not cervical spinal cord from the HSP-*SPG4* patient. Because the intensity of this band not only greatly exceeded the intensity of M1D4 but also M87 band, we concluded that this band might represent accumulated M1D11. The protein band corresponding to the M87 isoform lacking 31 amino acids encoded by exon 11 was not found. That might indicate that M87D11 but not M1D11 is prone to degradation. Interestingly, no prominent 64 kDa-band was found in the cervical spinal cord from the same patient. This suggests that mutated M1D11 accumulates preferentially in the more distal axons. If the mutated M1 spastin is cytotoxic (as we have proposed), this observation may explain why axonal degeneration in HSP classically occurs as a "dying back" from the synapse.

<u>Co-aggregation of M1 and M87 spastin</u>

The possibility that mutated M1 spastin might accumulate begs the question as to whether such accumulated M1 affects M87 microtubule-severing activity. When compared with M87, M1 has an ability to form presumably insoluble aggregates. To compare solubility of individually expressed WT and mutated M1 and M87 isoforms, we transfected cells with Group-V construct expressing WT or mutated M87 spastin or with Group-IV construct expressing WT or mutated M1 spastin. Transfected cells were then extracted with cell lysis reagent M-PER. After centrifugation, supernatants were collected and pellets were re-suspended in SDS-PAGE sample buffer. As expected, Western blot analysis revealed that majority of WT and mutated M87 is soluble and remains in supernatants while WT and mutated M1 are evenly divided between soluble fraction in supernatants and insoluble fraction in pellets.

To test whether WT or mutated M1 affects the solubility of co-expressed M87, we transfected cells with Group-III constructs that simultaneously express elevated levels of M1 and M87. Western blot analyses revealed that the M87 isoform, which is present predominantly in supernatant when expressed alone, becomes evenly divided between supernatant and pellet when expressed in the presence of M1. These results indicate that the solubility of M87 can be modulated by M1. The levels of insoluble M87 did not seem to be affected by HSP-related mutations, and no significant differences in solubility were found between WT and mutated spastins. Interestingly, in cells transfected with the construct co-expressing WT M87 and a short 46-amino acid fragment of M1 (M1Stop mutant), some M87 isoform was found in the pellet, suggesting that even a very short fragment of M1 (not recognized by our anti-spastin antibody directed against AAA domain) can co-aggregate with M87. We do not know if M1/M87 co-aggregation is in any way specific, but it is reasonable to assume that M87 in the insoluble

fraction does not sever microtubules. Therefore, accumulated M1 might decrease the severing activity of M87 by trapping this isoform in insoluble aggregates.

These results demonstrate that there are spastin mutants associated with HSP that retain their full ability to sever microtubules, which is clearly inconsistent with haploinsufficiency. While it is possible that the symptoms of HSP could still be exacerbated by diminution in microtubule-severing activity in the corticospinal tracts, even the combination of neurotoxicity and decreased microtubule-severing activity of mutated spastin cannot explain the great differences in onset ages and symptom severity characteristic of HSP-*SPG4*. It seems inescapable that differences must exist among patients in their ability to compensate for potential losses of spastin activity and/or their ability to tolerate or dispose of toxic proteins. Gaining insight into these mechanisms, particularly the processes involved in the disposal of misfolded proteins might prove beneficial not just for the HSP-*SPG4* patients but also to patients suffering from other neurodegenerative disorders. The mutants in the present work are not ideal for studying the merits of the gain-of-function model because they would certainly cause notable microtubule loss if ectopically expressed in neurons. Therefore, our next step is to generate a panel of tools corresponding to human disease-related mutations that do impair the microtubule-severing activity of spastin so that the mechanisms of toxicity can be studied in neuronal cells.

Figure 1. Spastin constructs prepared in our laboratory. See text for details.

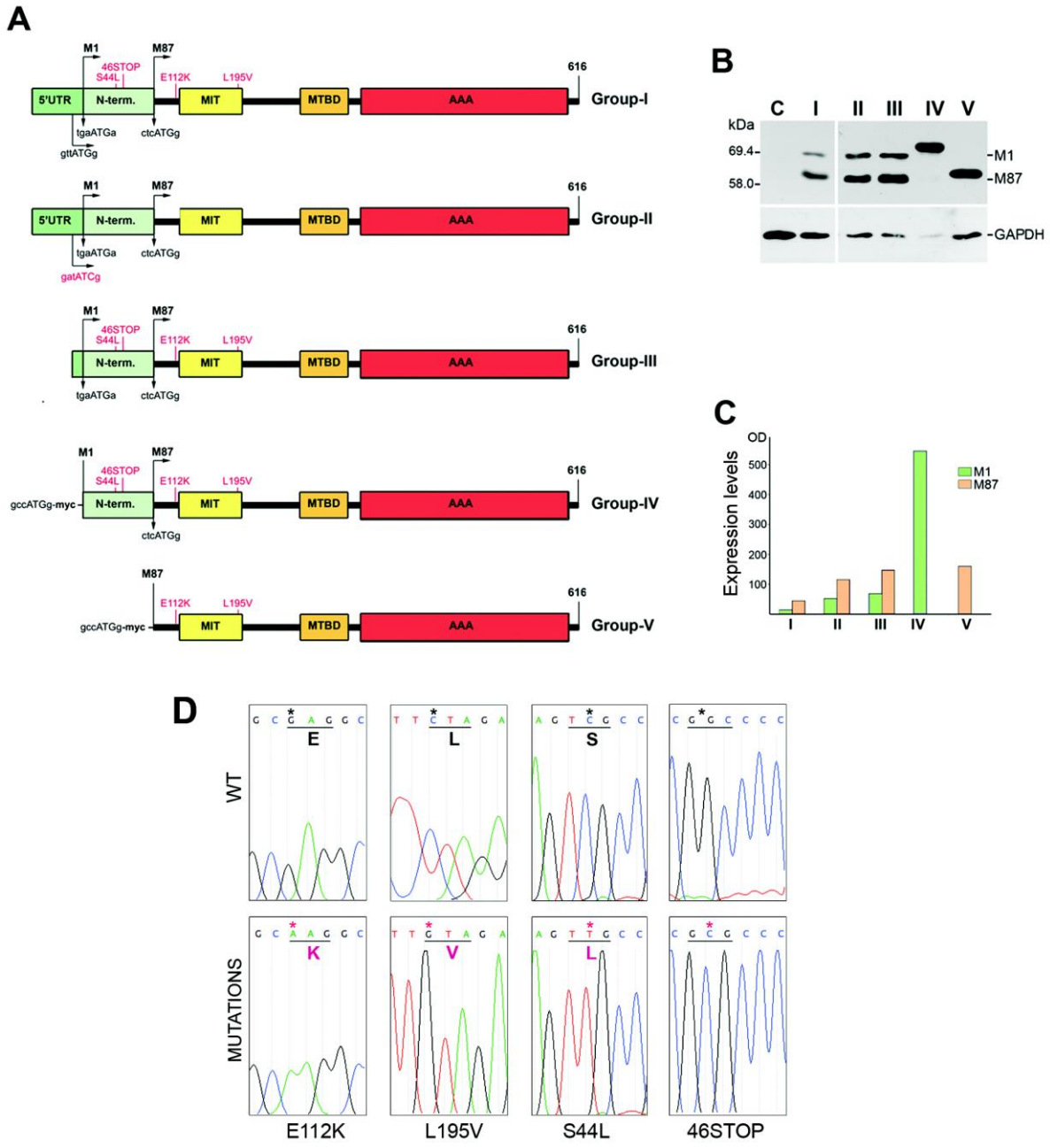

Figure 2. Spastin isoforms in control human and HSP human patient. See text for details.

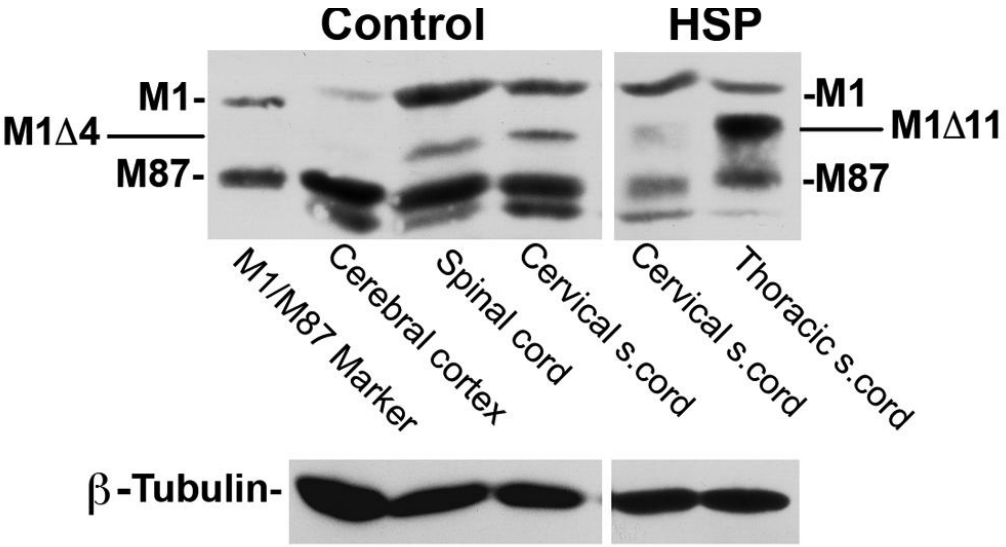

Research Project 3: Project Title and Purpose

Role of CTF18 in Female Germ Cell Development and Fertility - Infertility is a major medical concern that affects about 1 of every 10 individuals of childbearing age worldwide. Although a significant proportion of infertility is accounted for by identifiable causes, the molecular basis of these defects is often not known or well characterized. Ovulatory dysfunction and diminished ovarian function in infertile women, and low sperm count in infertile men are examples. It is becoming increasingly clear that many more disorders in medicine, including infertility, have a genetic basis than was previously realized. It is our goal to advance the field so that a better understanding of the underlying defects of infertility disorders will lead to improved treatments.

Anticipated Duration of Project

1/1/2009 - 12/31/2010

Project Overview

Better understanding of the role of *CTF18/Chtf18* in females will broaden our knowledge of the underlying molecular aspects of oogenesis and folliculogenesis, and in doing so will shed light on the underlying defects of infertility in women. Thus, the specific aims of this proposal are:

1. To determine the function of *Chtf18* in mouse oogenesis and folliculogenesis *in vivo*. *Hypothesis: Chtf18 is a critical mediator of oogenesis and folliculogenesis, and its absence causes follicle degeneration.* We will assess oocyte and follicle development in ovaries of *Chtf18*$^{-/-}$ and wild-type females using histological criteria and immunofluorescence-microscopy.

The underlying cause(s) of a decreased number and aberrant appearance of follicles seen in *Chtf18*-deficient ovaries will be determined. Developmental competency of oocytes and hormonal profiles will also be evaluated.

2. To determine the cause of subfertility in *Chtf18*$^{-/-}$ females.
Hypothesis: Premature separation of homologous chromosomes in meiosis results in aneuploidy and embryonic death leading to significantly impaired fertility. Oocytes will be studied immunocytologically for chromosome segregation defects and embryos will be evaluated for aneuploidy.

Principal Investigator

Karen M. Berkowitz, MD
Assistant Professor
Drexel University College of Medicine
245 N. 15th Street, Mail Stop 495
Philadelphia, PA 19102

Other Participating Researchers

None

Expected Research Outcomes and Benefits

We have generated an experimental system to study CTF18 (known as Chtf18 in the mouse), an evolutionarily conserved gene that is crucial for fertility in the fruitfly and that it is essential for the accurate segregation of chromosomes in yeast. We recently demonstrated that Chtf18 is necessary for fertility and accurate chromosome segregation in the mouse. In addition, almost half of mice lacking Chtf18 die during embryonic development. These data strongly suggest that Chtf18 plays a significant role in normal segregation of chromosomes during development of germ cells (i.e. the cells destined to become eggs and sperm). Defects in these processes are known to contribute greatly to causes of an abnormal chromosome number in offspring, and an abnormal chromosome number often leads to birth defects and/or pregnancy loss. Thus, a better understanding of Chtf18 and its role in germ cell development and chromosomal segregation will shed light on one of the most frequent types of genetic defects that occur during reproduction. Therefore, these studies will provide insight into human infertility and reproductive disorders, ultimately leading to better treatments.

Summary of Research Completed

Data collected from each of the following aims (described below) have been presented at the following meetings during the reporting period: 1) Drexel University College of Medicine Discovery Day, Philadelphia, PA, October 7, 2009; 2) The 57th Annual Meeting of the Society of Gynecologic Investigation, Orlando Florida, March 24-27, 2010 (Oral presentation).

Specific Aim 1. To determine the function of *Chtf18* in mouse oogenesis and folliculogenesis *in vivo*.

To ascertain the role that *Chtf18* plays in both mouse oogenesis and folliculogenesis we are examining ovarian follicle development, developmental competency of oocytes, and hormonal function of *Chtf18*$^{-/-}$ females in 3 separate subaims:

1) Evaluation of follicle development. We are evaluating ovaries of *Chtf18*$^{-/-}$ females compared to wild-type controls from embryonic development through adulthood in order to determine the stage(s) at which the defects in follicle development occur. Our studies will also allow us to determine the underlying cause(s) of the defects. *Chtf18*$^{-/-}$ ovaries are smaller, contain fewer follicles than wild-type ovaries, and are morphologically abnormal (Figure 1). We are counting ovarian follicles to quantitate the differences observed at different stages of development, and follicles are being scored and categorized as primordial, primary, secondary, and antral according to morphological criteria. Dissected ovaries are fixed in Bouin's solution or 4% paraformaldehyde solution at 4°C overnight, embedded in paraffin blocks, sectioned, and viewed by light microscopy. Ovarian sections used for histological evaluation are stained with hematoxylin and eosin. Ovaries from *Chtf18*$^{-/-}$ and wild type control females at postnatal day 21, 3 and 6 months of age have been collected, processed, paraffin embedded, and counted. We found significantly decreased numbers of primordial follicles at postnatal day 21 (Figure 2) in *Chtf18*$^{-/-}$ compared to wild-type ovaries. We also found a significant reduction in the numbers of primary and secondary follicles of *Chtf18*$^{-/-}$ ovaries at 3 months of age and in the numbers of primary and antral follicles of *Chtf18*$^{-/-}$ at 6 months of age (Figure 3). Our data from antral follicle counts and secondary follicle counts in *Chtf18*$^{-/-}$ ovaries at 3 and 6 months of age, respectively, are trending toward statistical significance and demonstrate a large size effect, suggesting that these results are biologically relevant. Our sample sizes are small and so we are continuing to collect data at these time-points. We had proposed counting follicles in females at 9 months of adult age, but have found that follicle numbers are so low and degenerated even in wild type females that data from this time-point is not meaningful. Neonatal ovaries are currently being examined and follicles counted at postnatal day 7 and during embryonic development. We had proposed counting follicles in females at 6 wks of age, but have already found significantly decreased numbers of primordial follicles in the ovaries of *Chtf18*$^{-/-}$ females at postnatal day 21 indicating that the early follicle pool is already significantly diminished in *Chtf18*$^{-/-}$ female mice. Our data strongly suggest that *Chtf18* is necessary to maintain the early and developing ovarian follicle pools in female mice, and they indicate that *Chtf18* plays significant roles in mammalian folliculogenesis.

2) Assessment of the competency of oocytes.
Oocytes are cultured and allowed to grow and mature *in vitro* in order to assess the developmental competency of *Chtf18*$^{-/-}$ oocytes. In our original research plan, we had proposed collecting antral follicles from ovaries of 6-week-old eCG-primed females. However, to improve the yield of antral follicles containing fully-grown oocytes, we are collecting oocytes at 3 wks of age (an accepted alternative age in the literature), which provides significantly greater numbers of oocytes to collect and culture (data not shown). Female mice are given a single injection of 5 units (U) of eCG (equine chorionic gonadotropin) (Calbiochem, La Jolla, CA) intraperitoneally, and then sacrificed 48 hours later. Ovaries are collected in medium and then

punctured with 27G½ inch needles to release antral follicles. The oocyte-cumulus cell complexes are then collected and transferred to fresh medium. Cumulus cells are mechanically removed from oocytes by pipetting, and cumulus-free oocytes are then incubated in fresh medium at 37°C in 5% CO_2 and air. The total number of oocytes per genotype is recorded, and oocytes are scored for the following stages of meiotic progression (Figure 4): presence of a germinal vesicle (GV), germinal vesicle breakdown (GVB), or extrusion of first polar body at collection time and after 16 hours in culture. GVB signifies resumption of meiosis I, and extrusion of a polar body signifies progression to metaphase II. Progression is measured by calculating percentages of oocytes reaching each stage (i.e. number of oocytes for each stage divided by the total number of oocytes placed into culture for each genotype. Chromosomes and spindle structure of oocytes will soon be examined. Stages are assessed morphologically with brightfield microscopy using Nomarski optics. The experiment will be performed with three independent replicates per genotype. In order to evaluate the ability of *Chtf18*$^{-/-}$ oocytes to progress in meiosis, we have developed an *in vitro* system of cultured mouse oocytes. Due to genetic influences of our mouse strain (hybrid of C57Bl/6; 129Sv), it has taken significant time for us to determine and optimize the conditions in which oocytes from our wild-type mice develop and progress. Multiple collection and culture conditions have been utilized, and we have recently found that a significantly greater number of wild-type oocytes progress to meiosis I and II when they are collected in MEMα medium and cultured in CZB medium (Figure 5). Now that we have determined optimal oocyte collection and culture conditions, we can collect data from *Chtf18*$^{-/-}$compared to wild-type female mice.

3) Hormonal evaluation. As an initial assessment of hormonal function, we are verifying that *Chtf18*$^{-/-}$ females cycle normally. Assessment of estrus cycle stages and length are being made for *Chtf18*$^{-/-}$ and wild-type females by cytological analysis of vaginal smears. We are also evaluating and comparing the endocrine profiles of *Chtf18*$^{-/-}$ with wild-type mice. Serum levels of steroid hormones (including estradiol and progesterone) and gonadotropins (including FSH and LH) will be measured in reproductively mature mice. At least three mice of each genotype will be evaluated.

Specific Aim 2. To determine the cause of subfertility in *Chtf18*$^{-/-}$ females.

1) Chromosomal localization of CTF18 in meiosis. As an initial step in determining the role of CTF18 protein in chromosome segregation and dynamics, we will localize CTF18 protein in chromosomes during meiosis. Embryonic ovaries at 17.5 dpc, when meiosis has progressed to the pachytene stage of meiosis are being utilized to prepare surface spread nuclei from oocytes. Each pair of ovaries is dissected from female embryos and placed into a 50 ⌠l drop of hypotonic buffer for 40 minutes. Each pair of ovaries is then moved to a 20 ⌠l drop of 100 mM sucrose, and the ovaries poked with a 27G½ inch needle to release oocytes. Another 40 ⌠l is added to resuspend the cells and 25 ⌠l each of the suspension is placed on each of two slides previously dipped in fresh 2% PFA/0.15% Triton X-100. Slides are placed on a flat surface and allowed to air-dry. For immunofluorescence, surface nuclei spread are blocked (1X PBS containing 10% donkey serum, 3% BSA, 0.05% Triton X-100) for 1 hour at room temperature, and then incubated with primary antibodies overnight at 4°C. We are utilizing rabbit anti-mouse CTF18 and guinea pig anti-mouse-SYCP2 (from P.J. Wang, University of Pennsylvania School of Veterinary Medicine), which stains the axial chromosomal cores of the synaptonemal complex.

Slides will be viewed with fluorescent microscopy. Conditions for the use of anti-mouse CTF18 are currently being optimized.

2) Evaluation of chromosomes in meiosis. We have confirmed that homologous chromosome pairing and synaptonemal complex formation is normal by examining *Chtf18*$^{-/-}$ chromosomes in oocytes from embryonic ovaries at 17.5 dpc during prophase I (Figure 6). We have also begun to analyze surface spread nuclei from oocytes of mice at 18.5 dpc (Figure 6) or P0, when the majority of oocytes meiosis has arrested in the diplotene phase of meiosis I. Immunofluorescence microscopy is performed (as described above) with rabbit anti-mouse SYCP1 (Abcam, Inc.) and guinea pig anti-mouse-SYCP2 antibodies.

3) Evaluation of embryos for aneuploidy. Since we hypothesize that subfertility observed in *Chtf18*$^{-/-}$ females results from chromosome segregation defects leading to aneuploidy and ultimately embryonic death, we will determine the time point at which this occurs. Since we speculate that loss occurs much earlier than E17.5, we sacrificed *Chtf18*$^{+/-}$ females (mated with *Chtf18*$^{+/-}$ males) at E9.5, and collected and genotyped embryos present in order to determine when embryonic death might occur. We found that the ratio of observed/expected *Chtf18*$^{-/-}$ embryos was significantly less than those of *Chtf18*$^{+/-}$ or *Chtf18*$^{-/-}$ embryos (data not shown). Since we did not note obvious resorption at this embryonic age, we speculate that loss occurs at an earlier time point. In order to determine whether loss occurs prior to implantation, we are currently breeding eCG-primed *Chtf18*$^{+/-}$ females with *Chtf18*$^{+/-}$ males, and collecting and culturing blastocysts at E3.5 (Figure 7). Cultured blastocysts will then be genotyped and karyotyped. We are currently optimizing our *in vitro* system for culturing blastocysts.

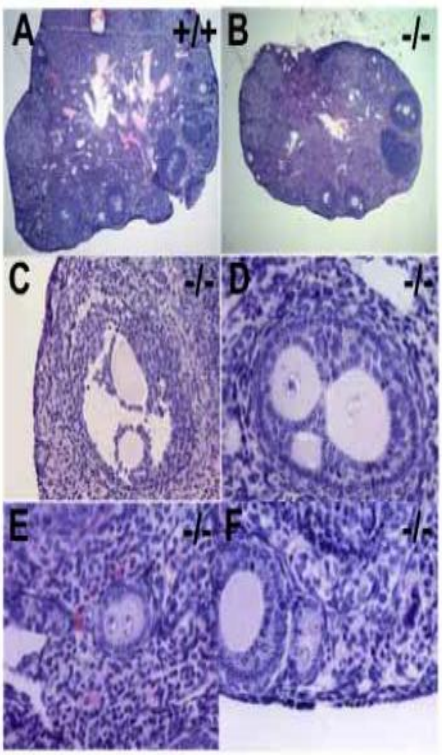

Figure 1. Ovaries from *Chtf18*$^{-/-}$ females are are morphologically abnormal. Sections of ovaries stained with hematoxylin and eosin from wild-type (A) and *Chtf18*$^{-/-}$ (B-F) females are shown. Ovaries from *Chtf18*$^{-/-}$ females (B) are smaller and contain fewer follicles than wild-type females (A) All stages of follicular development are seen, but many of the follicles appear to be degenerating (C) while some appear to be binucleate, consistent with premature release from meiotic arrest (C-F).

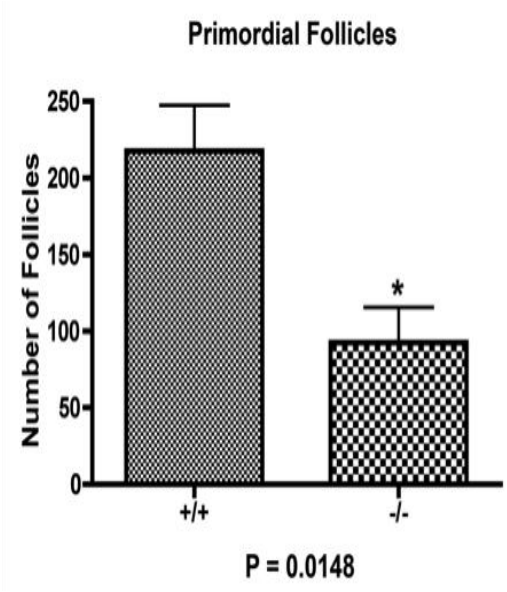

Figure 2. Numbers of primordial follicles are significantly decreased in *Chtf18*$^{-/-}$ ovaries at postnatal day 21.

Figure 3. Numbers of primary, secondary, and antral follicles are decreased in *Chtf18*$^{-/-}$ ovaries at 3 and 6 months of age.

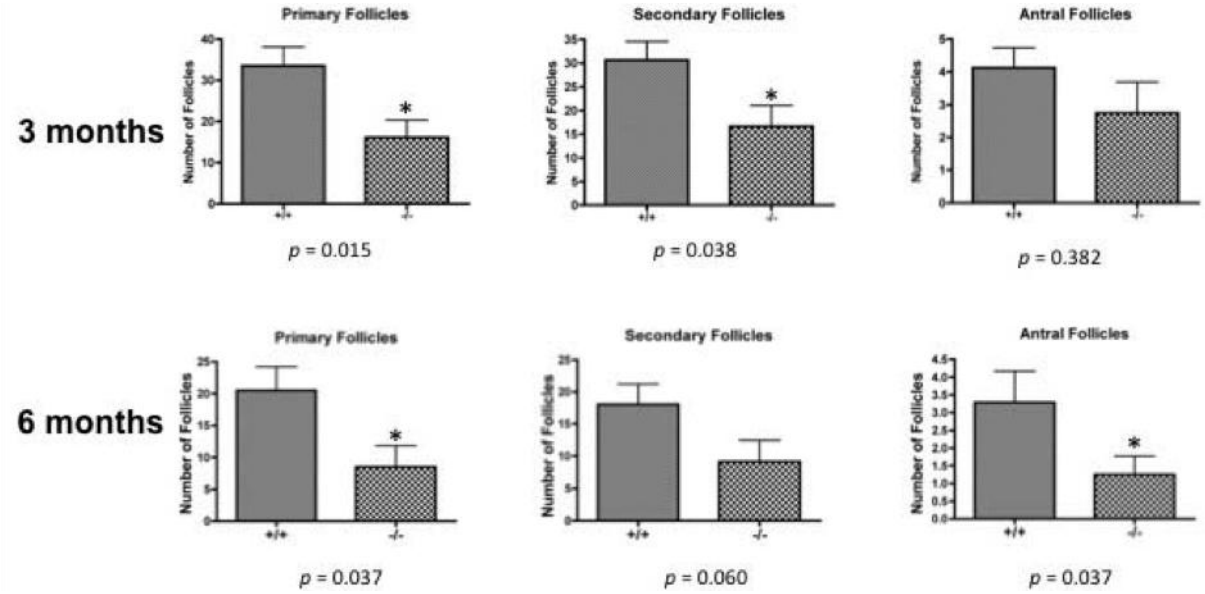

Figure 4. *In vitro* maturation of *Chtf18* wild type oocytes. Oocytes cultured from *Chtf18* wild type ovaries show the germinal vesicle stage (A), germinal vesicle breakdown indicating progression to metaphase I (B), and polar body extrusion indicating progression to metaphase II (C).

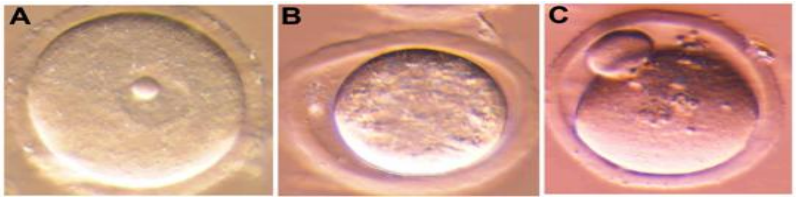

Figure 5. Significantly greater numbers of oocytes progress in meiosis when collected in MEMα medium and cultured in CZB medium. Oocytes from *Chtf18* wild type females were collected and cultured in 4 different combinations of media

Oocyte stage	**1**	**2**	**3**	**4**	**P value**
GV	255	155	107	321	
MI	147 (57.6%)	125 (80.6%)	88 (82.2%)	313 (97.5%)	P < 0.001
MII	50 (19.6%)	85 (54.8%)	41 (38.3%)	80 (24.9%)	P < 0.001

Media used:	Collection	Culture
1	MEM with milrinone	CZB
2	MEM without milrinone	CZB
3	MEMα with milrinone	MEMα
4	MEMα without milrinone	MEMα

Figure 6. Evaluation of meiosis reveals the presence of univalent chromosomes in *Chtf18*$^{-/-}$ oocytes during prophase I. Surface spread nuclei from wild-type (+/+) and *Chtf18*$^{-/-}$ (-/-) oocytes were stained with antisera against SYCP1 (red) and SYCP2 (green) during the pachytene (A-F) and diplotene (G-I) stages of prophase I. SYCP1 localizes to central elements of the synaptonemal complex and SYCP2 localizes to the axial/lateral elements of the synaptonemal complex. The merged images (C and F) demonstrate that formation of the synaptonemal complex occurs normally and that synapsis is complete during the pachytene stage in both *Chtf18*$^{+/+}$ (A-C) and *Chtf18*$^{-/-}$ (D-F) oocytes. While the diplotene stage is normal in *Chtf18*$^{+/+}$ oocytes (G-I), we detected the presence of possible univalent chromosomes (arrows in L), a sign of premature separation of homologous chromosomes in *Chtf18*$^{-/-}$ oocytes (J-L).

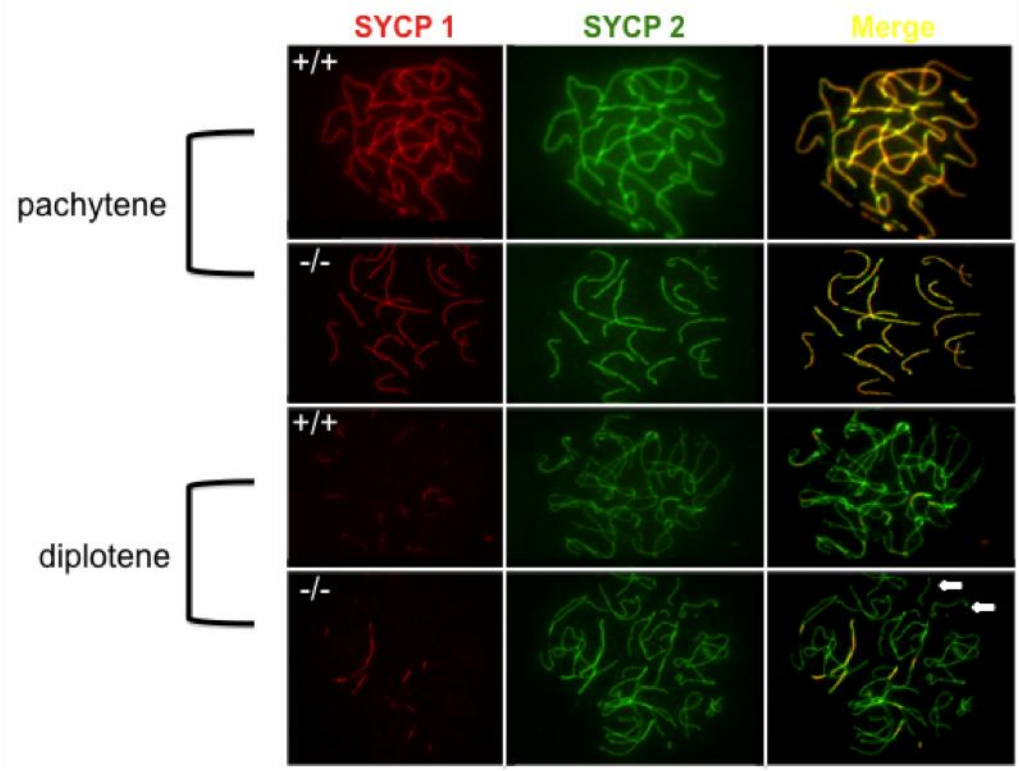

Figure 7. Blastocysts collected from the oviducts of *Chtf18*$^{+/-}$ female mice**.** Cultured blastocysts exhibited attachment (A) and hatching (B).

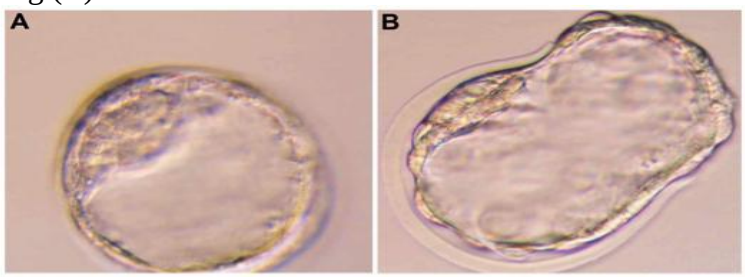

Research Project 4: Project Title and Purpose

A Microfluidic Model of Drug-induced Liver Toxicity - Drug-induced liver injury (DILI) is a common reason for terminating drug development, failing to acquire governmental drug approval, or withdrawing a drug from the market. There is no authentic human liver model for predicting DILI in humans. Attempts to make a human liver model have been impeded by the lack of readily available, large quantities of normal human liver cells. A human liver model that retains normal liver architecture and function, while only requiring small numbers of liver cells, is needed. In this project, we will use rat liver cells and fabricated microchannels to produce a mini-liver unit to test DILI. Our long-term goal is to use parameters derived from studies of the rat mini-liver system to generate a human mini-liver system that can be used for human liver biology and DILI studies.

Anticipated Duration of Project

1/1/2009 - 12/31/2010

Project Overview

The broad objectives and specific aims of this project are: 1). Establish cell growth conditions for layered co-cultures of primary rat hepatocytes and liver sinusoid endothelial cells (LSEC) in a microfabricated, microfluidic environment that mimics a basic functional unit of the liver and 2). Determine the cellular responses of LSEC and hepatocytes in this mini-liver system to Ritonavir exposure.

To achieve these goals, recent advances in microfabrication of mini cell-culture chambers, and construction of microfluidic pumps that can control fluid flow within these chambers, will be combined with techniques for isolation and culture of primary hepatocytes and LSEC to generate layered co-cultures of hepatocytes and LSECs in microchannels. Continuous influx of nutrients and removal of waste and bile will be controlled by microfluidic pumps so that this system mimics the normal microenvironment of a liver sinusoid functional unit.

Hepatocytes and LSEC isolated from rats will be used in this project; rats provide an experimentally tractable system for isolating hepatocytes and LSEC and generating the experimental parameters required to maintain these cells in a microfabricated environment. If required, rat livers can also serve as a source of additional liver-specific cells such as Kuppfer or Stellate cells; inclusion of these might be necessary for generating a fully functional mini-liver unit.

Experimental conditions will first be developed that facilitate the long-term maintenance of functional hepatocytes and LSEC; these will include defining both nutrient and fluid exchange requirements. A thin layer of MatrigelTM that mimics the space of Disse will be used to maintain the layering of the cells. Each cell type will be routinely tested in the mini-liver system to ensure that it retains its liver-specific phenotype and functions. Once established, as an initial evaluation of drug-induced liver injury, cells within this mini-liver system will be exposed to Ritonavir, and the consequence to cell viability or functions will be evaluated. Testing the

cellular response to Ritonavir will demonstrate how this system can be used to test drug-induced liver injury.

The long-term goal of this project is to use experimental conditions derived from studies of the rat mini-liver model to generate a human mini-liver system that recreates the normal cellular, architectural and fluidic microenvironment of a human liver functional unit and serves as a system for analyses of human liver physiology and drug-induced liver toxicity.

Principal Investigator

Michael J. Bouchard, PhD
Assistant Professor
Drexel University College of Medicine
NCB 11312
Dept. of Biochemistry and Molecular Biology
245 North 15th St.
Philadelphia, PA 19102

Other Participating Researchers

Moses Noh, PhD – employed by Drexel University

Expected Research Outcomes and Benefits

We expect that by combining recent advances in microfabrication and microfluidic technologies with techniques for the isolation and culture of normal hepatocytes and liver sinusoidal endothelial cells (LSEC), we will define conditions for creating layered co-cultures of rat hepatocytes and LSEC that mimic a functional liver unit. These cells will be co-cultured in microchannels, and the final functional unit will only require small numbers of cells. The control of fluid influx and efflux by microfluidic pumps, the maintenance of cellular architecture that is similar to that of a normal liver, and the use of small numbers of cells will create a miniaturized liver unit that can be used to study numerous aspects of liver biology as well as liver responses to various drugs. While the outlined project will focus on developing this system with rat liver cells, these studies will establish experimental parameters for generating a similar human mini-liver.

The benefit of this research is that it will define conditions required to construct a much-needed human liver system that recreates the normal architecture and environment of the liver while only using small numbers of human liver cells. Human liver cells are usually acquired from surgically removed livers and are limited in availability. In addition, as a proof-of-principle, this rat mini-liver system will be used to study the toxicity of Ritonavir, a drug that is thought to be harmful to the liver. Ultimately, a human mini-liver system can be used to study general liver biology and well as liver-specific responses to drugs. Considering that drug-induced liver injury is the most common reason from removing a drug from the marker, a system that could be used to evaluate this toxicity prior to actual administration to humans would prevent approval of drugs that are potentially toxic to humans.

Summary of Research Completed

During this period, we have focused on completing generation of a functional mini-liver system containing layered co-cultures of primary rat hepatocytes (PRHs) and liver sinusoidal endothelial cells (LSECs) and have continued to make progress. Our approach has capitalized on the engineering and biological expertise of the principal investigators. We have identified conditions for maintenance of co-cultured PRHs and LSECs in microchannels, including defining growth factor and O_2 requirements, demonstrating maintenance of cell-specific markers, constructing an oxygenator and a continuous perfusion platform, and testing dual microchannel systems. We have also expanded our system to include cultured primary human hepatocytes.

Culture of Primary rat hepatocytes and liver sinusoidal endothelial cells: We previously reported identification of conditions for maintenance of PRHs and LSECs in microchannels but discovered that PRH growth medium was not compatible for LSECs and vice versa. Consequently, we redefined growth medium conditions that allows co-culture of PRHs and LSECs and confirmed that cell-specific mRNA are expressed under these conditions. Confirmation was by reverse-transcriptase polymerase chain reaction (RT-PCR) of isolated mRNAs. In addition, because of continual contamination of LSECs with a low level of other liver cell types and debris from the liver perfusion, we previously were forced to culture LSECs in standard tissue-culture plates, remove contaminants, and then subsequently add the LSECs to microchannels. We have now developed protocols for generating highly purified LSECs that can be directly seeded into microchannels (Figure 1). These procedures include sequential differential centrifugation followed by Percoll gradient purification of the LSECs. We have also developed methods for layering the LSECs over PRHs that are already seeded and have formed monolayers in the microchannels. For this, we defined conditions for overlaying the PRHs with a thin layer of collagen. Specifically, we added collagen diluted in 0.15 mM Hepes buffer to the microchannel containing a monolayer of PRHs, waited 1.5 hours, washed away the collagen, and then added LSECs (Figure 2).

O_2 simulation models: The O_2 concentration decreases from inlet to outlet of a sinusoid; the approximate O_2 gradient spans from ~.084 mol/m^3 to ~.03 mol/m. In order to determine the feasibility of this type of O_2 gradient, numerical simulations were performed in COMSOL Multiphysics 3.5a using the convection/diffusion and the incompressible Navier Stokes modules; the governing equations are Navier Stokes equation and Fick's Second Law of Diffusion. For single microchannels, we simulated a polydimethylsiloxane (PDMS) microchannel with PRHs at the bottom of the channel. A parabolic flow profile was defined with a mean velocity of $1x10^{-4}$ m/s. The medium was assumed to be oxygenated to 0.084 mol/m^3. The O_2 uptake rate of PRHs, the diffusion coefficients of O_2 through PDMS and medium, and the distribution constant between O_2 in air and PDMS were obtained from the literature. The results showed that the O_2 diffusion through PDMS causes the O_2 concentration of the flowing medium to change to a steady state value at the bottom of the channel (Figure 3). This results in a smaller concentration gradient than is seen in the body, suggesting that we may have to alter our configuration in the future to achieve a physiologically relevant gradient. To validate the COMSOL software, we compare our COMSOL simulation result with two existing models in the literature: Allen (2005) and Mehta (2007). We first employed the mathematical model by Allen (2005) assuming uniform velocity in the whole channel and steady-state. Our boundary conditions and governing

equations are the same as Allen's model. The cell uptake rate is assumed to be constant through the channel. The result in Figure 3 shows that oxygen level is decreasing smoothly along the channel, which is similar to Allen's result.

To compare with Metha's simulation (2007), a parabolic flow profile is assumed. The cell uptake rate is simulated by the Michaelis-Menten kinetic model. Oxygen diffuses from the atmosphere to the channel through the PDMS membrane. Oxygen concentration at the outlet is presented in Figure 4. This result shows good agreement with Metha's simulation.

For dual microchannels, the simulation geometry had two flow channels separated by a 10-µm thick membrane on which cells are cultured. The simulation was modeled in a similar fashion as described above with proper boundary conditions at the interfaces between materials; however, the flow is provided in different directions. Initial results showed that both channels have a similar O_2 concentration profile with both quickly decreasing to a concentration of about 0.077 mol/m^3. Oxygen level in the bottom channel is lower than the oxygen level in the top channel since we assume oxygen does not diffuse from bottom into the channel. To verify results, we are currently measuring the fluorescence of an O_2-quenching dye, ruthenium tris dichloride hexahydrate, flowing over cells. We simulated the oxygen concentration using the COMSOL software both in a microchannel and a dual-channel system (Figure 5).

Oxygenator Construction: To investigate the effect of O_2 concentration on liver cells, we also tested the effect of various O_2 levels on cell viability. We cultured PRHs in 1%, 5%, or 8% O_2 in a hypoxia chamber. PRHs in 5% and 8% O_2 remained viable throughout the culture period. RT-PCR analysis was performed for the cells in 5% O_2 and showed that these PRHs maintained albumin and transferrin expression (data not shown). To control O_2 levels in the microchannels, we have constructed an oxygenator through which the medium will pass before reaching cells in the microchannel; this device will ensure that the proper amount of O_2 reaches cells. Initially, the oxygenator was intended to provide a gas mixture of 21% O_2, 5% CO_2, and 74% nitrogen at a total pressure of 1 atmosphere. For these conditions, a numerical simulation was run to test the final concentration of O_2 in the media flowing through the oxygenator and the time it takes to reach that final concentration. The geometry that was modeled was a 4-inch length of silicone tubing with an inner diameter of 1.5 mm and a wall thickness of 0.75 mm. The final concentration of O_2 was 0.0775 mol/m^3, slightly less than the desired value of about 0.084 mol/m^3. We concluded from these observations that the gas in the oxygenator will need to be pressurized to 1.08 atm to achieve the desired O_2 concentration and have adjusted the pressure accordingly.

Construction of a Continuous Perfusion System: We constructed a continuous perfusion system that includes a syringe pump, oxygenator, bubble trap, a reservoir for waste, and the microchannel (Figure 6). A syringe and silicone tubing that is filled with the culture medium is attached to a syringe pump that pumps the medium through the oxygenator and into the microchannel. An inlet and outlet for medium flow were made using syringe tips that were inserted through holes in the lid. Upon entering the oxygenator, medium travels through the silicone tubing, which allows the O_2 to diffuse through to the medium; a bubble trap receives the O_2-rich medium from the oxygenator and sends the medium to the microchannel. We have tested the perfusion system with RAMEC, HepG2, and PRHs. The syringe pump was started at a flow

rate of 0.1 µL/min and the oxygenator was pressurized to 20 psi. We initially observed that the cells survived for only about six hours under continuous perfusion. In order to increase the O_2 concentration in the microchannel and decrease the shear stress, we tried various perfusion conditions, flow rates, and configurations and have increased the survival period to at least 35 hours of continuous perfusion. We are currently perfecting this system for layered co-cultures to ensure longterm survival.

Fabrication of Dual Microchannel Platforms: We have built dual microchannels to generate higher configuration platforms that simulate liver sinusoids (Figure 7). The dual channel platform consists of two PDMS microchannels with a layer of parylene in between. Before these channels were fabricated, we demonstrated that PRHs and LSECs adhere to parylene and remain viable (data not shown). The first step in the microchannel fabrication process was soft lithography to create PDMS microchannels. These microchannels were then cut out individually, and pairs of these microchannels were "sandwiched" together with a 10-µm thick layer of microporous parylene in between. We have made a slightly altered design from the previously proposed one. The previous straight microchannel design did not allow us to "sandwich" the membrane in between because the membrane would not have been able to completely separate the two channels. Also, the inlet and outlet would overlap with those microchannels, and this is not desired because potential set-ups may require that the inlet and outlet of both channels be accessible from one side. The new design has a straight channel with the same dimensions as described in the original proposal and an extra channel length at both ends that extends out at an angle so that the holes do not overlap. The two channels were attached together by O_2 plasma bonding. PRHs survived in this system for at least 12 days.

Culture of primary human hepatocytes in microchannels: A longterm goal of this project is to replace PRHs with human hepatocytes to create a novel human mini-liver system. Primary human hepatocytes were acquired from the NIDDK-sponsored liver tissue procurements system and seeded into microchannels (Figure 8). Cells were isolated from the microchannels at various times post-seeding, RNA was isolated, and RT-PCR was performed to confirm expression of albumin, transferrin, connexin 43 and 32 (hepatocyte specific markers) and the absence of connexin 27 (markers of LSECs and Kuppfer cells, but absent from hepatocytes). Hepatocytes expressed specific markers and survived in the channels for at least 10 days.

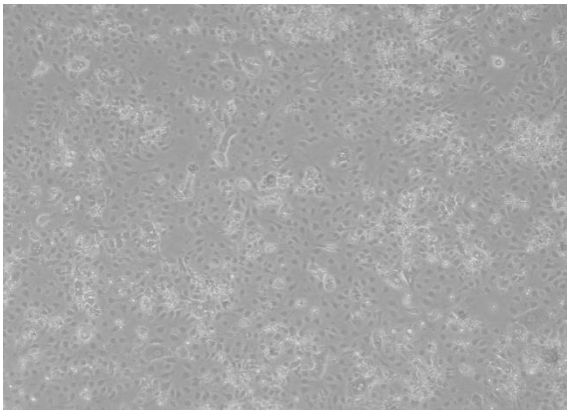

Figure 1: LSECs plated directly into microchannels. LSEC were isolated from perfused livers by differential centrifugation followed by Percoll gradient purification and direct infusion into microchannels.

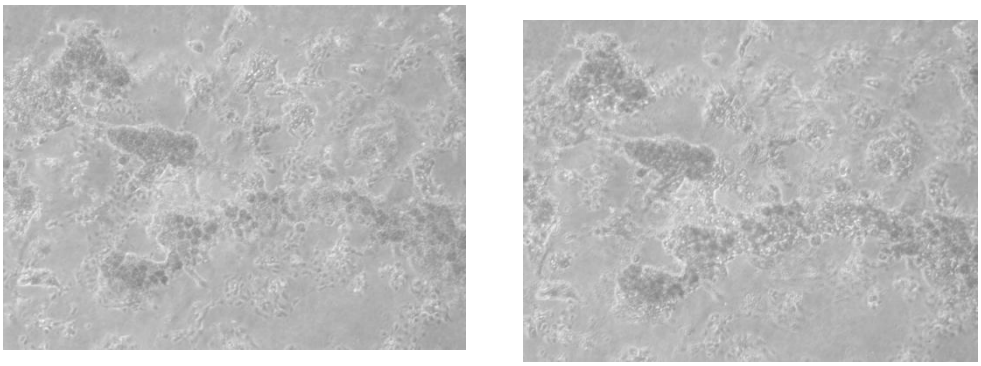

Figure 2. Layered co-culture of PRHs and LSECs. Right panel shows upper layer of hepatocytes, lower panel is refocused on lower layer of LSECs.

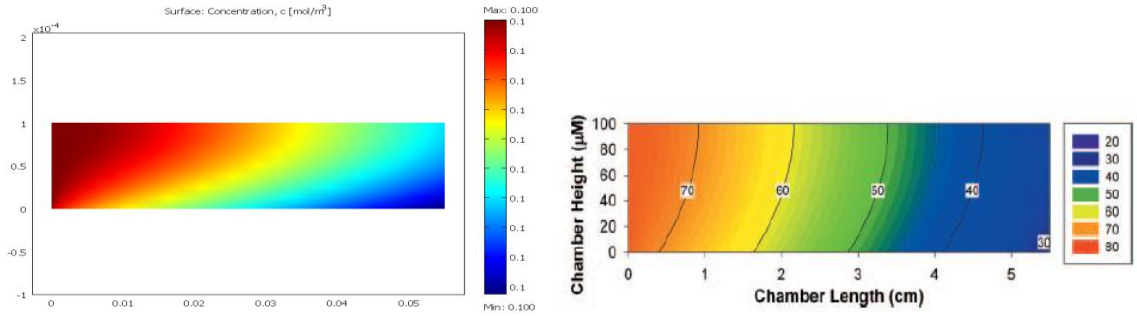

A. **B.**

Figure 3. Governing Equations and Boundary Conditions in Allen's Model (2005) for modeling oxygen concentration in a microchannel. (A) Our COMSOL simulation result. Simulation parameters: width 5.5e-2 m , height 1.0e-4 m, uniform velocity 0.01 m/s, cell uptake rate 6.46e-10 mol/s/m^2, and initial oxygen concentration 0.1 mol/m^3. (B) Allen (2005) simulation result. (REF: J.W. Allen, S.R. Khetani, and S.N. Bhatia, In Vitro Zonation and Toxicity in a Hepatocyte Bioreactor, Toxicological Sciences, 84,110-119 (2005)).

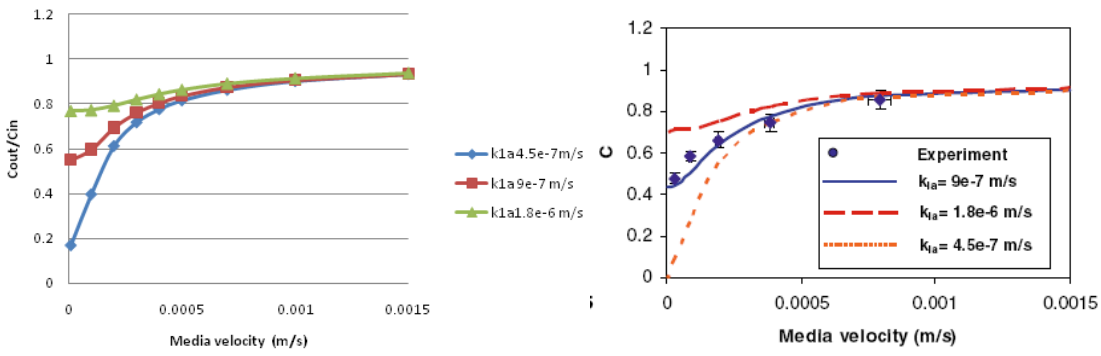

(A) (B)

Figure 4**.** Governing equations and boundary conditions in Metha's simulation (2007) used to calculate oxygen concentration at the outlet of the channel. Our simulation shows good agreement with Metha's simulation. (A) Our COMSOL simulation result. Simulation parameters: height 40 µm, length 0.01 m, diffusivity 2.1e-9 m^2/s, Vmax 2.06e-16 mol/cell/s, Km 0.005 mol/m^3. (B) Metha's simulation result (2007). (REF: G. Mehta, K. Mehta, D. Sud, J.W. Song, T. Bersano-Begey, N. Futai, Y.S. Heo, M. Mycek, J. J. Linderman, S. Takayama, Quantitative Measurement and Control of Oxygen Levels in Microfluidic Poly(dimethylsiloxane) Bioreactors During Cell Culture, Biomed Microdevice 9: 123-134 (2007).)

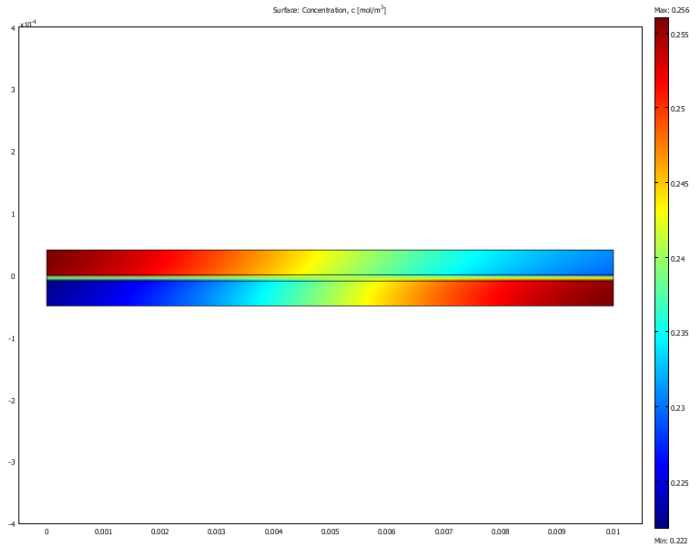

Figure 5**.** Oxygen concentration in a dual channel. Simulation parameters: height 40 µm, length 0.01 m, diffusivity of PDMS 2.1e-9 m^2/s, Vmax 2.06e-16 mol/cell/s, Km 0.005 mol/m^3, thickness of the membrane is 10 µm, and diffusivity of the membrane is 2.09e-13 m^2/s.

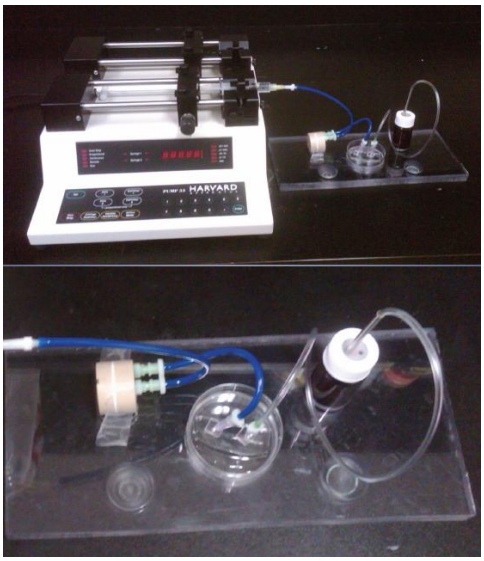

Figure 6: Continuous perfersion system. A syringe pump (upper panel) was attached to the microchannel system and various flow rates were tested to identify the flow rate that facilitated cell survival. See text for description of system and test of parameters.

Figure 7: Fabrication of dual microchannel. See text for description.

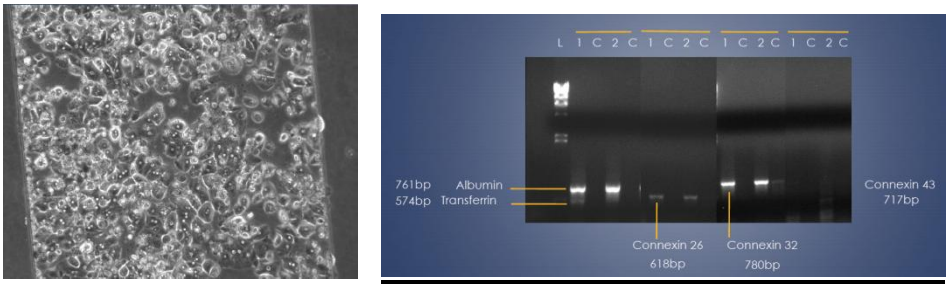

Figure 8: Primary human hepatocytes in microchannels. Right panel, cultured primary human hepatocytes in microchannels. Left panel, confirmation of expression of liver specific mRNAs by RT-PCR (see text for details).

Research Project 5: Project Title and Purpose

Identification of Biomarkers and Therapeutic Targets in 3D Hypoxic Breast Cancer Mode - Breast cancer is the most common female cancer in the Western world, affecting 1 of 8 women over their lifetime. One critical prognostic indicator for many tumor types including breast cancer is decreased oxygen levels or hypoxia. Hypoxic cancers are generally associated with aggressive growth, metastasis, and poor response to radiation treatment and chemotherapy. Understanding the molecular mechanisms and signaling pathways driving breast cancer development is critical for developing diagnostic and therapeutic agents. The purpose of this project is to use molecular techniques to analyze the role of hypoxia in regulating gene expression during breast cancer development and to utilize this information to identify novel diagnostic markers and therapeutic targets that can be used to detect and treat breast cancer.

Anticipated Duration of Project

1/1/2009 - 12/31/2010

Project Overview

The objectives of this project are to characterize the role of hypoxia and to identify the changes in gene expression that promote breast cancer development using a 3D breast cancer model system that we have developed. The overall objective of this grant is to validate and test whether the hypoxia-induced mRNAs that have been identified by microarray analysis are critical for hypoxia-mediated cell survival and the changes in tissue architecture that are observed in our 3D hypoxic model. We have focused on 5 hypoxia up-regulated genes that are likely to be involved with the pathways that lead to the DCIS (ductal carcinoma in situ) phenotype that is observed in 3D hypoxic cultures. We will also test whether targeting these genes reverses the hypoxic survival phenotype and prevents chemoresistance. Additionally, this work will determine whether these target genes can serve as biomarkers for hypoxic breast cancers.

The first aim of this project will use quantitative reverse transcriptase polymerase chain reaction (qRT-PCR) to verify the hypoxia induction of 5 key genes (LOX, ITGA5, MNK2, ET-2, and ANGPTL4) that we identified by microarray analysis. Additionally, immuno-blot analysis will be performed to ensure that changes in RNA levels of these key genes reflect changes in protein expression. The impact of the validated genes on cell survival and DCIS formation in 3D culture will be examined by knocking down the expression of the specific proteins using RNA interference and/or using specific inhibitors (when available).

The second aim of the project will determine if the 5 hypoxia induced genes described in aim 1 are also found in hypoxic DCIS breast cancer patients. We will perform immunohistochemistry (IHC) studies using commercially available tissue arrays to examine whether these 5 are also induced in hypoxic DCIS tumors.

The third aim of this project will determine if the hypoxia mediated changes in gene expression alters sensitivity to chemotherapeutic agents in normal and oncogenic (Her2) expressing breast cancer cells grown in 3D. This aim will be accomplished by treating normal and hypoxic 3D

cultures with the chemotherapeutic agent placitaxel and examining the impact of hypoxia on apoptosis. Additionally, we will examine the impact of the 5 hypoxia induced gene on placitaxel induced apoptosis by knocking out each gene with RNA interference and/or by using specific inhibitors. These studies will aid in identifying novel markers and therapeutic targets to kill hypoxic lesions before they progress to more advanced invasive phenotypes.

Principal Investigator

Gregg J. Johannes, PhD
Assistant Professor
Drexel University College of Medicine
245 N. 15th Street, MS-435
NCB5606
Philadelphia, PA 19102

Other Participating Researchers

Mauricio J. Reginato, PhD, Fernando Garcia, MD - employed by Drexel University College of Medicine

Expected Research Outcomes and Benefits

The anticipated outcome of this project is to validate our 3D breast cancer model and to determine the role of hypoxia in promoting breast cancer development and chemoresistance. We expect to identify new genes and pathways that are critical for the development of breast cancer and that correlate with breast cancer progression. These studies will aid in identifying novel markers and therapeutic targets to kill hypoxic lesions before they progress to more advanced invasive phenotypes. In addition, validating novel pathways or markers in hypoxic human tumors may help guide therapeutic treatment of hypoxic premalignant breast cancers. We will also potentially identify novel therapeutic targets that may reverse hypoxia-mediated chemoresistance. This project will also establish a novel model system to study the role of hypoxia in cancer progression.

Summary of Research Completed

We have continued to investigate the regulation of the 4 hypoxia regulated genes, Lysyl Oxidase (Lox), Map Kinase Interacting Serine/Threonine Kinase 2 (MNK2), Endothelin 2 (ET2), and Angiopoietin-like 4 (ANGPL4). Since we have previously shown that these mRNAs were upregulated by hypoxia in 3D, suspension, and adherent cell cultures, we have utilized the adherent cell culture system for the subsequent work. To further characterize the expression pattern of the target genes we analyzed the induction of each of the mRNAs after 6, 12, 24, and 48 hr of hypoxic exposure. As shown in Figure 1, all target genes were induced by 6 hr of hypoxic exposure but demonstrated different kinetics for maximal induction. The MNK2 (MNK) and ANGPL4 mRNAs were fully induced by 6 hr, the Lox mRNA required 24hr, and the ET2 mRNA required 48 hr of hypoxic exposure for maximum induction. The Adrenomedullin (ADM) mRNA was used as a positive control because it is a known HIF1 target and the Hypoxia

Inducible Factor 2α (HIF2α) mRNA was used as a negative control. As expected, the ADM mRNA was fully induced by 6 hr of hypoxic exposure and the HIF2α mRNA was unaffected by hypoxia.

We have also examined the expression of the HIF1α and HIF2α proteins in response to hypoxia. Figure 2 show that the HIF1α protein is maximally induced by 2 hr of hypoxic exposure after which it rapidly declines. The HIF2α protein is also induced by 2 hr of hypoxic treatment, but unlike HIF1α, HIF2α remains induced during prolonged hypoxic treatment. Thus, the HIF1α protein is transiently induced by acute hypoxia while the HIF2α protein remains induced during prolonged hypoxia. Actin was used as a loading control and showed no change in expression during hypoxic treatment. The loss of HIF1α by prolonged hypoxic exposure is not typical but has been reported to occur in other cell types. The molecular mechanism responsible for the loss of the HIF1α protein during prolonged hypoxia is the subject of a grant that has been submitted to the NIH entitled "Regulation of the HIF1α mRNA during prolonged hypoxia" (PI: G. Johannes).

Based on the differential expression of the HIF1α and HIF2α proteins, we hypothesized that the target mRNAs that are maximally induced by 24hr of hypoxic exposure (MNK2, ANGPL4, and Lox mRNAs) would be HIF1 targets, while those targets that required prolonged hypoxic exposure for maximal induction, such as ET2, would be HIF2 targets. To test this hypothesis, RNA interference was used to knockdown the expression of the HIF1α or HIF2α mRNAs in MCF10A cells and the impact on target mRNA induction was evaluated by qRT-PCR. Figure 3A shows that the siRNA targeting HIF1α (siHIF1α) knocked down the expression of the HIF1α mRNA by 5-fold while only marginally affected HIF2α expression. Similarly, the siRNA targeting HIF2α (siHIF2) knocked down expression of the HIF2α mRNA by 3-fold without affecting the HIF1α mRNA. This demonstrates that the siRNAs targeting HIF1α and HIF2α are efficient and specific for the targeted mRNA. Using these siRNAs the impact of HIF1 and HIF2 on the hypoxic induction of the target mRNAs was determined. Figure 4 shows that the hypoxic induction of the ANGPL4 (Figure 4A) and ADM (Figure 4B) mRNAs was significantly reduced in the HIF1α (siHIF1) and HIF2α (siHIF2) knockdown cells. This indicates that the hypoxic induction of these two mRNAs can be mediated by either HIF1 or HIF2. This ability of HIF1 and HIF2 to activate the transcription of common genes demonstrates their redundant function. We are currently investigating the impact of the simultaneous knockdown of HIF1α and HIF2α on the expression of these two mRNAs. Figure 5 shows that the hypoxic induction of the Lox (Figure 5A) and MNK2 (Figure 5B) mRNAs is significantly reduced in the HIF1α knockdown cells but not in the HIF2α knockdown cells. This indicates that the hypoxic induction of these two mRNAs is preferentially regulated by HIF1. In contrast, Figure 6 shows that the hypoxic induction of the ET2 mRNA is significantly reduced in the HIF2α knockdown cells but not in HIF1α knockdown cells. Unexpectedly, the knockdown of HIF1α resulted in a 4-fold induction of the ET2 mRNA through an unknown mechanism. We are currently investigating if the induction of the ET2 in the HIF1α siRNA treated cells is dependent on HIF2 expression. This is the first report that demonstrates that ET2 is a HIF2 specific target. In addition this data supports the hypothesis that mRNAs that require prolonged hypoxic exposure for maximum induction are HIF2 targets.

These studies show for the first time that the HIF1α protein is transiently induced by acute

hypoxia, while HIF2α induction is maintained during prolonged hypoxic exposure in MCF10A cells. This indicates that the HIF1 transcription complex is dominant during acute hypoxia while the HIF2 transcription complex is dominant during prolonged (<24hr) hypoxia. Additionally, we have determined that the ET2 gene is a HIF2 specific target, the Lox and MNK2 genes are HIF1 specific targets, and the ADM and ANGPL4 genes are both HIF1 and HIF2 targets. Together this data supports the hypothesis that the gene expression patterns induced by HIF1 or HIF2 are overlapping but not identical, which may have important therapeutic implications. For example, the changes in gene expression that are mediated by HIF1 may be important for the cellular adaption to acute hypoxia while the specific genes induced by HIF2 may be important for the survival of chronically hypoxic tumor cells. Thus targeting HIF1 may not be effective in killing chronically hypoxic cells that are often found in solid tumors. However, targeting HIF2 alone or in combination with HIF1 may be effective in killing these chronically hypoxic cells and provide a more favorable clinical outcome than just targeting HIF1.

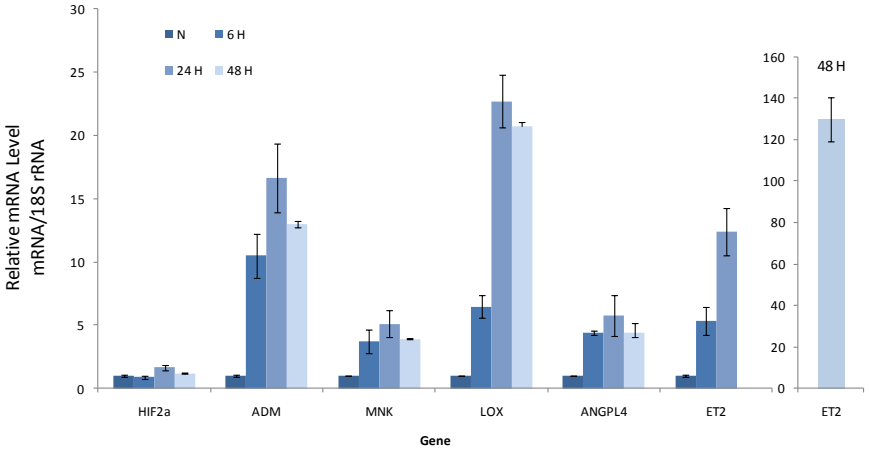

Figure 1. Induction kinetics of the hypoxia inducible genes. MCF10A cells were exposed to hypoxic conditions (1.0% O_2) for 0 (N), 6, 24, and 48 hr (H). Total RNA was harvested and the expression of the individual mRNAs (genes) was determined by qRT-PCR using gene specific primer/probe sets (ABI). The amount of the mRNA found under normoxic conditions was set to 1 for each mRNA. 18S rRNA was used for normalization. Standard error bars are shown. Abbreviations are denoted in text.

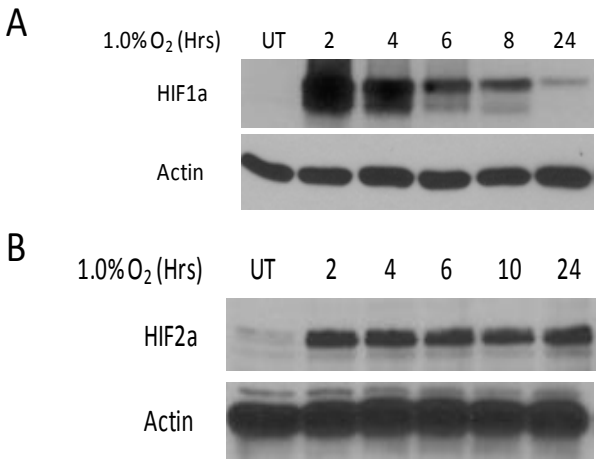

Figure 2. HIF1a induction is lost during prolonged hypoxia. Total protein was isolated from MCF10A cells that were grown under hypoxic (1.0% O_2) conditions for 0 (UT), 2, 4, 6, 8, and 24 hours (Hrs). Equal micrograms (30 ug) of protein were separated by SDS-PAGE and the amounts of HIF1a (A) and HIF2a (B) proteins were detected by immuno-blot analysis. Actin was used as a loading control.

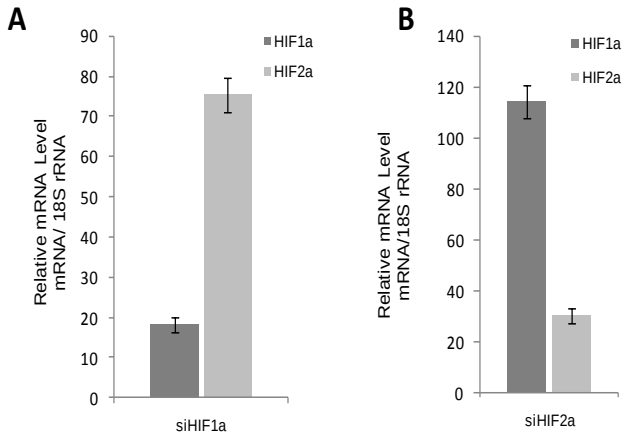

Figure 3. siRNAs directed against HIF1a or HIF2a efficiently knockdown the expression of the targeted mRNA. MCF10A cells were transfected with siRNAs targeting HIF1a (siHIF1a), HIF2a (siHIF2a), or scramble sequence (control). 48 hr after transfection, RNA was harvested and the amount of the HIF1a mRNA, HIF2a mRNA, and 18S rRNA was determined by qRT-PCR. The ratio of HIF1α mRNA /18S rRNA and HIF2α mRNA/18S rRNA found in cells transfected with the control siRNA was set to 100% (data not shown). The Relative mRNA level was determined by normalizing the amount of HIF1a (A) or HIF2a (B) mRNA in the knockdown cells to the level found in the cells transfected with the control siRNA. Standard deviation bars are shown.

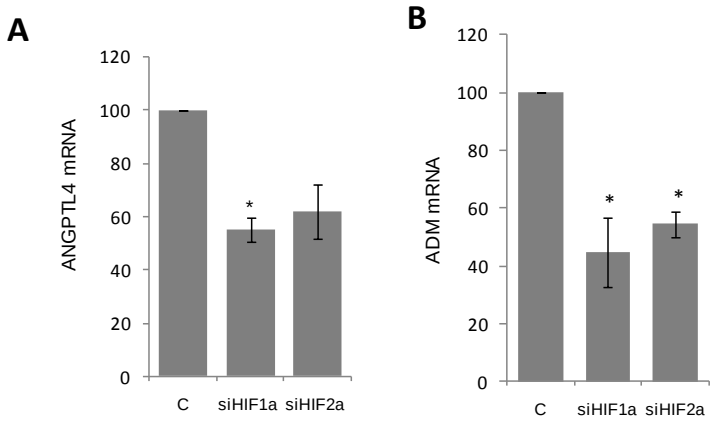

Figure 4. ANGPL4 and ADM are HIF1 and HIF2 targets. MCF10A cells were transfected with siRNAs targeting HIF1a (siHIF1a), HIF2a (siHIF2a), or a control siRNA (C) and placed under hypoxic conditions for 24 hr. The amount of the ANGL4 and ADM mRNAs was determined by qRT-PCR and normalized to the amount of the 18S rRNA. The normalized level of ANGPL4 (A) and ADM mRNA (B) in hypoxic cells transfected with the control siRNA was set to 100%. Standard Deviation bars are shown. * p-value <0.05

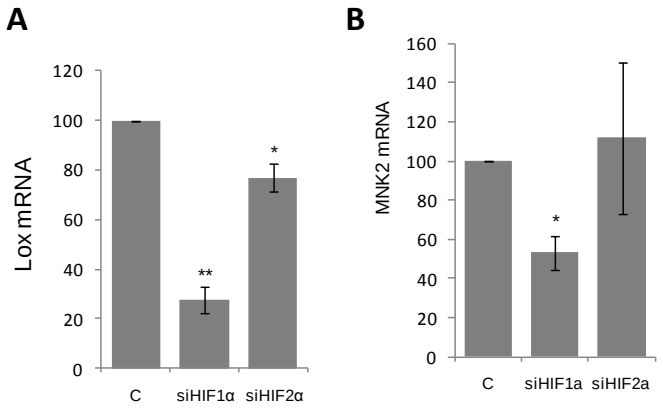

Figure 5. Lox and MNK2 are HIF1 targets. MCF10A cells were transfected with siRNAs targeting HIF1a (siHIF1a), HIF2a (siHIF2a), or a control siRNA (C) and placed under hypoxic conditions for 24 hr. The amount of the Lox and MNK2 mRNAs was determined by qRT-PCR and normalized to the amount of the 18S rRNA. The normalized levels of the Lox (A) and MNK2 mRNAs (B) in hypoxic cells transfected with the control siRNA were set to 100%. Standard deviation bars are shown. * p-value <0.05, ** p-value <.005

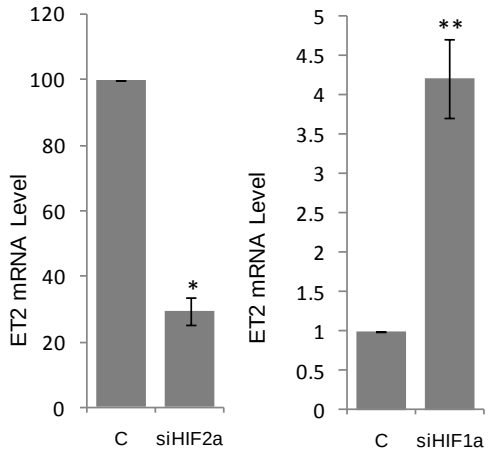

Figure 6. ET2 is a HIF2 target. MCF10A cells were transfected with siRNAs targeting HIF1a (siHIF1a), HIF2a (siHIF2a), or a control siRNA (C) and placed under hypoxic conditions for 24 hr. The amount of the ET2 mRNA was determined by qRT-PCR and normalized to the amount of the 18S rRNA. The normalized level of ET2 mRNA in hypoxic cells transfected with the control siRNA was set to 100% (A) or 1 (B). Standard deviation bars are shown. * p-value <0.05, ** p-value <.005

Research Project 6: Project Title and Purpose

Role of O-GlcNac Transferase as a Biomarker and Therapeutic Target for Prostate Cancer - In cancer a number of signaling pathways including phosphorylation/dephosphorylation cascades that add or remove phosphate residues are over-activated. Accumulating evidence suggests a less studied protein modification, known as O-GlcNAc (O-linked N-acetylglucosamine) may globally regulate cell growth and death. The role of O-GlcNAc modifications in prostate cancer phenotypes and signaling is not known. Moreover, we hypothesize that targeting enzymes which regulate O-GlcNAc modifications, such as O-GlcNAc transferase (OGT), may be a novel therapeutic treatment for prostate cancer. Using cell biological, chemical, and proteomic approaches, this project will test the novel hypothesis that O-GlcNAc modifications are increased in prostate cancer, they regulate cancer growth, and thus may serve as novel biomarker and therapeutic targets for prostate cancers.

Duration of Project

1/1/2009 - 6/30/2010

Project Overview

There is great interest in understanding the regulation of cellular signaling due to its importance in cancer biology. While much has been learned about phosphorylation-dependent signaling, the potential regulatory component of serine/threonine modification by O-GlcNAc has not been considered. Our preliminary data suggests higher levels of OGT in prostate cancer cell lines and prostate cancer tissue. Our project will expand this observation to specific types of human prostate tumors. This may provide a future basis for monitoring OGT or O-GlcNAc levels as potential novel clinical marker of prostate tumors.

In addition, demonstration that critical cancer transcription factors, such as FoxM1, are modified by O-GlcNAc will create a field of study concerning novel O-GlcNAc targets for therapeutic intervention in prostate cancer. Current therapies that target FoxM1 are of high interest and have shown promise using *in vivo* tumor models. The cytosolic and nuclear enzymes which regulate addition (OGT) and removal (O-GlcNAcase) are ideally suited targets for pharmacological modulation of O-GlcNAc levels. Agents for inhibition of OGT described here are validated as highly specific and have been shown *in vivo* to modulate O-GlcNAc levels in mice without general toxicity.

O-GlcNAc appears to modulate phosphorylation based signaling. Pharmacological targeting of kinases has had some success in the treatment of cancers, but is accompanied by unwanted side effects due to global inhibition of kinases in both normal and transformed cells. As a modulator of phosphorylation based signaling, O-GlcNAc may be ideally suited as a target to differentially dampen oncogenic signaling while avoiding toxicity in normal cells. Application of recently developed inhibitors of OGT to the novel question of O-GlcNAc's regulation of cancer based signaling will establish a basis for connecting pharmacological targeting of these enzymes with treatment of prostate cancer. The use of these inhibitors in the context of cancer signaling will likely inspire further refinement and testing of related pharmacological agents for the modulation

of O-GlcNAc in prostate cancer. This project will yield important information on the contribution of O-GlcNAc to altered cell cycle regulation, but will also intellectually provide a basis for researchers/clinicians to entertain and examine this novel regulatory mechanism (O-GlcNAc) as it relates to therapeutic treatment of prostate cancer.

Principal Investigator

Mauricio J. Reginato, PhD
Assistant Professor
Drexel University College of Medicine
Department of Biochemistry & Molecular Biology
245 N. 15th St., MS-497
Philadelphia, PA 19102-1192

Other Participating Researchers

Fernando Garcia, MD, Keith Vosseller, PhD - employed by Drexel University College of Medicine

Expected Research Outcomes and Benefits

We expect this work to introduce the novel concept of targeting O-GlcNAc modifications as therapy in prostate cancer specifically. As yet, such ideas have not been introduced. The expected results from this project will be to establish O-GlcNAc as a regulator of prostate cancer cell growth and a novel target for treating highly aggressive prostate cancers. In collaboration with a clinical pathologist, we will also examine whether OGT and O-GlcNac modifications occur in human prostate cancers *in vivo*, determine the frequency of overexpression, at which stage of prostate cancer it occurs, and determine whether OGT may be a novel biomarker for prostate cancer. We will test directly whether reducing O-GlcNAc modifications alter prostate cancer phenotypes including growth and survival. Cutting edge proteomics technology used for identification of specific targets regulated by O-GlcNAc will also provide a basis for other researchers in the field of prostate cancer signaling to discover O-GlcNAc modifications in their systems.

In addition, this proposal has the potential to help patients with aggressive prostate cancers. This project uses novel synthetic compounds to test our hypothesis that blocking O-GlcNAc modifications can inhibit prostate cancer phenotypes *in vitro*. If successful, these compounds can be used in future animal studies and clinical studies to expand our results *in vivo*. These compounds can also be used as templates for future compounds to increase specificity, availability and anti-tumor function. Thus, if these compounds do have anti-tumor function, then getting them to clinical trials for treating prostate cancers could be achieved in a relatively short period of time. The potential benefit for patients is high; however, little is known about possible toxicity of these compounds.

Summary of Research Completed

Aim 1. Analyze whether increase of OGT expression and O-GlcNAc modifications occurs at a significant frequency in human prostate cancers in vivo and to determine at what stage of tumorigenesis it occurs.

Previous work completed had shown that OGT was found to be elevated at the protein level in prostate cancer cells compared to normal immortalized prostate epithelial cells. This was consistent with Oncomine data showing four different studies found OGT was elevated at level of RNA in human prostate cancer samples compared to normal prostate tissue. We tested whether increased in OGT expression was also at the level of RNA in prostate cancer cells. We show that OGT is elevated two-fold at RNA level in prostate cancer cell line PC3-ML compared to non-tumorigenic prostate cell line RWPE-1 (Figure 1).

We have completed making 2 prostate cancer tissue arrays. We are currently getting ready to make slides and begin staining them with antibodies against OGT and O-GlcNAc. However, the antibodies we have tested for both OGT and O-GlcNAc have given us false positivc staining in control experiments. As controls we performed immunohistochemical analysis of PC3-ML cells containing OGT RNAi and although we detected significant decrease in Ki-67 staining, as well as decrease in OGT in western analysis in parallel cells, we did not detect decrease in OGT or O-GlcNAc staining in IHC suggesting these two antibodies are not specific. We are currently testing new antibodies for OGT and O-GlcNAc from different sources. Once we are convinced of specificity with new antibodies we will perform IHC in prostate cancer arrays we created.

Aim 2. Characterize role of OGT in prostate cancer cell proliferation.

We have shown in the last progress report that reducing levels in OGT with RNAi blocked prostate cancer growth. We now show through cell cycle analysis by propidium iodide staining and flow cytometry an increase in cells in G1-G0 phase of cell cycle targeted with OGT RNAi compared to control (Figure 2B). Consistent with cells arresting in G1and not progressing thru cell cycle, we also detected a three-fold inhibition of Ki-67 staining in prostate cancer cells with reduced OGT (Figure 2C). This is consistent with induction of CDK inhibitor p27 and loss of FoxM1 levels in cells with reduced O-GlcNAcation (Figure 2A).

Since in breast cancer cells FoxM1 is known to regulate cell invasion, we examined whether targeting OGT in prostate cancer cells lead to inhibition of cell invasion. PC3-ML cells when placed in three-dimensional basement membrane culture exhibits a morphological phenotype that is consistent with invasive potential (Fig. 3A). However, PC3-ML cells that express OGT shRNA, when cultured in three-dimensional conditions, contained reduced invasive protrusions compared to PC3-ML cells expressing control shRNA (Fig. 3A). This reduction in invasive morphology upon decreased OGT expression led us to assay the invasive potential of PC3-ML cells in transwell invasion chambers. As shown in Figure 3B, there is an approximate 60% reduction in the ability of PC3-ML cells to invade through the Matrigel coating of the transwell membrane with decreased OGT expression. Since it has previously been established that matrix metalloproteinase-2 and -9 (MMP-2 and -9) are associated with prostate cancer progression and metastasis, we examined expression of MMP-2 and-9 in the context of OGT knock-down. We

observed an approximate 70% reduction in MMP-2 and approximate 50% reduction in MMP-9 mRNA levels by QPCR (Fig. 3C) in PC3-ML cells with reduced OGT expression compared to control. Additionally, MMP-2 and MMP-9 protein levels were decreased upon knocking-down OGT (Fig. 3D). It has been previously shown that FoxM1 regulates expression of MMP-2 and -9 in breast cancer cells. Indeed, knocking-down FoxM1 in PC3-ML cells with stably expressed shRNA constructs results in a reduction of MMP-2 protein (data not shown), invasive structures in 3D culture (data not shown) and invasion (data not shown) in PC3-ML cells. Thus, targeting OGT in prostate cancer cells reduces invasion associated with expression of MMPs.

FoxM1 has been to shown to regulate VEGF expression in breast, pancreatic, and gastric cancers, suggesting that decreasing OGT may also inhibit VEGF expression and angiogenic potential of prostate cancer cells. We first determined if reducing levels of OGT in PC3-ML cells altered endothelial tube formation, an indirect measure of angiogenesis. After 24 hrs of stably expressing control or OGT shRNA in PC3-ML we collected conditioned media. This conditioned media was then used to stimulate human umbilical vein cells (HUVEC) in an endothelial tube formation assay; HUVECs were seeded onto a bed of Matrigel and then covered with PC3-ML cell conditioned media. After 6 hours, the HUVECs were imaged and tube length quantified using iVision software. As seen in Figure 4A, there is a statistically significant ($p < 0.05$, *t*-test) reduction in the ability of conditioned media from PC3-ML cells expressing OGT shRNA to stimulate tube formation in HUVECs as compared to media from control shRNA cells. RNA was harvested from the same PC3-ML cells used to condition media and levels of VEGF RNA were determined. As expected, levels of OGT RNA were decreased in those cells expressing OGT shRNA, moreover, VEGF RNA levels were also significantly ($p < 0.05$, *t*-test) decreased by 60-70% percent (Fig. 4B), consistent with the decreased ability of OGT knock-down cells to stimulate endothelial tube formation (Fig. 4B). Thus, we show for the first time that reducing O-GlcNAcation reduces VEGF levels and angiogenic potential of cancer cells.

Aim 3. Determine mechanism of how OGT regulates cell cycle regulator FoxM1.

We have previously shown that FoxM1 is not directly modified by O-GlcNac. New data suggest that OGT regulates FoxM1 protein stability and this regulation requires the N-terminal domain. The N-terminus of FoxM1 contains two degradation motifs. Exogenous wildtype FoxM1 is still degraded when we reduce levels of OGT (data not shown) however a mutant FoxM1 missing N-terminus is no longer degraded by reducing OGT levels (Figure 5A). To test whether FoxM1 regulation by OGT is required for alterations of PC3-ML angiogenic potential and VEGF expression we examined whether FoxM1 non-degradable mutant could reverse angiogenic potential of PC3-ML cells caused by downregulating OGT. PC3-ML cells overexpressing mutant FoxM1 (Figure 5A) was able to fully overcome the angiogenic inhibitory effect of OGT silencing (Figure 5B) as well as reverse inhibition of VEGF expression (Figure 5C). Thus, OGT regulation of FoxM1 is required for VEGF expression and angiogenic potential of prostate cancer cells. Future studies will examine mechanism by which OGT regulates FoxM1 degradation.

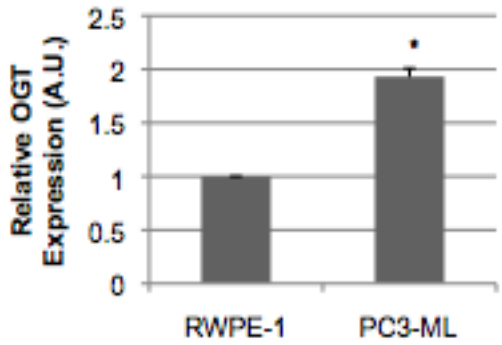

FIGURE 1. OGT levels are elevated in prostate cancer. A. Total RNA was collected from RWPE-1 and PC3-ML cells and subjected to QPCR for OGT expression; error bars indicate S.E.M. for n = 3, * indicated p > 0.05, *t*-test.

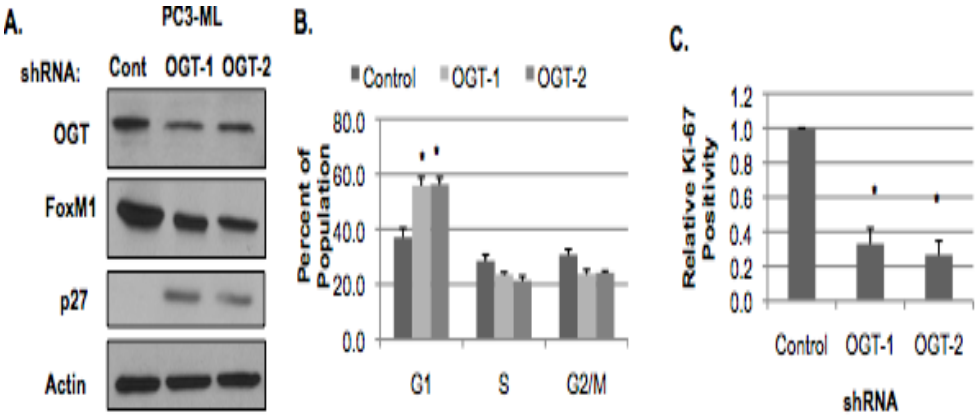

FIGURE 2. Targeting OGT alters cell cycle progression in PC3-ML cells. A. PC3-ML cells were infected with either control (scramble), OGT-1 or OGT-2 shRNA-containing lentivirus, lysed and immunoblotted with the indicated antibodies. **B.** PC3-ML cells were collected 48 Hours after infection and stained with propidium iodide for cell cycle analysis. Data aare presented as percent of gated population in indicated phase; error bars indicate S.E.M. for n = 3, * indicated p> 0.05. *t*-test. **C.** RWPE-1 and PC3-ML cells stably expressing control, OGT-1, or OGT-2 shRNA were incubated with FITC-conjugated antibodies against Ki-67 or isotype control and analyzed by flow cytometry for Ki-67 positivity. Data are presented as percent of gated population positive for Ki67; error bars indicate S.E.M. for n =3, * indicated p > 0.05, *t*-test.

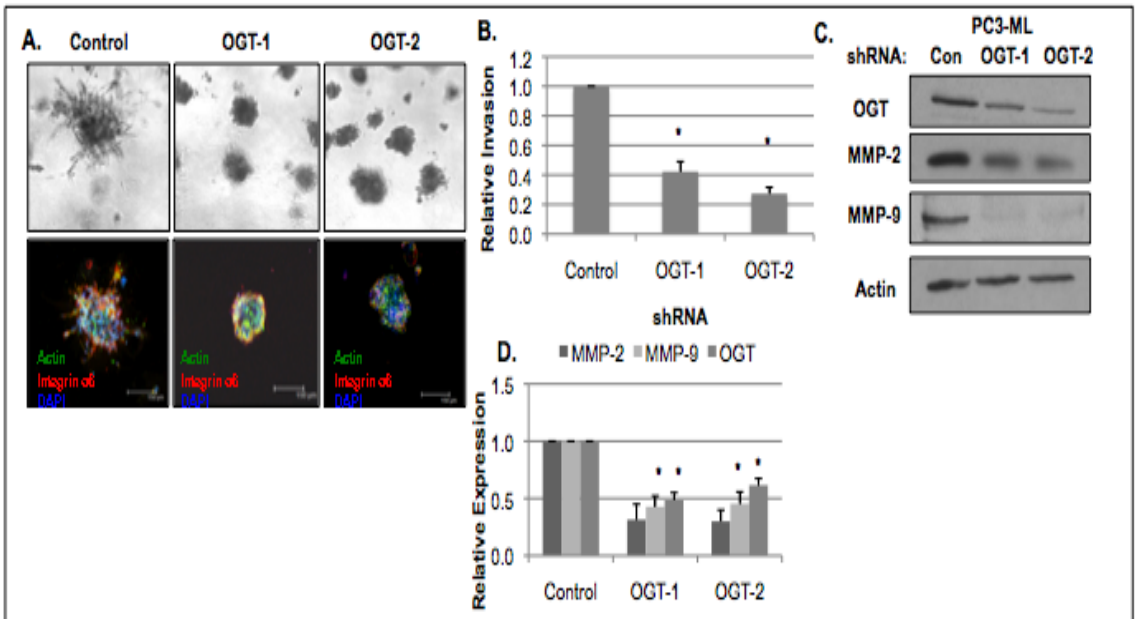

FIGURE 3. Targeting OGT decreases invasive phenotypes *in vitro*. A. Brightfield (top) and confocal (bottom) micrographs comparing control, OGT-1 or OGT-2 shRNA expressing PC3-ML cells cultured in three-dimensional culture. Green corresponds to actin, red corresponds to integrin α6 and blue corresponds to DAPI in confocal images. **B.** PC3-ML cells expressing control, OGT-1 or OGT-2 shRNA were assayed for ability to invade through Matrigel-coated transwell membranes. Data are presented as relative invasion compared to control shRNA; error bars indicate S.E.M. for n = 3, * indicated $p > 0.05$, *t*-test. **C.** PC3-ML cells described in figure 4B were lysed and immunoblotted for the indicated antibodies. **D.** Total RNA was collected from PC3-ML cells expression control, OGT-1 or OGT-2 shRNA and subjected to QPCR for MMP-2, MMP-9 and OGT. Data were normalized to cyclophilin A and are expressed as relative expression to control shRNA; error bars indicate S.E.M. for n = 3, * indicated $p > 0.05$, *t*-test.

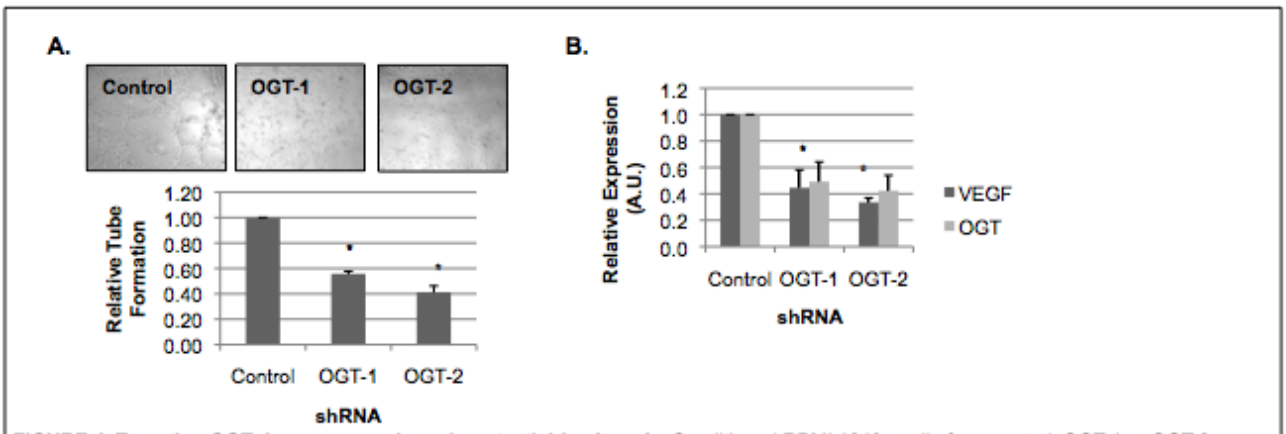

FIGURE 4. Targeting OGT decreases angiogenic potential *in vitro*. A. Conditioned RPMI 1640 media from control, OGT-1 or OGT-2 shRNA expressing PC3-ML cells was used to overlay HUVECs seeded on a bed of Matigel for 6 hours in endothelial cell tube formation assays. Relative tube length to control shRNA was calculated; error bars indicate S.E.M. for n = 3, * indicated p > 0.05, *t*-test. Representative images are depicted above. **B.** Total RNA was collected from PC3-ML cells expression control, OGT-1 or OGT-2 shRNA and subjected to QPCR for VEGF and OGT. Data were normalized to cyclophilin A and are expressed as relative expression to control shRNA; error bars indicate S.E.M. for n = 3, * indicated p > 0.05, *t*-test.

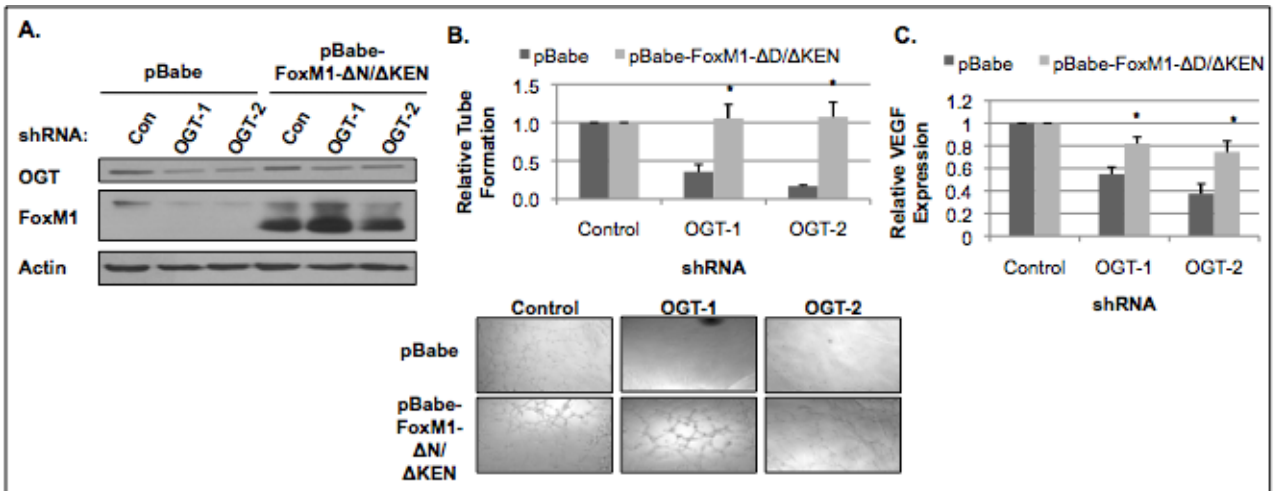

FIGURE 5. OGT regulation of angiogenesis and VEGF is mediated by Foxm1. B. Conditioned RPMI 1640 media from control, OGT-1 or OGT-2 shRNA expressing PC3-ML cells stable expressing control (pBabe) or FoxM1 N-terminal mutant was used to overlay HUVECs seeded on a bed of Matigel for 6 hours in endothelial cell tube formation assays. Relative tube length to control shRNA was calculated; error bars indicate S.E.M. for n = 3, * indicated p > 0.05, *t*-test. Representative images are depicted below. **B.** Total RNA was collected from PC3-ML cells expressing control or FoxM1 N-terminal mutant infected with lentivirus containig control, OGT-1 or OGT-2 shRNA and subjected to QPCR for VEGF and OGT. Data were normalized to cyclophilin A and are expressed as relative expression to control shRNA; error bars indicate S.E.M. for n = 3, * indicated p > 0.05, *t*-test.

Research Project 7: Project Title and Purpose

Piezoelectric Microcantilever Sensors (PEMS) to Detect Methicillin-Resistant Staphylococcus aureus (MRSA) - The purpose of the project is to develop a real-time, highly-sensitive, highly-specific, portable, cost-effective sensor that can be used to detect MRSA in patient samples in the field (doctors' offices, hospitals, university and college infirmaries, and others), leading to an improved treatment outcome measured by decreased mortality and morbidity.

Anticipated Duration of Project

1/1/2009 - 12/31/2010

Project Overview

About 19,000 patients died in US hospitals in 2005 of rapidly progressing MRSA infections, and almost 100,000 developed serious infections … leading to more deaths than to AIDS, tuberculosis and viral hepatitis combined. Blacks, the elderly and males are at highest risk. These tragic consequences of MRSA disease have continued to increase nationally. It is imperative that a rapid, sensitive MRSA detection assay be developed. The translational aspect and long term goal (~3 years) of the project is to develop a real-time, highly-sensitive, highly-specific, portable, cost-effective detection system that can be used for MRSA diagnosis of patient samples in the field, leading to improved treatment outcomes measured by mortality and morbidity. The short term goal is to develop an antibody-based, bench-top piezoelectric microcantilever sensor (PEMS) to detect MRSA. As part of an effort to fulfill this goal, the project has *2 specific aims*: (1) To acquire appropriate antibody (Immunoglobulin G, abbreviated IgG) specific for whole MRSA, MRSA surface components, and MRSA virulence factors, and (2) To attach the anti-MRSA IgG to the PEMS surface in order to optimize specific detection of well characterized MRSA strains, with high specificity and high sensitivity. Aim 2 will be done by modifying and fine tuning an existing lead magnesium niobate - lead titanate (PMN-PT) PEMS.

In addition to commercially available anti-MRSA antibodies, we will use 3 MRSA strains to raise antibodies, and determine which antibodies have the highest specificity and avidity for MRSA binding. IgG will be tested in Enzyme Linked Immunosorbent Assays (ELISAs) against the immunizing MRSA strains, a panel of MRSA strains, and other relevant bacterial pathogens. Antisera will be raised in rabbits against whole UV-killed MRSA. Anti-MRSA IgG will be immobilized on the organic MPS insulation layer of PMN-PT PEMS via the bi-functional linker Sulfo-SMCC. In addition, MRSA will be targeted by multiple (array) PEMS to improve the sensitivity at very low MRSA concentrations. Different PEMS within the array will be bound with different antibodies, each specific to a particular MRSA target. To determine specificity, anti-MRSA IgG-coated PEMS will be challenged with the immunizing MRSA strain, a panel of additional MRSA clinical isolates, bacterial normal skin flora and other Gram positive and Gram negative bacteria causing skin and soft tissue infections (SSTI).

Principal Investigator

Richard F. Rest, PhD
Professor
Drexel University College of Medicine
Dept of Microbiology and Immunology
2900 W. Queen Lane
Philadelphia, PA 19129

Other Participating Researchers

Wan Shih, PhD - employed by Drexel University

Expected Research Outcomes and Benefits

(i) Successfully acquire antibodies that are specific to MRSA and that bind MRSA but not other bacteria that cause skin or soft tissue infections (SSTI) similar to MRSA. Successfully bind functional anti-MRSA antibodies to the sensor (PEMS) surface and demonstrate that the antibody-coated sensor (MRSA PEMS) recognizes MRSA but not other bacteria that cause SSTI.

(ii) If the above outcomes are accomplished, then we are well on our way to developing a commercial product that can rapidly detect MRSA. Our hypothesis is that more rapid detection of MRSA infection will lead to more rapid antibacterial treatment and thus decreased morbidity and mortality.

Summary of Research Completed

Validation of Detection of Methicillin Resistant Staphylococcus aureus (MRSA)

Piezoelectric Microcantilever Sensors (PEMS) were fabricated and either rabbit polyclonal antibody to Methicillin Resistant *Staphylococcus aureus* (R-MRSA) antibody (1683 from Abcam Inc, Cambridge, MA) or a different *S. aureus* antibody was immobilized and covalently bound to the sensor to test for sensitivity and specificity to MRSA (1683) (Figure 1).

The PEMS was placed in a flow cell during detection. The total volume of the flow cell was 1.8 ml. A closed container with a 3 ml volume was used as a reservoir. PBS was circulated through the channel at a rate of about 0.7 ml/min and the frequency of the resonance peak around 680 KHz was monitored until it reached a stable baseline with a resonant frequency change of less than 200 Hz over 30 min. Increasing concentrations of MRSA were put into the flow system in sequence, which takes 30 mins for each concentration. The sequence of MRSA concentrations went from low to high:$1x10^3$/ml; $4x10^3$/ml; $7x10^3$/ml and $1x10^4$/ml. A validation step was also performed on a glass slide using gold-coated glass slides with an MPS layer using the same immobilizing method.

Experimental Results
The resonance spectrum of the PEMS is shown in Figure 2 in air and in liquid. The main peaks in air and in PBS overlapped indicating a good insulation in PBS. For the $1x10^3$/ml MRSA (1683) sample, the PEMS shows a frequency shift of 300 Hz (Figure3). For continuous concentration increments, the frequency shift from detection signals are: 600 HZ for $4x10^3$/ml; 700Hz for $7x10^3$/ml; 700Hz for $1x10^4$/ml. The detection time is 10 to 20 minutes for each concentration.

Anti - *S. aureus* antibody (against a non-MRSA strain) was also tested to compare with the anti-MRSA-antibody using the same strain of MRSA (1683) with a concentration of $1x10^4$/ml. After

insulation, the PEMS spectra peaks almost overlapped indicating a good insulation (Figure 4). However, the PEMS immobilized with anti-*S. aureus* antibody did not show any response while the anti-MRSA antibody showed a 200 Hz clear response (Figure 5). This indicates that the anti-*S. aureus* antibody does not bind to MRSA(1683), while anti-MRSA antibody does and shows a reliable detection response.

Scanning Electron Microscopy (SEM) pictures were taken to verify the detection results. As shown in Figure 6, a dense binding layer of MRSA (1683) can be seen, indicating anti-MRSA antibody binds to MRSA (1683) effectively (Figure 6), consistent with the PEMS detection results.

Conclusions

We successfully fabricated piezoelectric microcantilever sensors (PEMS) using lead magnesium niobate-lead titanate (PMN-PT) freestanding films that we processed. After insulation and immobilization of anti-MRSA antibody, successful demonstration of MRSA detection was accomplished. On the other hand, PEMS immobilized with anti-SA antibody did not respond to MRSA indicating that PEMS is sensitive enough to differentiate the anti-MRSA and anti-SA antibodies. It is concluded that PEMS is a suitable technology for detection of MRSA in a direct manner.

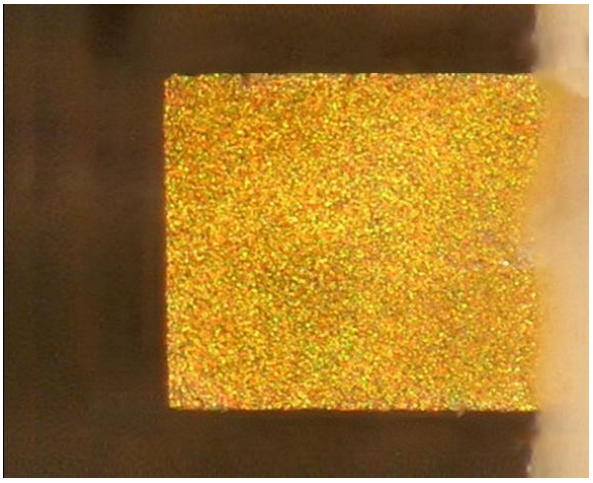

Figure 1**:** PEMS top view

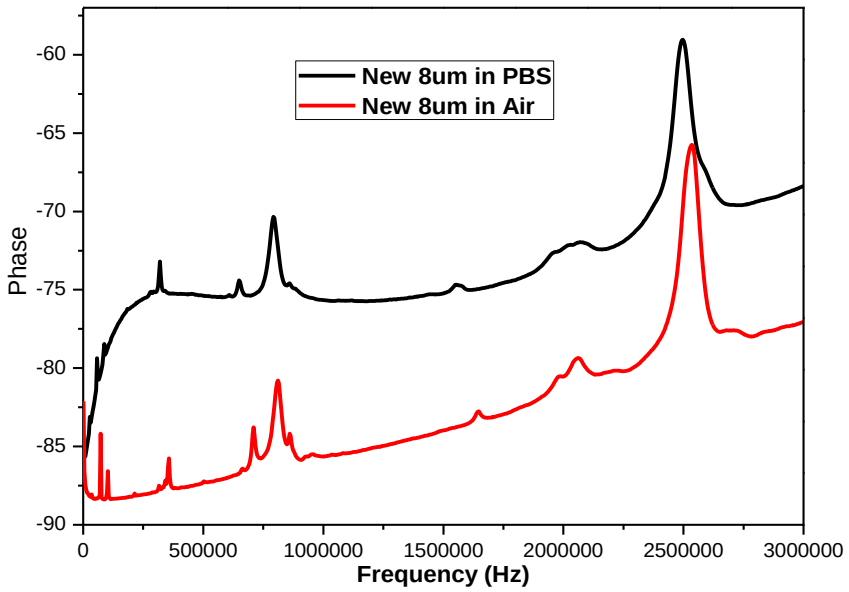

Figure 2: PEMS insulation results

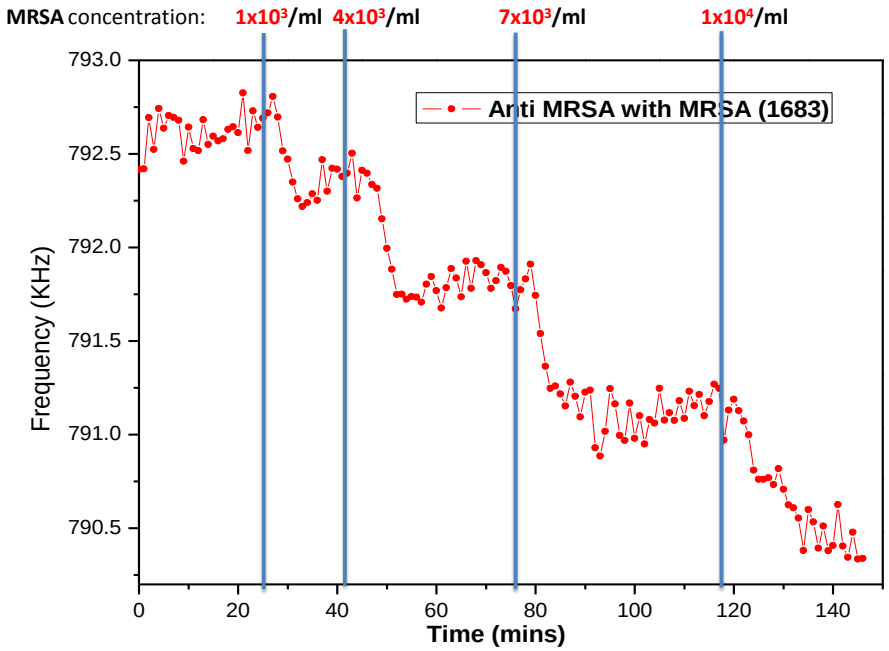

Figure 3: MRSA detection result using Anti-MRSA antibody

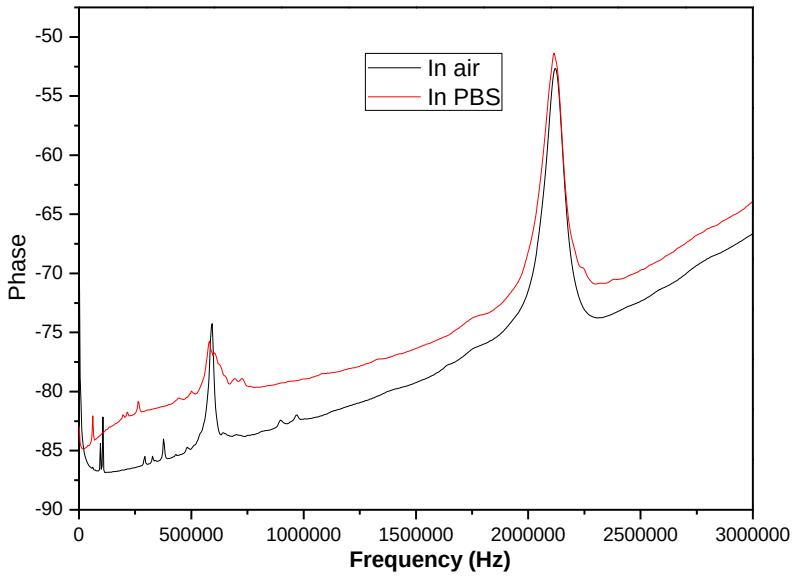

Figure 4: PEMS insulation results

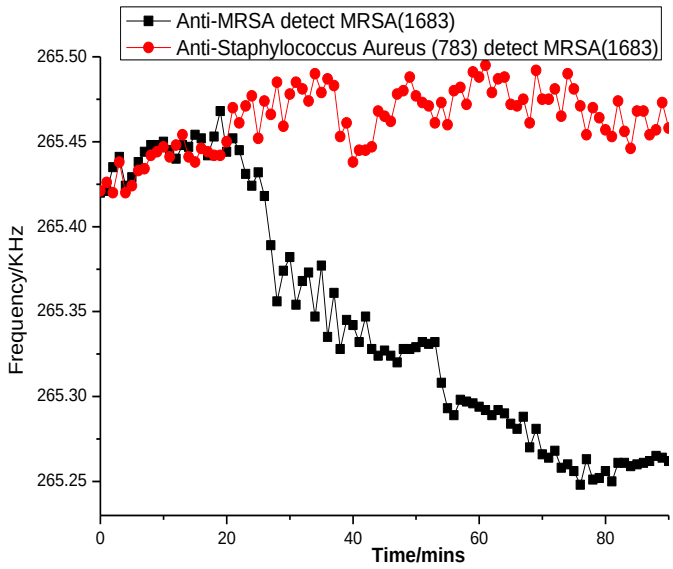

Figure 5: MRSA detection result using anti-MRSA and anti-SA antibody

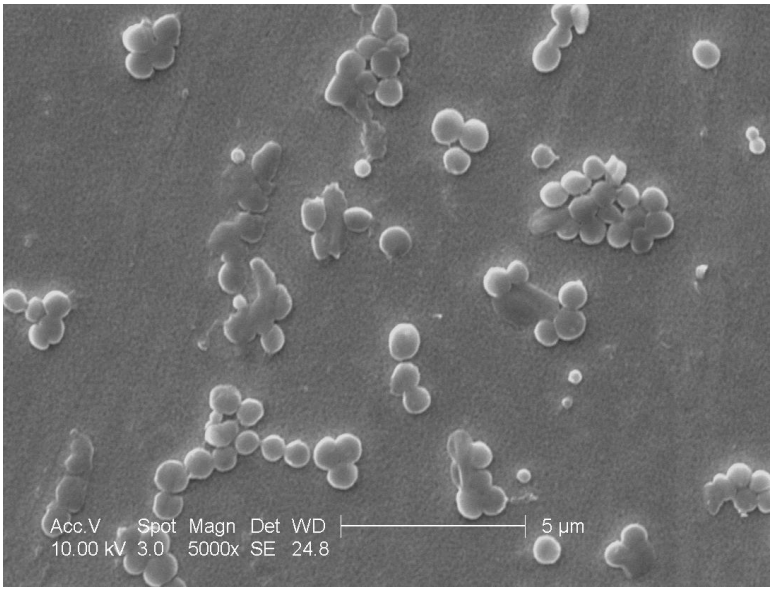

Figure 6: Section of an SEM micrograph of MRSA (1683) captured on glass slides with MPS using anti-MRSA antibody for immobilization

Research Project 8: Project Title and Purpose

RNA Interference-based Therapy for HIV-1 Associated Neurologic Disease - The purpose of this project is to lay the foundation for a new method to intervene in the progression of neurologic disease that often develops in HIV-1 infected individuals. We will investigate a method designed to reduce the ability of HIV-1 infected immune cells to migrate into the brain. This migration is enhanced by signals released from brain-resident infected cells in a positive feedback loop that we will disrupt using a strategy based on RNA interference. Certain receptors that are present on the surface of immune cells, and that allow these cells to respond to the migratory signals, will be down-regulated specifically in HIV-1 infected cells. If successful, this will lead to therapies designed to reduce the overall inflammatory immune response to infection in the brain and help to curb the progression of neurologic disorders.

Duration of Project

1/1/2009 - 6/30/2010

Project Overview

HIV-1 associated dementia (HAD) and a more subtle condition called minor cognitive motor disorder (MCMD) are neurological disorders that develop in a high percentage of HIV-1 patients and correlate with a worse overall outcome. Although control of viral load using anti-retroviral therapies (ART) has reduced the severity of these neurological diseases, longer patient survival times have increased their prevalence. Further, the failure of existing ART to cross the blood brain barrier (BBB) limits its efficacy in treating HIV-1 infection in the brain. In the experiments of this project, we will address these issues by designing a lentiviral vector that can

be transduced into monocytes and that will express silencing RNAs to suppress the expression of a cytokine receptor (CCR2). This receptor plays a central role in the migration of monocytic cells across the BBB in response to MCP-1 (CCL2), a cytokine that is induced by exposure of astrocytes to the viral protein Tat. We will express the CCR2-miRNA from a vector using a Tat-inducible RNA polymerase II promoter and thus limit silencing to HIV-1 infected cells, protecting the functional integrity of uninfected monocytes. We expect that this will help to interrupt a positive feedback loop where infected monocytes would otherwise be attracted into the brain by MCP-1 that, in turn, was induced by Tat released from brain-resident infected cells. We recognize that additional toxic factors are released in the brain of an infected patient and contribute to neuronal damage. This project is meant to be a proof-of-principle study that focuses on a major regulatory circuit, but where additional elements can be added to our highly adaptable silencing vectors in the future.

Principal Investigator

Laura F. Steel, PhD
Assistant Professor
Drexel University College of Medicine
245 N. 15th Street, Room 18313
MS 1013A
Philadelphia, PA 19102

Other Participating Researchers

Michele A. Kutzler, PhD - employed by Drexel University College of Medicine

Expected Research Outcomes and Benefits

This work can provide the basis for a novel approach to HIV-1 therapy that addresses both viral replication and disruptions of cellular signaling that are responsible for much of the pathogenesis of this disease. While there has been a degree of success in the treatment of HIV-1 with current anti-retroviral therapies (ART), these treatments remain problematic in terms of cost, unwanted side effects, patient compliance, and long-term efficacy. In addition, the neurological disorders associated with HIV-1 infection have been particularly difficult to treat since most medications will not cross the blood-brain barrier. This project explores the idea that cellular signaling pathways that affect disease progression can be specifically disrupted in HIV-1 infected cells. By targeting cellular pathways instead of viral gene products, we expect to reduce the problem of escape by this highly mutable virus. However, our strategy also preserves the functionality of important cells of the immune system that are not infected by HIV-1. We expect that this research will help to identify cellular regulatory networks that play key roles in neurological disease progression as well as to develop new strategies to disrupt these networks in a therapeutically significant way.

Summary of Research Completed

The goal of this project is to answer the question "Can Tat-inducible expression of interfering

RNAs designed to silence the expression of the MCP-1 receptor (CCR2) in infected macrophages inhibit their migratory response to MCP-1?"

In the first phase of this project, we designed and tested the efficacy of microRNAs (miRNAs) that target mRNA encoding CCR2. We have now extended our characterization of the Tat-inducible, chimeric CK-TAR promoter for the expression of these miRNAs and we have constructed lentiviral vectors that carry expression cassettes for the inducible expression of miRNAs. In addition, we have established an assay for the migration of monocytes towards MCP-1.

Characterization of the CK-TAR promoter

The chimeric Tat-inducible promoter that we refer to as the CK-TAR promoter is an essential element in our strategy to express miRNAs that can target mRNAs that contribute to the pathology of viral infection. The CK-TAR promoter is composed of the chicken β-actin core promoter and the HIV-1 TAR element and was first reported by Han et al. (Nucleic Acids Research, 19,7225, 1991). The HIV-1 viral LTR is highly responsive to induction by Tat and has been used in the construction of anti-viral vectors. However, we expect that the CK-TAR promoter will provide an alternative promoter that is less susceptible to risks associated with vector mobilization and the generation of replication competent lentiviruses when used in the context of therapeutic vectors. We have characterized the CK-TAR promoter, comparing its performance to the viral LTR with regard to induction by Tat as well as its induction by additional cell stimuli that may be encountered by uninfected cells. In these experiments, we have used miRNAs that target the reporter EGFP mRNA (enhanced green fluorescent protein) and miRNAs that target the HIV-1 protein Gag. Both of these are well-characterized miRNAs with strong silencing activities.

Results shown in Figure 1 demonstrate that Tat can induce silencing of a reporter to similar levels when miGag expression is driven by the LTR or the CK-TAR promoter. These experiments used Jurkat cells, a T-cell line that is relevant to HIV-1 infection. Cells were co-transfected with plasmids expressing either wild type Tat or an inactive Tat mutant (K41A) together with a reporter construct where the target site for miGag has been inserted into the 3'-untranslated region (3'UTR) of a gene encoding Renilla luciferase (Rluc). Silencing is measured by a reduction in Rluc activity relative to firefly luciferase (Fluc) expressed independently from the same plasmid.

In further experiments, shown in Figure 2A, we demonstrated that the level of Tat produced by replicating virus is sufficient to induce strong silencing by miGag driven from the CK-TAR promoter. Silencing induced from the CK-TAR promoter is comparable to that from the LTR or from the constitutively active CMV (cytomegalovirus) promoter. Here, HEK-293T cells were co-transfected with the indicated silencing plasmids together with an infectious molecular clone encoding HIV-1, strain LAI. Production of infectious virus was monitored by β-galactosidase assay after infection of the reporter cell line, Magi P4R5, with equal amounts of culture supernatant from the transfected cells. Similar results were obtained in experiments in Jurkat cells where reductions in the production of infectious virus were measured by the P4R5 reporter assay (Figure 2B) or silencing of the gag gene was measured by p24 (HIV-1 Gag protein) ELISA

of lysates of the transfected cells (Figure 2C). In Figure 2D, we show that reductions in virus replication are not simply due to competition for essential transcription factors resulting from overexpression of the TAR element from the CK-TAR promoter since production of an irrelevant miRNA (miEGFP) from this promoter does not lead to significant reductions in the production of infectious virus.

It is our long term goal to use the CK-TAR promoter to drive the expression of silencing RNAs that target cellular RNAs (such as the CCR2 mRNA) that contribute to HIV-1 pathology. Since the silencing constructs will be delivered broadly to cells of the immune system, it is important that the silencing RNAs are only expressed in infected cells, so that healthy immune cells are not affected. We show in Figure 3 that there is minimal induction of the CK-TAR promoter by agents such as LPS (lipopolysacchride), PMA (phorbol 12-myristate 13-acetate), and TNFα (tumor necrosis factor α). In the experiments shown in Figure 3A, HEK-293T cells were co-transfected with plasmids expressing EGFP and a silencing plasmid expressing miEGFP from either the viral LTR or the CK-TAR promoter; cells were then treated with the indicated agents. Transfection with the Tat expression plasmid, pTat, is shown as a control for induction of silencing. It is evident that LPS can induce moderate levels of activity from both the viral LTR and the CK-TAR promoter, but little or no CK-TAR activity was induced by either PMA or TNFα. Similar results were observed in Jurkat cells (Figure 3B and C).

Lentiviral vectors with miRNA expression cassettes

We have used the pLEX-GFP vector (described in the Progress Report of July 2009) to construct a series of lentiviral vectors with the following promoter-miRNA expression cassettes: CMV-miFlu (control), CMV-miCCR2-DE, CK-TAR-miCCR2-DE, CMV-miGag, CK-TAR-miGag. These vectors are depicted in Figure 4. The miCCR2-DE vectors express a bi-cistronic miRNA (comprising miCCR2-D and miCCR2-E) that targets CCR2 mRNA that was developed in related work in a separate project. The miGag vectors express a potent miRNA that directly targets HIV-1 miRNAs; these vectors, together with the miFlu vector, will be used in control experiments. The constructs have been packaged using a VSV-G pseudovirus system and are now being tested for their ability to transduce immune cell populations, including monocytes and T-cells.

Establishment of a cell migration assay

To test the physiological relevance of the knock-down of CCR2 in miRNA-transfected cells, we will utilize chemotaxis assays as a functional measurement of CCR2 activity. In Figure 5, we show that we have established that U937 (monocytic) cells respond and chemotax towards MCP-1 protein. U937 cells were placed in the upper wells of 5mm Transwell plates (1 X 10(6)/well), while bottom wells contained medium alone or medium with recombinant human MCP-1 (5 or 15ng/ml). After incubation at 37°C for 2 hrs or 6 hrs, migrated cells in the lower chamber from multiple replicate wells (6 wells per each condition, three independent trials) were collected and counted. The data are graphed as Migration Index (MI) which represents the fold increase in the number of cells migrated in experimental wells divided by the number of cells migrated in background, medium control wells. Data generated from the independent experiments and replicate wells were averaged and results are shown in Figure 5. Using this chemotaxis system,

we will be able to test whether Tat-inducible expression of interfering RNAs designed to silence the expression of the MCP-1 receptor (CCR2) in infected macrophages inhibit their migratory response to MCP-1.

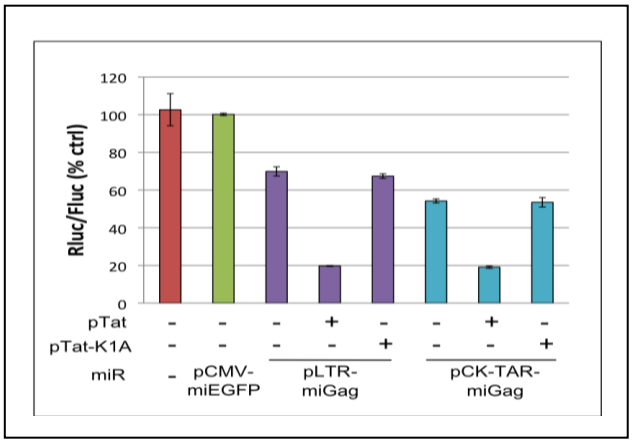

Figure 1. Tat induces silencing by miGag expressed in Jurkat T-cells from the viral LTR and from the chimeric CK-TAR promoter.

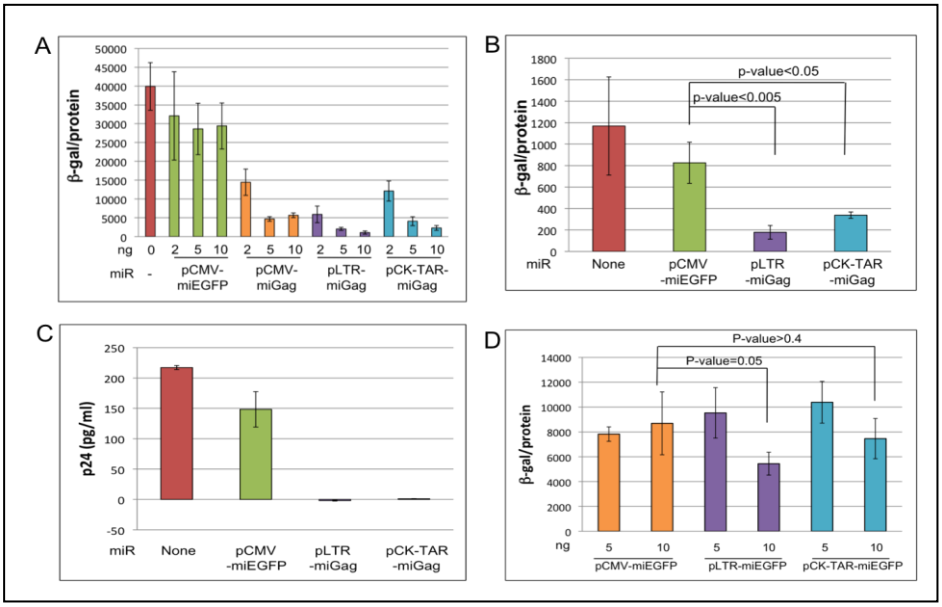

Figure 2. Tat produced from replicating virus is sufficient to induce silencing activity from miRNAs driven by the viral LTR or by the CK-TAR promoter.

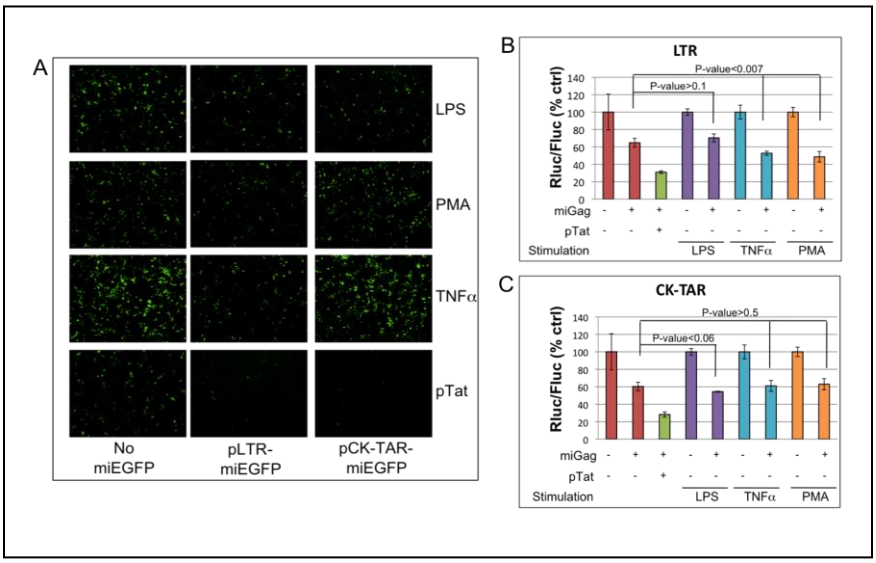

Figure 3. Response of the LTR and the CK-TAR promoter to stimulation of cells with LPS, PMA, and TNFα.

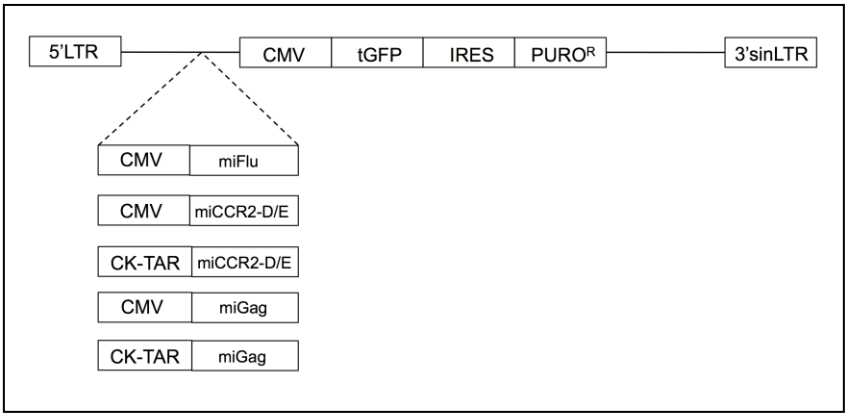

Figure 4. Expression cassettes for constitutive expression of the indicated miRNAs from the CMV promoter, or HIV-1 Tat-inducible expression from the CK-TAR promoter, have been inserted into the pLEX-GFP lentiviral vector.

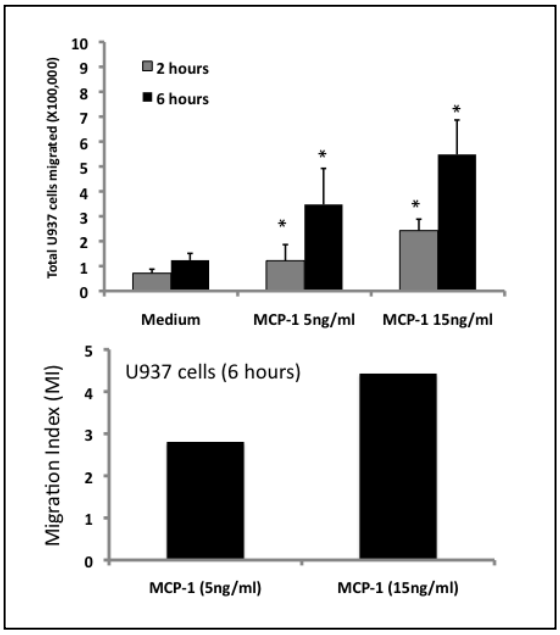

Figure 5. The migration of U937 cells towards MCP-1 in Transwell assays is both dose and time dependent.

Research Project 9: Project Title and Purpose

Somatostatin Signaling in Alzheimer's Disease - A common feature of Alzheimer's disease (AD) is a decrease in the neuropeptide somatostatin in brain. The degree of somatostatin reduction has been correlated with the degree of cognitive decline. However, the role of somatostatin in AD has not been defined. This project is designed to test the function of somatostatin in cognition and cellular models of learning and memory in a mouse model of AD. This project will validate whether somatostatin and its receptors could be utilized as novel therapeutic targets for treating this devastating disease, for which there are currently no effective drugs.

Duration of Project

1/1/2009 - 12/31/2009

Project Overview

Levels of the neuropeptide somatostatin (SST) are reduced in brain of Alzheimer's disease (AD) patients, and this decline is correlated with the degree of cognitive dysfunction. This project is designed to explore the role of SST in AD using a mouse model of the disease. Our focus is on the SST_3 receptor, which localized on neuronal cilia. Our preliminary data shows that SST_3 is required for object recognition memory, a type of memory that is dysfunctional in AD. That neuronal cilia may be important signaling organelles has been hypothesized but not demonstrated. Our results are the first to show a role for neuronal cilia in brain function—the role of cilia signaling in cognition has not been addressed outside our studies.

We have designed a plan to examine whether dysfunctions in cilia signaling are present in AD mice, and whether we can restore cognitive function and synaptic plasticity in these mice by activation of SST_3. We will use the 3X-TG AD mouse model that contains 3 transgenes associated with familial AD and have pathological and cognitive phenotypes associated with the human disease. We have 4 major experimental aims: 1) Examine whether a specific form of synaptic plasticity, forskolin evoked long-term potentiation (LTP), is dysfunctional in the AD mouse model. We have previously demonstrated that this cellular model of learning and memory requires activation of SST3. 2) Determine whether activation of SST3 can restore LTP deficits in AD mice. 3) Examine whether cognitive deficits in AD mice can be restored by intracerebroventricular injection of SST or its analogs. 4) Examine whether neuronal cilia are abnormal in the AD mouse. This research will provide important information on the role of somatostatin and SST_3 in AD, and provide rationale for exploring SST_3 as a therapeutic target for treating AD.

Principal Investigator

Melanie K. Tallent, PhD
Assistant Professor
Drexel University College of Medicine
Department of Pharmacology and Physiology
245 N. 15th Street, MS 488
Philadelphia, PA 19102

Other Participating Researchers

None

Expected Research Outcomes and Benefits

This project should provide new information on the underpinnings of Alzheimer's disease (AD), and suggest novel therapeutic approaches. Currently, there are no drugs that are effective in preventing or reversing cognitive declines associated with AD. Our research is designed to explore a new therapeutic target, the neuropeptide receptor SST_3. SST_3 has a unique localization pattern in the brain, and may have novel signaling mechanisms. Activation of SST_3 is required for recognition memory. This is the type of memory that allows us to distinguish between novel and familiar things, and is defective in AD. Thus drugs that target SST_3 may be effective in reversing cognitive decline caused by this devastating disease.

Summary of Research Completed

The major goal of our project was to examine whether activation of SST3 signaling pathways could be a therapeutic approach to treating Alzheimer's disease, using a mouse model of the disease (3x-tg mice). In our previous report we showed a specific type of synaptic plasticity, forskolin-evoked long-term potentiation (F-LTP) was impaired in 3x-tg mice, but other types of synaptic plasticity were intact. Since this is remarkably similar to our findings in SST3 knockout mice, we further explored the requirement of SST3 activation for F-LTP. This type of LTP is

generated by direct activation of adenylyl cyclase, an enzyme that when activated produces the important signaling molecule cyclic adenosine monophosphate (cAMP). Therefore we examined the role of SST3 in modulating cAMP levels in mouse hippocampus.

Signaling mechanisms of SST3 in hippocampus

We found that cAMP levels in *sst3* knockout mice were 41.5 ± 13% of wild type when extracted directly from hippocampus (n = 6 each; $p < 0.05$). We also examined forskolin-induced increases in cAMP in a homogenized hippocampal preparation (lysate) from wild type and *sst3* knockout mice. Unstimulated cAMP levels in lysates were also significantly lower in *sst3* knockout mice (820 ± 312 pmol/mg protein) compared to wild type (1299 ± 144 pmol/mg protein). However, forskolin induced a similar relative increase in cAMP in hippocampal lysates from wild type (5.1 ± 1.7 fold increase; n = 5) and *sst3* knockout mice (4.8 ± 0.4 fold increase; n = 5). We also examined the effect of the SST3 agonist and antagonist in hippocampal lysate (n = 5) and in hippocampal slices (n = 5; Fig. 1). In hippocampal lysate, blockade of SST3 with ACQ090 (1 µM) did not significantly affect forskolin-stimulated cAMP levels (91 ± 15% of control; $p = 0.6$). However, in hippocampal slices, ACQ090 reduced forskolin-stimulated cAMP levels to 48.6 ± 8% of control levels ($p = 0.03$). Similarly, SST3 activation with L-796,779 (1 µM) did not affect basal cAMP levels in hippocampal lysate (90 ± 11%; n = 0.4), but in hippocampal slices increased basal cAMP levels to 130 ± 7% of control levels ($p = 0.03$). These results suggest that intact cilia and/or neuronal structure may be required for SST3 signaling.

The next question we wished to address was how does activation of cAMP lead to signaling events in the neuronal soma. Our findings suggested that cAMP signaling within the tiny cilia must be amplified in order to produce such large changes in overall cellular cAMP levels. Interestingly, neuronal cilia in hippocampus and elsewhere specifically express adenylyl cyclase type 3 (AC3). This same AC isoform mediates olfactory transduction in olfactory cilia. Therefore we proposed a model of signaling based on analogies to olfactory signaling, in which increases in cAMP activate cyclic nucleotide gated (CNG) ion channels. We therefore tested whether blockers of CNG channels impaired F-LTP. We used two different blockers, dicholorobenzamil (DCB; 30 µM) and L-cis-diltiazem (DTZ; 30 µM). Interestingly, both blockers inhibited F-LTP to a similar degree as the SST3 antagonist ACQ090 (Fig. 2). This supports our hypothesis that signaling in hippocampal cilia shares common mechanisms with olfactory transduction.

Object recognition memory in 3x-tg mice

We have demonstrated that the major cognitive impairment in SST3 knockout mice is in object recognition memory (ORM). Mice have an innate preference for novel vs. familiar objects which can be utilized to test ORM. SST3 knockout mice show no discrimination between novel and familiar objects. Acute blockade of SST3 via IP injection of the systemically active SST3 antagonist ACQ090 leads to a similar impairment. Since ORM in the 3x-tg mice had not been examined, we determined whether these mice could discriminate novel objects. We found that 3x-tg mice as young as 5 mos (n = 12), with a 1 hr delay, showed no preference for a novel object (Fig. 3). Non-transgenic (non-tg) control mice as old as 11 mos showed significant preference for the novel object at the 1 hr retention interval (n = 10). Thus ORM represents an

early cognitive deficit in the 3x-tg mice, and demonstrates another similarity between this AD mouse model and SST3 knockout mice.

To further define the role of SST3 in ORM, we needed to determine its site of action. ORM involves both the hippocampus and perirhinal cortex (PRC). We examined whether SST3 blockade with ACQ090 could affect F-LTP in the PRC, as it does in CA1. Interestingly, although we were able to induce stable LTP with forskolin, it was not impaired by ACQ090 (1 µM). In control slices, 60 min following washout of forskolin cocktail, fEPSP slopes were 158 ± 9.9% of baseline (n = 8). When ACQ090 was superfused beginning 15 min prior to and during the 15 min forskolin application, fEPSP slopes were 155 ± 15% of baseline 60 min following washout of drugs. (n = 4). Thus although SST3 is expressed in PRC, it may have a function distinct from that in CA1 hippocampus.

We next wanted to examine whether SST3 blockade in hippocampus was sufficient to block ORM. We have established a protocol to inject drugs into hippocampus using bilateral cannulae in mice. The original stereotaxic coordinates we used resulted in hippocampal damage and nonspecific functional deficits in some wild type mice. After altering our coordinates, we were able to show no impairment of ORM after saline injection in mice 30 min prior to the test phase in our ORM paradigm (Fig. 4; n = 5). However, the SST3 antagonist ACQ090 (20 ng; n = 5) impairs ORM when injected into hippocampus 30 min prior to the ORM test (30 min after training; Fig. 4). Thus blockade of SST3 in hippocampus is sufficient to impair ORM in mice.

SST and cilia deficits in 3x-tg mice

In our previous progress report we showed that aged 3x-tg mice had reduced SST levels and SST3 expression, and that targeting of SST3 but not AC3 to neuronal cilia was impaired in aged (12-15 mos) 3x-tg mice, and, to a lesser extent, in aged non-tg mice. We now demonstrate that SST deficits appear as early as 6 mos in the 3x-tg mice. Shown in Fig. 5 is a Western blot with immunostaining for SST. SST expression in hippocampus is reduced in 3x tg mice compared to non-tg mice. This confirms our findings using immunohistochemistry in 12 mos old 3x-tg mice that we showed previously. We also wanted to determine at what age SST3 expression and targeting began to show changes in 3x-tg mice. We found that at 9 mos of age, SST3 expression appears normal in 3x-tg mice (Fig. 6). These results suggest that SST3 may be a valid therapeutic target for AD until late stages of the disease.

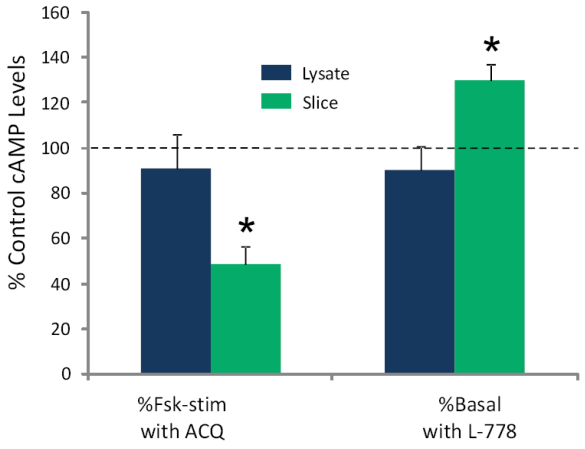

Figure 1. *Effects of SST3 agonist and antagonist in hippocampal lysate and slices*. Forskolin (Fsk) stimulation of cAMP is inhibited by 1 µM ACQ090 in hippocampal slices but not hippo-campal lysate (left columns). The SST3 agonist L-796,778 (L-778) increases basal cAMP levels in hippo-campal slices but not hippocampal lysate (right columns). * indicate significant difference from control cAMP levels (basal or forskolin-stimulated in the absence of SST3 ligand; dashed line).

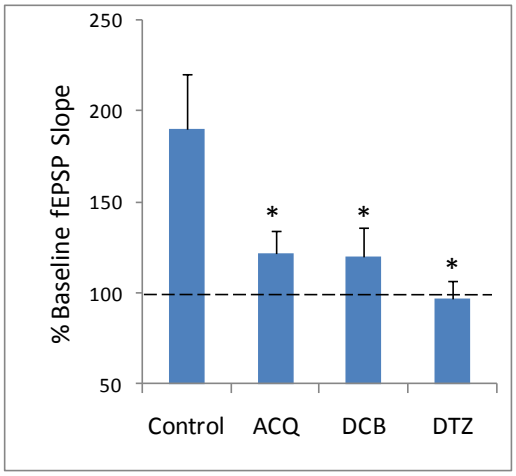

Figure 2. *Blockade of CNG channels impairs F-LTP in hippocampal slices*. Forskolin (Fsk) stimulation of cAMP is inhibited by SST3 antagonist 1 µM ACQ090, and to a similar degree by CNG channel blockers dichlorobenzamil (DCB) and L-cis-diltiazem (DTZ). * indicate significant difference from control F-LTP.

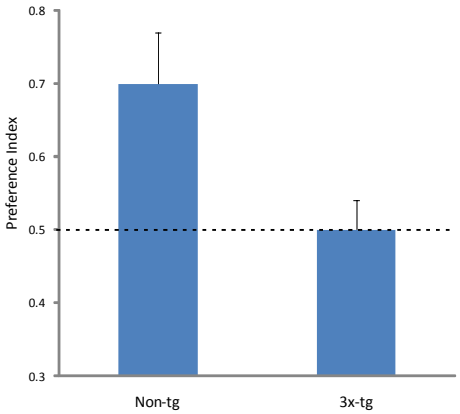

Figure 3: *ORM deficit in 3x-tg mice.* Preference index is number of approaches to the novel object over total number of approaches. Dotted line equals show no preference (0.5).

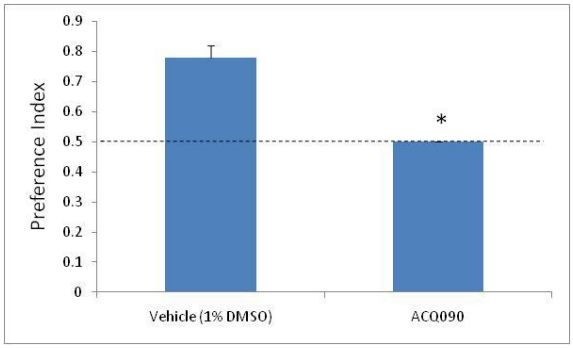

Figure 4. Bilateral intrahippocampal injection of ACQ090 impairs object recognition memory in wild type mice. Injections of vehicle or ACQ090 (20 ng bilaterally) were made 30 min prior to testing using a 1 hr retention interval. Dashed line indicates no preference; asterisk shows significant difference from vehicle injection ($p < 0.05$; paired t-test.)

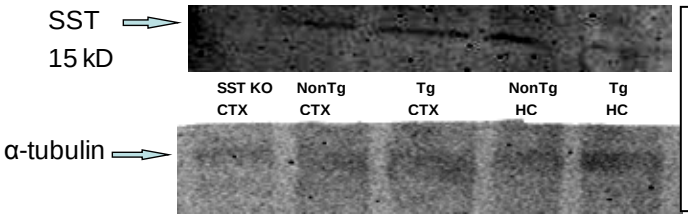

Figure 5. *Western blots with anti-SST antibody shows reduction of SST in hippocampus of 6 mos old 3x-Tg mice*. Antibody specificity is confirmed in SST knockout mouse (lane 1).

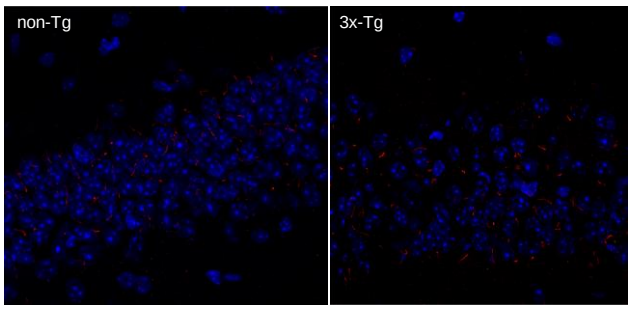

Figure 6. *Normal SST3 staining (red) in CA1 of 9 mos old 3x-Tg mice*. Left panel 9 mos old non-Tg mice; Right panel age-matched 3x Tg mice. Note similar staining pattern and ciliary targeting of SST3 in both mouse strains. Anti-SST3 antibody 7986 gift from S. Schulz, blue staining is DAPI (nuclear).

Research Project 10: Project Title and Purpose

Characterization and Application of a Novel Drosophila Model for CHARGE Syndrome - The long term goal of this project is a deeper understanding of the pathogenesis of CHARGE Syndrome, a rare autosomal dominant disorder that affects roughly 1 in 10,000 live births. We plan to examine these mechanisms by modeling the disorder in the fruit fly *Drosophila melanogaster*. By creating and validating a working model of CHARGE Syndrome in *Drosophila*, we will be able to genetically test the contribution of candidate genes towards the phenotypes associated with these flies, in order to predict whether these genes may be involved in the symptoms of CHARGE patients. We will also be able to analyze the effect(s) of mutation in these genes on neuronal morphology and connectivity within nerve cells in the fly brain. This

approach has been very successful in the past in understanding complex forms of mental retardation.

Duration of Project

1/1/2009 - 12/31/2009

Project Overview

CHARGE syndrome is a rare, autosomal dominant disorder characterized by a variety of clinical symptoms. It is prevalent in approximately 1 in 10,000 live births, and is caused in large part by mutations in the *Chd7* gene, which account for 2/3 of diagnoses, though little is known about the genes and cellular processes this protein regulates. Additionally, there is little research funding devoted to understanding the contribution of *Chd7* towards the mechanism of this disease, or how this gene is involved in normal neuronal function. We have therefore created the first *Drosophila* model for CHARGE Syndrome by utilizing an RNA interference strategy whereby we knockdown the function of the fly homolog of *Chd7*, a gene named *kismet* (*kis*). These flies display prominent and genetically tractable phenotypes consistent with defects in central nervous system function, and allow for quick and quantitative genetic analysis of novel interactions between candidate genes that might contribute to these phenotypes, and thus to the pathogenesis of CHARGE Syndrome.

Our specific aim is to validate the effectiveness of utilizing our *Drosophila* CHARGE model towards further understanding the clinical symptoms and disease pathogenesis of CHARGE patients. Our preliminary data show that *kis* regulates the transcription of the proneural genes *atonal* and *daughterless* in flies. These genes are excellent candidates for misregulation in CHARGE Syndrome, as the human homologs of these genes are required for many aspects of brain and neuronal development, including specification of sensory neurons in both the human retina and cochlea, cerebellar development, and the regulation of dendritic arborization (branching) in the developing brain.

We will utilize the powerful behavior analyses capable of being performed in *Drosophila* to quantify any aberrant behavior in our CHARGE flies as compared to our control flies (those that do not knock down *kis* function). We will then quantify how these behaviors are affected when we introduce mutations in the proneural genes *atonal* and *daughterless* within the genetic background of these flies. We will then determine how mutation in *kis*, *atonal*, and *daughterless* affect the neuronal morphology and arborization patterns of a specific subset of Atonal positive neurons in the brain through immunohistochemistry and confocal microscopy. This will help us determine the contribution of these genes towards neuronal structure and function. Finally, to determine if this transcriptional regulation is conserved in human cells, we will analyze the mRNA expression of *atonal* and *daughterless* human homologs in human cells after *RNAi* knockdown of *Chd7* in these cells.

Principal Investigator

Daniel R. Marenda, PhD
Assistant Professor
Drexel University
3141 Chestnut Street
Stratton Hall, 230
Philadelphia, PA 19104

Participating Researchers

Aleister J. Saunders, PhD - Employed by Drexel University

Expected Research Outcomes and Benefits

Using a genetic knockdown technique, we have created a novel *Drosophila melanogaster* model for CHARGE syndrome. Using the phenotypes associated with this model, we expect to analyze which genes can functionally contribute to the pathogenesis of CHARGE Syndrome through genetic enhancement and suppression studies. We hope that this research will lead to novel diagnostic tools and/or therapeutic targets for patients with CHARGE Syndrome. By analyzing how the phenotypes associated with a fly model of the disease can be altered through genetic manipulation of other genes (genes considered to be good candidates for contribution to the disease), we are able to get a better understanding of how loss of these genes could contribute to disease symptoms within the context of CHARGE Syndrome. Do mutations in candidate genes make the phenotypes in the fly worse or better?

Summary of Research Completed

<u>Creation and further testing of a novel *Drosophila* model of CHARGE syndrome (CS)</u>
After identifying *kis* in a screen for proneural gene expression and because the human homolog of *kis* is involved in CS, during the first half of the reporting period, we developed a disease model utilizing a *Drosophila* loss-of-function *kis* effect that produced viable adults with highly recognizable and prominent neurological and/or developmental phenotypes, and then use this model to determine if the regulation of proneural gene expression was important within this model. During this reporting period, we have utilized our disease model to further understanding the underlying factors that may be contributing to the pathology of CHARGE Syndrome. These accomplishments include identifying defects in memory and also uncovering specific defects in the development of three different populations of neurons in the brain, as described below.

To begin to investigate the role of *kis* in fly behavior and neural development, we utilized the Gal4/UAS system to express *UAS:kis* RNA interference transgenes specifically within the CNS to generate adult flies with decreased *kis* expression in these tissues. We tested learning and memory in these flies using an associative conditioning procedure, the courtship suppression assay. This assay is ethologically based and capable of measuring both learning and memory in individual flies. The conditioning aspect of this assay is based on the observation that male courtship behavior is modified by exposure to a previously mated female unreceptive to courting.

Thus, after 1 hour of unsuccessful courting of a mated female, wild type males suppress their courtship behavior in the last 10 minutes of the training phase, indicative of proper learning (Figure 1A). Trained males also suppress their courtship behavior towards subsequently encountered receptive virgin females for 1-3 hours by 40% or more (the memory phase of this assay, Figure 1C). We found that when *kis* is knocked down roughly 90%, specifically in neurons associated with learning and memory, these flies were capable of learning in this assay (Figure 1B). A trained wild type fly continues to suppress his courtship towards a subsequently receptive virgin fly 2 minutes after training (Figure 1C). This represents a change in behavior indicative of memory of training. However, flies where *kis* had been knocked down had no memory of this learning 2 minutes after training (Figures 1D). Because these flies are capable of successful perception, and experience-dependant alteration of their behavior during the training (learning) component of this assay, their inability to suppress their courtship frequency in the second component (memory) of this assay indicates that these flies are defective in their immediate recall memory of this learning.

Because the *kis* gene encodes for a transcription factor, we hypothesize that the behavioral defects in memory we observe are due to the mis-regulation of gene(s) important for immediate recall memory formation during development. However, there are multiple cellular processes that could be affected by *kis* mutation, including the neurogenesis of critical neurons in this memory circuit, and/or control of circuit connectivity once these neurons have differentiated, and/or control of the development and/or morphology of these neurons. To begin to address these questions, we analyzed the effect of loss-of-function in *kis* on neuronal development and morphology of the Kenyon neurons, as these neurons are associated with learning and memory in multiple experimental paradigms in *Drosophila*. We utilized the MARCM technique to create clones of neurons that are homozygous mutant for kis^{LM27}, a protein null mutant. The population of Kenyon cells consist of three distinct groups of neurons, each with its own characteristic developmental morphology. During larval development, the γ subset of Kenyon neurons are differentiated first, and these neurons undergo highly stereotyped dendritic and axonal pruning during pupal development. Pruning of these neurons occurs by localized degeneration, and is evident by 18 hours after puparium formation in wild type neurons (Figure 2A, arrow shows remnants of γ axonal projects into the brain). While γ neurons mutant for *kis* undergo proper dendritic pruning, they display defects in their axonal pruning (arrow in Figure 2B), and continue to display un-pruned γ axons projecting into the brain 40% of the time (N=10, P<.05).

The final adult structure of the mushroom body axons consist of 5 distinct projections to the α, α', β, β', and γ lobes (Figure 2C). To determine if structures other than γ lobes are affected by mutations in *kis*, we created MARCM clones mutant for kis^{LM27} using the *OK107-Gal4* driver, which is expressed in these 3 populations. While Kenyon cell dendrite morphology was also normal in these *kis* mutant neurons (data not shown), we did observe axonal migration defects in these cells where axons cross the midline of the brain to migrate into the opposite brain lobe 55% of the time (arrow in Figure 2D, n=11, P<.05).

Expression analysis shows that the Kis protein is widely expressed in the developing fly brain (data shown in previous progress report). Given that mutations in *kis* affect axonal pruning and axonal migration in developing Kenyon neurons, we next analyzed the effect of *kis* loss-of-function in other neuron populations in the developing and adult brain to determine if the Kis

protein may play a broader role in regulating neuronal morphology. Based on Kis expression patterns in the brain, we created MARCM clones mutant for *kis* function in the Dorsal Cluster (DC) neurons, a subset of Atonal-expressing neurons in the larval and adult brain. These neurons form a highly stereotypical pattern of connections in the fly, extending a bundle of neurites posteriorly which then branch into a bundle of commissural axons that migrate contralaterally to innervate targets of the opposite brain lobe (Figure 3A). Developing larval DC neurons mutant for kis^{LM27} exhibit several morphological abnormalities indicative of abnormal axon development, including abnormal commissural axon projections (arrow in Figure 3B, 32% frequency, n=19, P<.05); abnormal positioning within the brain, appearing laterally (left arrow in Figure 3B, 52% frequency, n=19, P<.05); and groups of DC neuron soma that are not part of the larger soma cluster (arrowhead in Figure 3B, 32% frequency, n=19, P<.05).

In adults, DC neurons form highly complex dendritic and axonal fields (Figures 3C and E). Adult DC neurons project neurite bundles that branch ipsilaterally to form the dendritic field (Figure 3C), and also project a large bundle of commissural axons contralaterally to innervate the lobula and medulla in a stereotypical fan-like pattern (Figure 3E). Adult DC neurons homozygous mutant for *kis* do not display abnormal dendrite formation (Figure 3D). However, *kis* mutant DC neurons show a severe reduction in the number of axons extending into the lobulla area of the brain, and subsequently extending from the lobulla into the medulla region of the brain (arrow Figure 3F, 100% frequency, n=5, P<.05). Wild type MARCM clones exhibit 14.25±.95 neurites extending from the lobulla into the medulla, while *kis* mutant MARCM clones exhibit 6.0±3.47 neurites extending from the lobulla to the medulla, a significantly lower number (P=0.0055). These results are similar to those observed in Kenyon cells, the dendrites develop normally, while the axons do not.

As an initial test to determine if the gene expression changes observed in our *Drosophila* model were conserved in human cells, we utilized human HEK293 cells to assay for conserved transcriptional regulation of the human homolog of the fly *atonal* gene. We performed gene knockdown by RNA interference (RNAi) using siGENOME SMARTpool reagents (Thermo Fisher Scientific, Dharmacon RNAi) according to the manufacturer's protocol. We then performed RT-PCR from these cells, and assayed the levels of the human homolog's of *atonal* (*Math5* and *Math1*), and the human homolog of *kismet* (*Chd7*) in these cells after *Chd7* knockdown (Figure 4). As a control for knockdown, we used ON-TARGETplus non-coding RNA (NC). As a control for cDNA loading and amplification we used *Glyceraldehyde 3-phosphate dehydrogenase* (*gapdh*, a gene unaffected by our RNAi treatment, and also unaffected in our *kis* microarray analysis).

After RNAi knockdown of *Chd7*, we observed a decrease in both *Math5* and *Math1* mRNA levels, as compared to mRNA levels in our NC control RNAi treatment (Figure 4). Importantly, *Math5* and *Math1* mRNA levels were decreased, but not completely absent upon *Chd7* gene knockdown, consistent with *kis* mutant clones in *Drosophila* tissues as reported previously in the preliminary data of our submitted grant proposal.

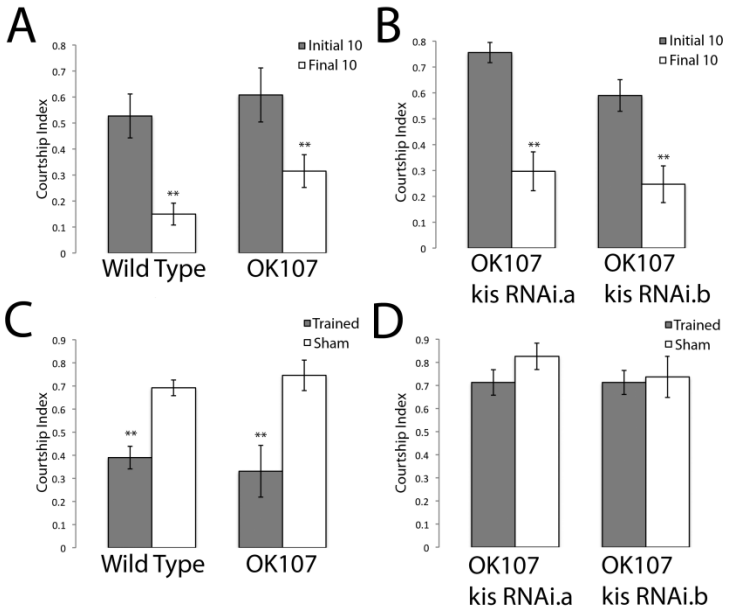

Figure 1. *kis* knockdown flies can learn, but are defective in memory. A-D shows the courtship index (CI) as the % of time male flies spend performing courtship behavior over the total amount of time assayed. (A) Shows CI of wild type and OK107-Gal4 outcrossed control flies during first and last 10 minutes of a 1 hour training session. OK107-Gal4 is expressed specifically in neurons associated with learning and memory in the fly. Note the significant decrease in CI in the final 10 minutes (white column) compared to the first 10 minutes (grey column) indicative of a proper *learning* response. (B) Shows CI of CS flies. Genotype is OK107-Gal4/kis-RNAi line (RNAi.a and RNAi.b). Note decrease in CI in final 10 minutes, indicative of proper learning. (C) Shows CI for 2 minute memory of trained control flies compared to genotype equivalent Sham controls. Note significant reduction of CI in trained flies compared to Sham controls, indicative of normal *memory* of training. (D) Shows CI for 2 minute memory CS flies. Note no significant decrease in CI of trained CS flies compared to genotype equivalent sham trained control CS flies. Not shown are UAS:kis RNAi (RNAi.a and RNAi.b) outcrossed results, which are the same as wild type and Gal4 outcrossed control flies.

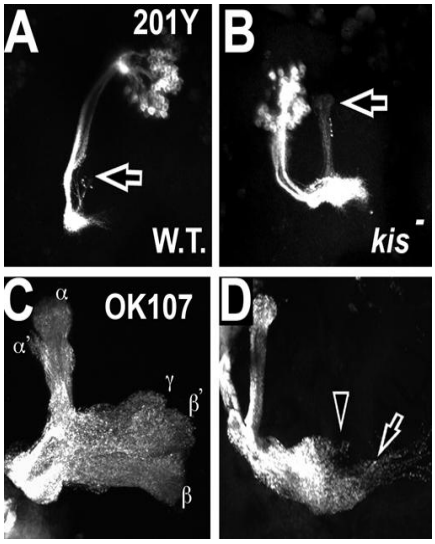

Figure 2. Kismet is required for proper axon pruning and axon migration in developing mushroom bodies. All panels show GFP in Kenyon neurons by MARCM analysis. (A-B) Pupal brains 18-20 hours after puparium formation (apf). (C-D) Adult brains 48 hours after eclosion. (A) Wild type MARCM clones (FRT 40A) in pupal brains driven by *201Y-Gal4* show remnants of proper axonal pruning of γ neurons that were previously populating the α lobes (arrow). (B) kis^{LM27} homozygous mutant MARCM clones display unpruned γ axons that continue to populate the α lobes (arrow). (C) Wild type MARCM clones (FRT 40A) in adult brains driven by *OK107-Gal4* show normal pattern of α, α', β, β' and γ axons innervating the mushroom body lobes, as labeled. (D) kis^{LM27} homozygous mutant MARCM clones in these adult brains often display abnormal axon migration beyond the midline (demarcated by the arrowhead).

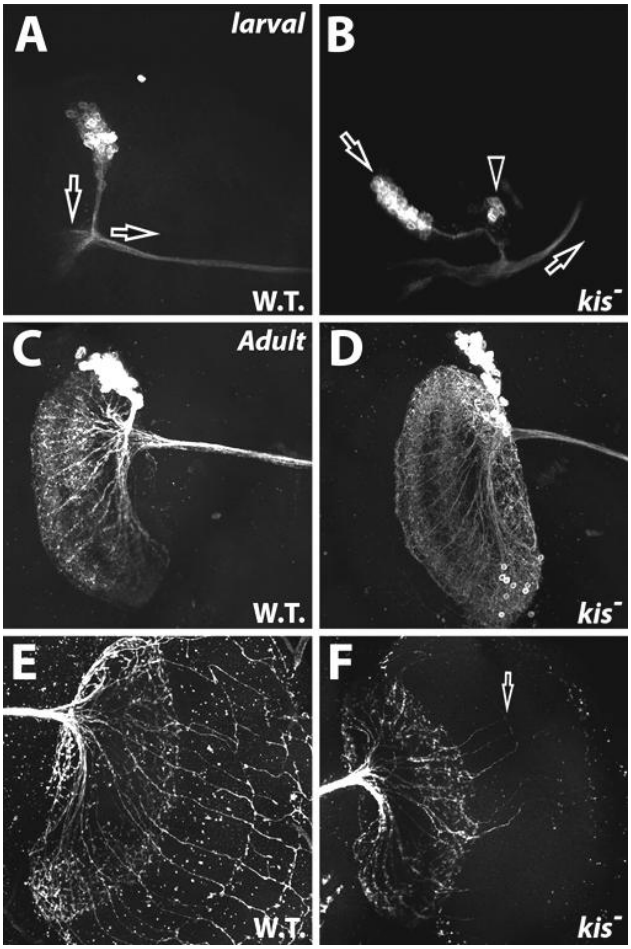

Figure 3. Kismet is required for proper cell and axon migration in developing Dorsal Cluster neurons. All panels show GFP in DC neurons by MARCM analysis. (A-B) Late third instar larval brains. (C-F) Adult brains 48 hours after eclosion. (A) Wild type MARCM clones (FRT 40A) in larval DC neurons. Note position of the soma cluster axon bundles (parallel to vertical arrow) compared to commissural axon bundles (below horizontal arrow). (B) kis^{LM27} homozygous mutant MARCM clones display abnormal positioning of soma cluster compared to commissural axon bundles (left arrow), soma that have developed outside of the normal cluster (arrowhead), and disrupted commissural axon migration (right arrow). (C) Wild type MARCM clones (FRT 40A) in adult DC neurons displaying normal dendritic morphology on ipsilateral brain hemisphere. (D) kis^{LM27} homozygous mutant MARCM clones in adult brains. Overall morphology of dendritic field appears normal. (E) Wild type MARCM clones (FRT 40A) in adult DC neurons displaying normal axonal morphology on contralateral brain hemisphere. (F) kis^{LM27} homozygous mutant MARCM clones in adult brains. Arrow displays abnormal and reduced number of axonal extensions from lobulla into the medulla.

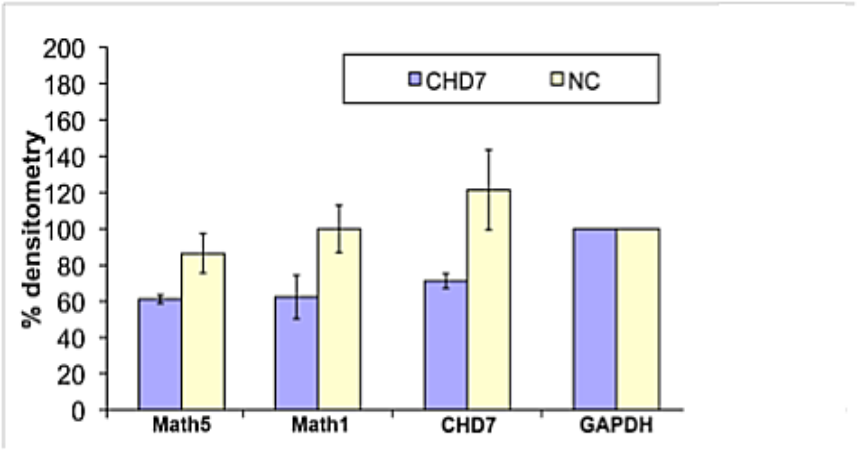

Figure 4. *Chd7* regulates *Math5/Math1* expression in human cells. Chart shows quantification of RT PCR levels in *Chd7* knockdown HEK293 cells (CHD7) compared to control non-coding (NC) transfected cells. Note the decrease on *CHD7* mRNA levels, indicating successful knockdown. Note the decrease in both *Math5* and *Math1* levels in knockdown cells compared to controls.

Research Project 11: Project Title and Purpose

Multidimensional Shape/Color Distributions as a Computational Biomarker for Cancer Pathology - The purpose of the project is to develop computational techniques for analyzing histology images of breast cancer tumors. The computational techniques will derive shape and color information from the images that will enable automated evaluation of the tumor. Specifically, the techniques will be used to determine if a patient's breast cancer has spread to nearby lymph nodes by examining a primary tumor that has been removed from the patient. This image analysis capability will eliminate the need for exploratory surgical removal of lymph nodes; thus eliminating the associated side effects, e.g. pain, swelling and morbidity, and costs.

Duration of Project

1/1/2009 - 6/30/2010

Project Overview

We will develop novel computational technologies that may be used to automatically and objectively predict the axillary lymph node status of breast cancer tumors via multiresolution image analysis of the primary tumor. Our hypothesis is that the structure of the nuclear pleomorphisms found in breast cancer tumors can be transformed into high-dimensional shape distributions using geometric measures from stochastic geometry. We will augment this space with information derived from the color/texture variations of the hyperchromatism found in the cancer cell nuclei and the expression of multiple prognostic markers. We hypothesize that, once the structure and color of the cells has been transformed, the resulting distributions of N pathologic staging categories will map into well-defined regions of the high-dimensional

distribution space. Mapping an unknown breast cancer sample into this high-D space and determining, via machine learning, to which region it belongs will allow us to automatically predict its axillary lymph node status.

Specific Aim 1 – Extend and improve recently developed histology image segmentation and shape distribution generation technologies/algorithms.

Specific Aim 2 – Develop techniques that create color distributions from the pixel regions of the histologic and prognostic marker images that correspond to the segmentation pixels identifying neoplastic cell nuclei.

Specific Aim 3 – Investigate machine-learning technologies for determining which geometric measures and spectral features will best discriminate between lymph node status categories and provide the most reliable/significant lymph node metastasis status classifier.

Specific Aim 4 – Using breast cancer databank specimens, numerous cases will be digitized, processed, and analyzed to validate the approach.

The project will employ a routinely used prognostic immunohistochemistry panel together with H&E staining. The panel includes: estrogen and progesterone receptors, MIB-1 (to calculate proliferative activity), mutated p53 and HER2/neu. Shape distributions represent the structure/shape of 2D/3D objects with a probability distribution produced by repeatedly and randomly applying geometric measures. Stochastic geometry analyzes and quantifies the connections between geometry and probability in order to describe and characterize aggregate statistical geometric properties. Based on information theoretic distance metrics between the shape distributions, classifiers will be trained to automatically identify lymph node statuses. We will mainly investigate the use of multi-class kernel support vector machines for non-linear classification of all lymph node categories.

Principal Investigator

David E. Breen, PhD
Assistant Professor
Drexel University
Computer Science Department
3141 Chestnut Street
Philadelphia, PA 19104

Other Participating Researchers

Fernando U. Garcia, MD, Aladin Milutinovic, MS - Employed by Drexel University

Expected Research Outcomes and Benefits

Despite a variety of new tumor markers resulting from significant progress in the molecular and genetic characterization of breast malignancies, axillary lymph node metastasis status continues

to be the most critical prognostic variable in the breast cancer management decision-making process and patient survival. Regional lymph nodes status, primary tumor size, and distant metastasis are the three variables defining pathologic staging performed routinely for clinical cancer. The increasing use of systemic adjuvant therapy and local radiotherapy even in lymph node-negative breast cancer patients together with the decrease in tumor size due to early detection raises questions about the need for routine lymph node dissection on all breast cancer patients. If lymph node status could be accurately and consistently predicted prior to axillary dissection, a considerable number of patients with low probability of lymph node metastases might avoid axillary dissection and its associated critical side effects (e.g. lymphedema, numbness, pain, infection and compromised immunity) and morbidity. Eliminating the need for lymph node dissection will also lower the associated costs.

Summary of Research Completed

The project has 4 specific aims/tasks: 1) image processing/segmentation/shape distribution generation, 2) color distribution generation, 3) machine learning for classification, and 4) sample scanning and method validation. Significant results were produced during this reporting period. These results demonstrate that our imaging, image processing/analysis and machine learning technologies may be used to identify breast carcinomas that have metastasized to nearby lymph nodes, via inspection of the primary tumor removed from the breast.

The computational pipeline for automated lymph node metastasis status prediction based on analysis of primary breast tumor histology is presented in Figure 1. The stages of the pipeline include: 1) selection and scanning of H&E slides, as well as gathering the associated de-identified patient data, 2) accurate and robust automated cancer cell and tumor structure segmentation techniques, 3) computing geometric measures from stochastic geometry that transform cancer cell/tumor shapes into shape distributions, 4) creating intensity distributions from the texture variation / nuclear hyperchromasia levels within cancer cells, 5) mapping the high-D shape/color distributions into a lower dimensional feature vector for separation analysis, 6) supervised machine learning technologies that classify test samples into lymph node metastasis status with probabilistic confidence values based on the feature vectors. All of the algorithmic steps needed to produce our computational pipeline were completed in the second phase of the project. Steps 1, 2 and 3 were completed in the first 6 months of the project. Implementation of step 4 had also begun at this point. Steps 4, 5 and 6 were completed in the final phase of the project. Technical details describing these steps, as well as the project's results, are given below.

<u>Intensity Distribution Generation.</u> Software was developed to generate intensity distributions from each histology scan. This process begins by separating the scans into three color channels, Hue, Saturation and Value (HSV). An intensity distribution is computed for each channel, producing three distributions per sample. The algorithm for producing the intensity distributions is the following. Given the segmented image of the scan and the three intensity images for Hue, Saturation and Value, iterate through all pixels of the segmented image. White pixels in the segmented image signify stained cancer cell nuclei in the original scans. For each white pixel in the segmented image find the intensity value at the associated pixel in the HSV images. A histogram of intensity values is created for each channel (HSV). The distribution of intensity

values within each channel is produced by simply accumulating the values in appropriate bins in the HSV histograms, when processing all white pixels in the segmented image.

Sample Distribution Generation. Using the image processing and segmentation software developed in the early stage of the project, two binary segmented images are generated for each of the 100 histology scans used in our study. One binary image is produced by processing the high resolution scans. The second is produced by applying a morphological closing to the high resolution binary image, and captures the large-scale structure of the invasive cancer cell formations. Our sample set consists of 55 N0 cases (negative for lymph node metastasis) and 45 N1+ cases (positive for lymph node metastasis). These samples were identified and scanned in the early phase of the project. All of the image processing/segmentation and shape distribution techniques described in the previous report, as well as the intensity distribution technique, were applied to these sample images. Applying our distribution generation algorithms to these samples produced 11 raw distributions for each case. Six shape distributions (area, perimeter, area/perimeter, aspect ratio, inside radial contact and inside line contact) and three intensity distributions (HSV) are produced from the high resolution images. Two additional shape distributions (inside radial contact and inside line contact) are produced from the closed, large-scale-structure binary images. The range of values present in the inside radial contact and inside line contact distributions were observed to be quite large, varying by many orders of magnitude. Concerned that these great differences in values may adversely affect downstream processing, four additional distributions were produced by transforming the individual bin values by the natural log; Thus significantly decreasing the range of values within the inside radial contact and inside line contact distributions.

Dimension Reduction. The distributions, which are represented by histograms, usually have a large and varied number of bins. The number of bins in any one histogram may reach into the 10's of thousands. For statistical analysis each bin may be considered a dimension of a feature space. Having such an enormous feature space makes analysis extremely difficult. Therefore it is necessary to reduce the dimensionality of the features produced by the shape/color distribution calculations. This is accomplished by calculating characteristic statistics for each distribution, i.e. the distributions are transformed from histograms into a low-dimensional feature vector. For each distribution, the following 10 quantities were computed: {mean, median, mode, standard deviation, skew and kurtosis} of the values used to make the histograms; and the maximum bin number, maximum value over all bins, mean and standard deviation of the bin values. Additionally, measures that produce distribution histograms of a fixed width (e.g. aspect ratio, hue, saturation and value) can also be averaged down to make a coarser distribution with 10 bins. The dimensionality reduction step takes histograms that cannot be effectively processed and transforms them into a low dimensional (10) feature vector that is now tractable and analyzable. Once completed this stage produces 17 (13 distributions statistics + 4 averaged down distributions) 10-element feature vectors for each sample. In summary, the 17 feature vectors are: 1. Area, 2. Perimeter, 3. Area divided by Perimeter, 4. Aspect Ratio, 5. Inside Radial Contact, 6. Inside Line Contact, 7. Log of Inside Radial Contact, 8. Log of Inside Line Contact, 9. Log of the Large Scale Structure Inside Radial Contact, 10. Log of the Large Scale Structure Inside Line Contact, 11. Hue, 12. Saturation, 13. Value, 14. Averaged Hue, 15. Averaged Saturation, 16. Averaged Value, and 17. Averaged Aspect Ratio.

Classification via Supervised Machine Learning Techniques. This stage treats the classification process as a data fusion problem, with each one of the 17 feature sets representing a different source of data. Each such source provides some prognostic information, and can be used to train an automated classifier to predict the metastasis status. Based on our preliminary analysis, we concluded that there is complementary information carried by different feature sets, and a strategic combination of such information can significantly improve the prognostic accuracy, compared to any of the feature sets used alone. We used an ensemble of classifiers based approach to data fusion. In this framework different supervised classifiers are trained on data obtained from different sources. In this case, we have 17 such classifiers, specifically 17 Support Vector Machine (SVM) classifiers. Each classifier makes a prediction (yes or no), whether the patient's tumor has metastasized and has a positive lymph node status (N1plus).

This process was further improved, however, by using a "stacked generalization" type of combiner. In stacked generalization, the classifier combiner is an additional "meta-classifier" whose inputs are the outputs of the individual classifiers. In such a framework, the meta-classifier effectively determines how the classifiers should be combined, by analyzing which classifiers are better predictors in which parts of the feature space, or in other words, which data sources / feature sets provide more relevant prognostic information for any given set of values for those features. The meta-classifier can be trained such that their outputs can be interpreted as a lymph node metastasis status probability for each sample. We used Logistic Regression as the "meta-classifier" so that the predictions are not just binary decisions, but also carry a probabilistic measure of the lymph node metastasis status. Logistic Regression fits the data to a logistic sigmoid function with simple probabilistic interpretation of the output, and naturally allows for the creation of an ROC curve, providing effective evaluation of the sensitivity / specificity tradeoff.

In the first stage of the classification process 17 SVMs, one for each feature vector, were used to predict the lymph node metastasis status. This produces a binary classification result, where lymph node positive metastasis status is represented by a "1" and negative status is represented by a "0". The Leave-One-Out (LOO) approach was used to predict the lymph node metastasis status of each sample. 99 samples are used to train the SVM and the remaining sample is then treated as a test sample and classified. This is repeated for each of the 100 samples. Thus for each SVM classifier we compute a 100x1 vector of binary predictions. Once the computation was completed for each of the 17 SVMs, a 100x17 binary matrix is produced, where each row represents the outcomes of the 17 SVMs for each sample. Both the value of the penalty factor, C, and the selection of kernels were varied to optimize the harmonic mean of the sensitivity and specificity of the classification results for each SVM. This customized each SVM and ensured that the most effective parameters were used for each feature vector.

The 100x17 binary matrix was used as input to the "stack-generalization" stage. The Binary Logistic Regression (BLR) classifier found in the SPSS software was used as the "meta-classifier". The outcome of the BLR analysis is the probabilistic confidence measure that a sample has "N1+" status, i.e. that the tumor has metastasized to a lymph node. An outcome of a sample with 0.90 means the classifier predicts the sample as a N1+ with high confidence. Whereas an outcome with a result of 0.10 means the classifier predicts the sample as a N1+ with low probability, or conversely classifies the sample as N0 with high probability.

Results. The SPSS BLR classifier produced a probabilistic prediction for each sample that it is in the N1+ class. The default threshold value used to classify a sample as "N0" or "N1+" is 0.5. This threshold value produced classifications with a sensitivity of 77.8% and specificity of 85.5% over all 100 samples. Since BLR does not produce a true probability, the threshold may be varied. This generates the Receiver Operating Characteristic (ROC) curve for the overall classification process and allows us to find the optimal threshold value, i.e. the one that produces the best classification results. The optimal threshold value of 0.357 produced a classification sensitivity of 91.0% and specificity of 80.0%, and correctly classified 85 of the 100 samples. The ROC curve is the plot of sensitivity versus (1-specificity) over the full range of threshold values. The ROC curve for the BLR meta-classifier is presented in Figure 2. The area under the curve may be used to characterize the accuracy of the classifier and its ability to separate the two classes. The area under the curve in Figure 2 is 0.90, which qualifies the approach as a good to excellent classifier.

Summary. Our project achieved its objective by demonstrating that lymph node metastasis status can be determined via inspection of primary breast carcinoma histology. The inspection process involves image processing and shape analysis of the stained invasive cancer cells in scans of the histology specimens. Our study is certainly not conclusive. Additional, and possibly more effective, geometric measures need to be evaluated. Further studies with many more test samples must also be conducted. This will be the focus of future work (and funding efforts) that will build on this encouraging preliminary research.

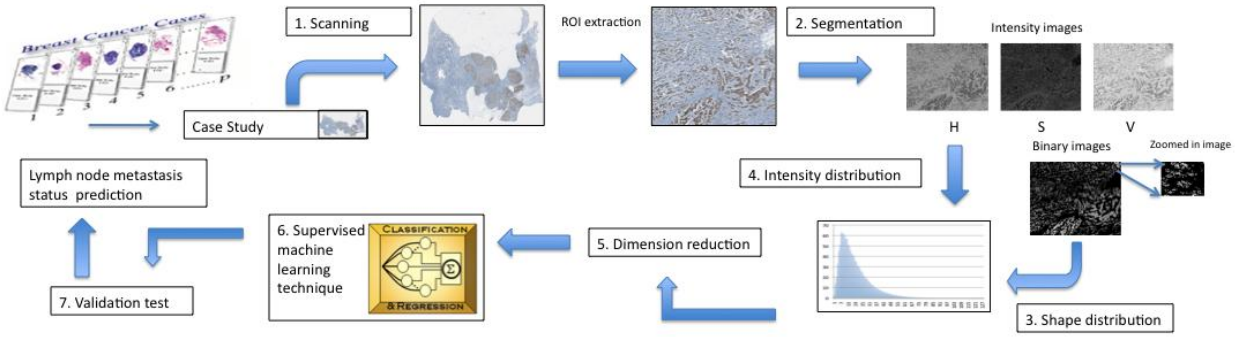

Figure 1. Computational pipeline for automated lymph node metastasis status prediction based on analysis of primary breast tumor histology.

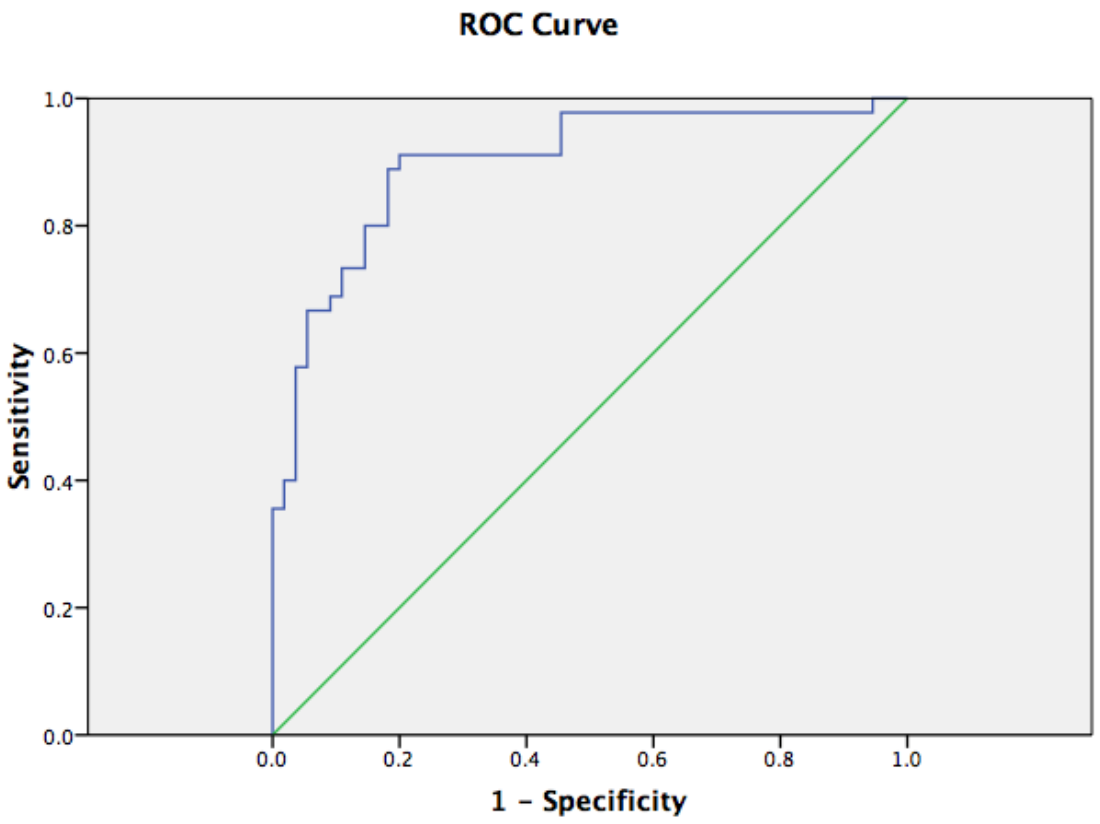

Figure 2. ROC curve for Binary Logistic Regression stacked meta-classifier.